Diffusion of Cosmic Rays in Galaxies and Clusters of Galaxies and its Application to SKA and CTA

Asha Tailor

A Thesis submitted to the
School of Physics,
Faculty of Science,
University of the Witwatersrand,
in fulfilment of the requirements for the degree of
Doctor of Philosophy.

Johannesburg, June 2015.

DECLARATION : I declare that this Theses is my own, unaided work. It is being submitted for the degree of Doctor of Philosophy at the University of the Witwatersrand, Johannesburg. It has not been submitted before for any degree or examination to any other University.

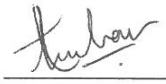

(Signature)

8 June 2015

(Date)

This one is for you Papa
Mahendrakumar Tailor
24 June 1955 - 9 December 2013

Contents

ACKNOWLEDGEMENTS

The research in this thesis was supported by the DST/NRF SKA post-graduate bursary initiative. This research would not have been possible without the continuous guidance from my supervisors Prof. Sergio Colafrancesco and Dr. Paolo Marchegiani. Their guidance and encouragement throughout this journey is really appreciated. The lengthy discussions and valuable inputs from them both have really helped me grow as a researcher.

I would also like to acknowledge the encouragements received during these years from my colleagues Nebiha, Nicola, Shehzad, Remu, Claudio, and Peter. I would like to thank them all for making a work place a fun place to be. I would further like to thank Nebiha for being a wonderful friend during the most difficult times of my PhD.

I would also like to thank my love, Dario Fanucchi for believing in me, for his continuous encouragement and undivided attention to all my complaints as well as for being there when I needed him the most. I would also like to thank him for the discussions on numerical methods which were very useful for obtaining accurate results as well as for proof reading my thesis and providing interesting comments.

I would further like to extend my appreciation to the School of Physics and its members for providing a good environment to work in.

There aren't enough words to express my gratitude to my family. During the period of my thesis my family lost five family members, including my grandfather Mohanlal Tailor, my uncles Raman Tailor and Amrutlal Merai, my aunt Taraben Tailor and my dearest father Mahendra Tailor. They were all great inspirations to me. Without the support of my parents and their love and their tremendous amount of belief, this work would not have been possible. My mom has been a pillar of strength throughout these difficult times and her continuous support and confidence in me has helped me achieve my goals. I would also like to thank my beautiful sisters Rupaben and Sonuben for being very understanding and taking over some of my responsibilities during this period. Finally, this acknowledgement would be incomplete without mentioning my little munchkins, my nieces, Arpita and Tia, and my nephew Chirag for being so entertaining and for always brining a smile on my face.

ABSTRACT

Galaxy clusters are the largest virialised and most recently formed cosmic structures. Their study is therefore a powerful mechanism to probe the large scale properties of the universe. A full understanding of the non-thermal properties of galaxy clusters has not yet been achieved. In particular, the origin of radio halos in galaxy clusters is still a topic of debate today. Several models have been proposed to explain the origin of radio halos but all of these models present some problems either in reproducing observations or in predicting the values of their parameters.

Recent observations of radio halos in clusters have shown that in some clusters the morphology of the radio emission appears to be more correlated with the distribution of galaxies than it is with the thermal gas. It has also been observed that while most clusters exhibit a correlation between the radio and X-ray luminosities, there are clear exceptions to this rule. Motivated by these observations, we propose a new theory to explain the origin of radio halos in clusters: that the radio emission observed in clusters is produced by electrons injected by different galaxies and diffusing in the intra cluster medium.

In developing our theory, we study the diffusion of relativistic electrons in galaxies by obtaining a very general solution of the diffusion equation which describes the transport of cosmic rays. This solution allows us to study the spatial, spectral and temporal properties of relativistic electrons and their radio emission for a wide range of cosmic objects. We test this model by applying it to the radio galaxy M51 and reproduce its spatial and spectral properties. We also study the evolution of M51-like galaxies. The model is then applied to study radio halos in clusters of galaxies. We investigate how the properties of these radio halos change when the number and types of sources in a cluster are varied. We compare the results of this model with the observed radio map and density flux spectrum for several galaxy clusters, specifically the low-luminosity cluster CL1446+26 and other clusters with a range of luminosities.

Our model provides a very promising explanation of the properties of radio halos in galaxies and clusters of galaxies. The observed properties like the morphology of radio maps in galaxy clusters, the flux spectrum and the correlation between radio and X-ray luminosities, can be reproduced by our model. This is done by considering the combination and evolution of galactic sources having radio properties similar to those of M51. Our model is simple and nevertheless very promising and therefore refining it can lead to a better understanding of the origin of radio halos.

List of Figures

List of Tables

Chapter 1

Galaxy Clusters in Modern Cosmology

"The interval between the decay of the old and the formation and establishment of the new constitutes a period of transition which must always necessarily be one of uncertainty, confusion, error, and wild and fierce fanaticism."

-John C. Calhoun

1.1 Introduction

It is extremely impressive how much we have learned about our universe as a result of the hot big-bang model. This is especially evident when juxtaposed with the state of our knowledge just over a century ago when we thought that the universe was only a few million years old and the Milky Way was its only galaxy. As we now know, the universe is actually some ~ 13.7 billion years old, and comprises some fascinating structures we could not previously have imagined, such as galaxies, clusters of galaxies, superclusters, voids and great walls. Amazingly, these structures can be explained by the standard model of Cosmology: the hot big-bang (e.g., Kolb and Turner (1990); Peebles (1993)). This theory is based on Einstein's theory of General Relativity (e.g., Weinberg (1972)) and supplies us with quantitative tools for understanding the evolution of the universe. Using the theory we can, with great success, trace the structure visible in the universe today back to the gas of elementary particles that existed in the first fraction of a second after the big bang. All of this structure is believed to have arisen as a result of the attractive forces of gravity acting in tiny primeval inhomogeneities in the distribution of matter.

Concurrent with the theoretical advances of the last century, there have also been vast improvements in the way we observe the universe.

Perhaps the most significant advance is that we have extended the spectral band of our observations beyond optical frequencies. Up until a century ago, observations were obtained in the optical band only, limiting the data collected from the universe to light in the visible spectrum. Only later, when we started to develop ground- and space-based telescopes with a wider range of frequencies, did we begin to understand how much of the structure in the universe was previously invisible to us. Modern telescopes allow us to study the universe in the full electromagnetic spectrum, from radio ($\sim$ 50MHz) to gamma rays (with energy 10^{12} eV and more). Studies with these instruments have resulted in discovery of phenomena that could not have been observed with optical telescopes alone. Moreover, modern observational astronomy is not exclusively concerned with the detection of photons (light), but also with cosmic rays, neutrinos and gravitational waves. New techniques and instruments have been developed to study these phenomena, enabling us to observe still more structure in our universe.

Technological advances have also resulted in noteworthy improvements in our observations. Observational cosmology in its early days was based on images stored on photographic plates taken with small aperture telescopes. Today, the photographic plates have been replaced by Charge-Coupled Devices, which are able to collect photons with improved efficiency. This efficiency has been further improved by increases in the aperture of telescopes. These improved detectors enable us to view faint and distant objects that could not previously have been seen. Digital data and powerful modern computers also play a major role in modern observational methods, enabling us to interpret the vast amounts of data produced by our instruments by fitting models to observed data and performing complex computations in the study of new classes of phenomena far more efficiently than could previously have been achieved. We are now able to obtain results with better speed and better precision, which is especially important when modelling fine structures.

These improvements in technology allow us to study several new objects in both the local universe and the large scale universe. We are now able to understand properties of objects like stars, galaxies, AGNs, galaxy clusters, black holes, gamma-ray bursts, neutron stars and extra-solar planets. Moreover, we can study the distribution of neutral gas and ionised gas in the Universe.

One of the fields in which these improvements have had a great impact is cosmology - the study of large scale structures in the Universe. The largest known gravitationally bound structures in the universe, galaxy clusters, are important objects of study for cosmologists. Cosmological models make different predictions about the distribution of these clusters, and how this distribution evolves with time. Measurements of this distribution are therefore important tests of cosmological models. From the astrophysical point of view it is also important

to understand the detailed structure (both thermal and non-thermal) of galaxy clusters.

In the following we will describe the standard cosmological model of the Universe leading to structure formation. Our main focus will be on galaxy clusters, specially on the non-thermal properties and the origin of radio halos.

1.2 The present Cosmological Model

1.2.1 Basic Equations

Our present understanding of the origin and evolution of the Universe is based on the theory of the hot Big Bang (Gamow, 1946; Weinberg, 1972; Kolb and Turner, 1990; Peebles, 1993). This theory is based on the Friedmann-Lemaitre-Robertson-Walker (FLRW) metric, which is the exact solution of Einstein's field equations for a homogenous and isotropic universe (using $c = 1$):

$$ds^2 = -dt^2 + R(t)^2 \left[\frac{dr^2}{1 - kr^2} + r^2(d\theta^2 + sin^2\theta d\phi^2) \right]. \tag{1.1}$$

The quantity $R(t)$ is a scale-factor describing the expansion rate of the Universe. The constant k represents the spatial curvature, where negative k corresponds to an open universe, positive k to a closed universe and $k = 0$ to a flat universe. The change in the scale factor is governed by the Friedmann equation for the expansion rate:

$$H^2 \equiv (\dot{R}/R)^2 = \frac{8\pi G\rho}{3} - \frac{k}{R^2}, \tag{1.2}$$

where ρ is the total energy density from all components of mass and energy. The energy density $\rho(t)$ and the pressure $p(t)$ are related by the fluid equation:

$$\dot{\rho} + 3(\rho + p)\frac{\dot{R}}{R} = 0. \tag{1.3}$$

In this equation, $H = \frac{\dot{R}}{R}$ is the Hubble constant, the term $3H\rho$ is reduction in density due to the increase in volume, and the term $3Hp$ is the reduction in energy caused by the thermodynamic work done by pressure when this expansion occurs (Liddle, 1997). These equations can be combined to get:

$$3\frac{\ddot{R}}{R} = \Lambda - 4\pi G(\rho + 3p) \ , \tag{1.4}$$

giving the acceleration rate, where Λ is the cosmological constant originally introduced to allow for a static universe.

For a flat universe, corresponding to $k = 0$ in Eq.(1.1), the density of the universe is equal to the critical density:

$$\rho_c(t) = \frac{3}{8G\pi}H^2 = 1.88\, h_{100}^2 \times 10^{-29}\text{g cm}^{-3}. \tag{1.5}$$

where h_{100} is the Hubble constant at present time H_0 in units of 100 km s^{-1} Mpc^{-1}. The densities can be expressed as a fraction of critical density:

$$\Omega(t) \equiv \frac{\rho}{\rho_c}. \tag{1.6}$$

1.2.2 Observational Confirmation

An important consequence of the general relativity equations presented in the previous scetion is that the Universe must be either expanding or contracting. The hot big bang model is founded on these equations and it predicts that the behaviour of the evolution of the Universe is an expansion derived from a singularity when the density and the temperature were infinite. There are several observations that confirm this theory, the most important being the expansion of the universe, the presence of the cosmic microwave background (CMB) and the abundance of light elements.

Hubble's discovery of the expanding universe was the first empirical observation to support the cosmological model. In the late 1920s he obtained spectra for several galaxies and noticed that the spectra of galaxies at greater distances were systematically shifted to longer wavelengths. He expressed this observation as the redshift (Peebles, 1993):

$$1 + z \equiv \lambda_{observed}/\lambda_{emitted}\,. \tag{1.7}$$

He also plotted the radial velocity derived from the redshift of each object (interpreted as the Doppler velocity, where $V = zc$) as a function of the distance (see, Fig.1.1) and found that there is a direct relation between the distance D to the source and the radial velocity V. This relation is now known as the Hubble law:

$$V = H_0 D\,. \tag{1.8}$$

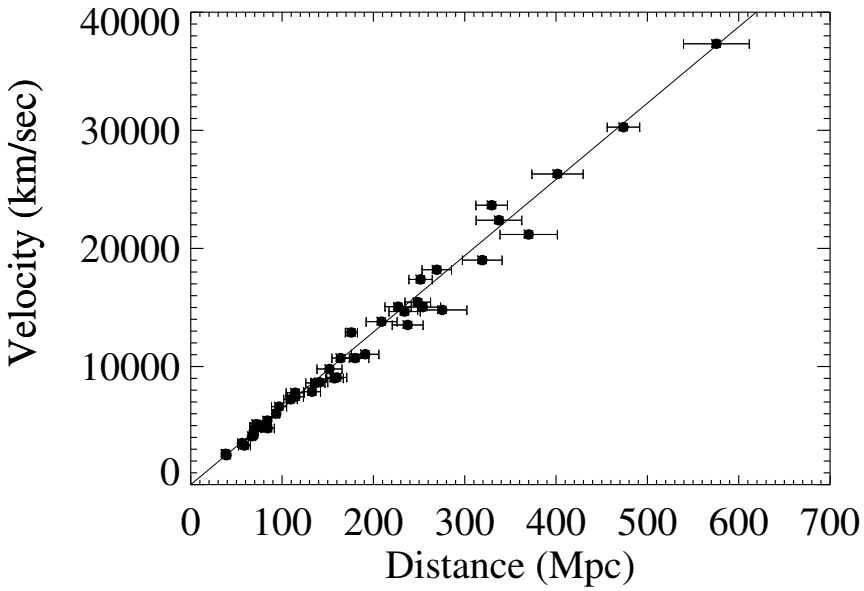

Figure 1.1: Hubble plot, representing the correlation between the redshifts and distance for his sample of galaxies. There is a clear trend suggesting that the redshift is directly proportional to distance (Turner and Tyson, 1999).

This observation that galaxies are moving away from each other suggests that the Universe is expanding, and confirms one of the predictions of Einstein's general relativity.

The second important test for the model was the discovery of CMB (Penzias and Wilson, 1965). CMB appears as isotropic radiation, with black body spectrum and temperatures similar to 2.7K. This is interpreted as the residuals of black body radiation from hot and dense conditions that are predicted to exist at early times in the hot big bang model. Today, CMB spectrum has been measured with extraordinary precision by the Far Infrared Absolute Spectrophotometer (FIRAS) on the Cosmic Background Explorer (COBE) satellite (Mather et al., 1990). It was observed that the CMB spectrum is Planckian, that is, any deviations are smaller than 300 parts per million (Fixsen et al., 1996) and the temperature was measured to be 2.7277 ± 0.002K (see Fig. 1.2). In the hot big bang model, this radiation has been emitted in the epoch of last scattering ($z \sim 1000$), when the temperature of the universe drops below 3000 K, the universe becomes neutral and the photons and electrons stop interacting due to Compton Scattering.

Spatially, the CMB is almost perfectly isotropic, with anisotropy of order $\frac{\delta T}{T} \sim 10^{-5}$. COBE was the first instrument to measure anisotropy in the CMB (Mather et al., 1990) and later better studies were carried out by WMAP (Hinshaw et al., 2013) and Planck (Planck

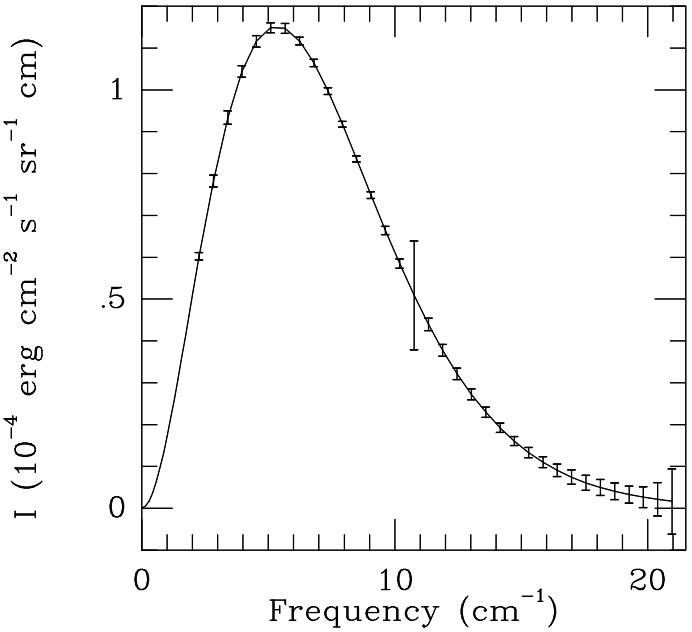

Figure 1.2: Spectrum of the Cosmic Microwave Background Radiation as measured by the FIRAS instrument on COBE and a black body curve for $T = 2.7277\,\mathrm{K}$. Note, the error flags have been enlarged by a factor of 400. Any distortions from the Planck curve are less than 0.005% (see Fixsen et al., 1996). [Image From (Turner and Tyson, 1999)]

Collaboration et al., 2015b) (see Fig. 1.3). These anisotropies are interpreted as seeds of structure formation in the Universe. By studying the power spectrum of anisotropy we are able to obtain information about cosmological parameters. The most recent results point to a Flat universe with $H_0 = 67.8 \pm 0.9\mathrm{km\ s^{-1}\ Mpc^{-1}}$ (Planck Collaboration et al., 2015c).

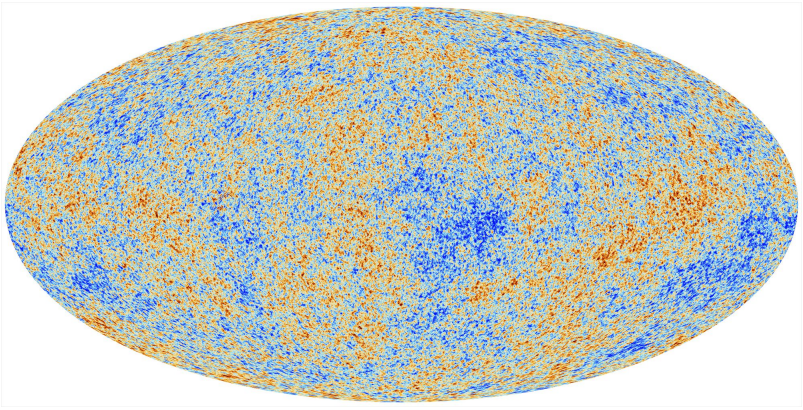

Figure 1.3: CMB anisotropies as observed by Planck.
Image Credit: ESA, Planck Collaboration

One of the earliest and most powerful tests of cosmology is the big bang nucleosynthesis (BBN). At the expansion age of one second the universe was a hot and dense mixture of

electrons, protons, neutrons, neutrinos and photons. At this stage of the Universe the number of protons was the same as the number of neutrons, due to interactions with neutrinos (Bothun, 1998). A few seconds after the beginning of the Universe, it cooled to the point (a temperature of around 1MeV) where some of the nucleons fused to form light elements D, ^{3}He, and ^{7}Li as a result of a sequence of nuclear reactions. The abundance pattern of light elements predicted by BBN (see Fig. 1.4) is consistent with that seen in most primitive samples of cosmos (Sarkar, 1996).

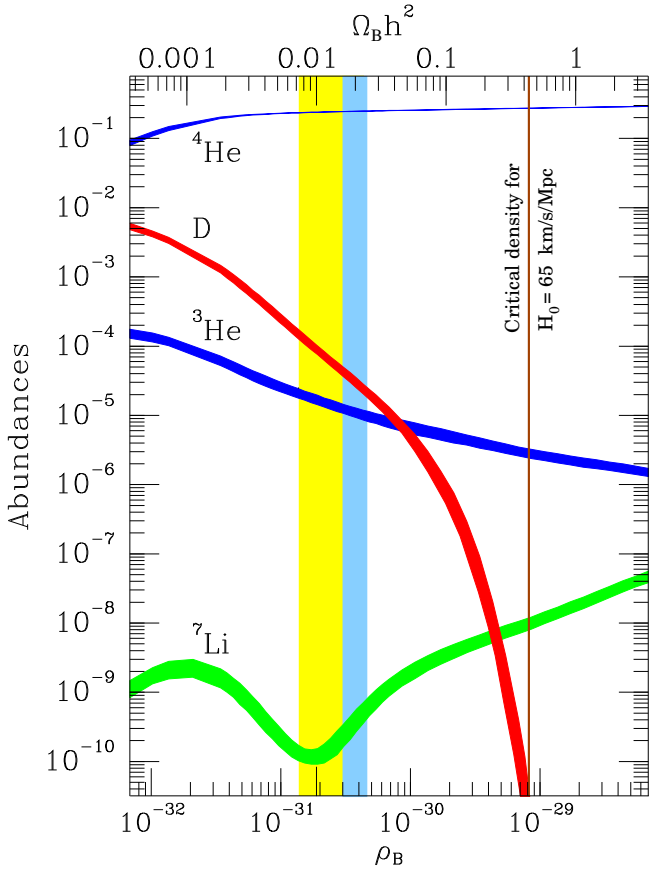

Figure 1.4: Predicted abundances of ^{4}He (mass fraction), D, ^{3}He, and ^{7}Li (relative to hydrogen) as a function of the baryon density. The broader band denotes the concordance interval based upon all four light elements. The narrower, darker band highlights the determination of the baryon density based upon a measurement of the primordial abundance of the most sensitive of these – deuterium (Burles and Tytler, 1998a; Burles and Tytler, 1998b), which implies $\Omega_B h^2 = 0.02 \pm 0.002$ [Image From (Turner and Tyson, 1999)].

1.2.3 Fundamental Additions to the Model

In the previous section we presented fundamental empirical confirmations of the big bang model. However, this model does present some problems. Here we briefly discuss these problems and introduce the additions to the model that lead to resolving them.

Inflation

One of the problems that the model posed was the flatness of the Universe. The FLRW solution with $\Omega = 1$ (Eq.1.6) is highly unstable, and as a consequence a small deviation from this number would lead to the Universe re-collapsing or rapidly expanding. However, observations reveal that the Universe is very close to being flat, i.e Ω is close to one. In fact, measurements of the CMB anisotropy power spectrum confirmed that $\Omega = 1.000 \pm 0.017$, (Planck Collaboration et al., 2015b). Another problem related to the model is the horizon problem. CMB photons emitted from distant regions of the sky appear to be in thermal equilibrium at almost the same temperature. Yet there was no time for those regions to interact before the photons were emitted. Both of these problems can be resolved by introducing inflation (see, Liddle (1997) for a review on Inflation).

The basic assumption of inflation is a a brief period of great expansion – a factor of greater than 10^{27} growth in the time of order 10^{-32} seconds – at the early stage of the Universe. This inflation phase is able to account for the flatness problem because $\Omega = 1$ is the direct consequence of the theory (Guth, 1981). The theory of inflation is able to resolve the horizon problem because before inflation took place the regions, from where CMB photons were emitted, were close enough to each other to be able to interact.

Another possible confirmation by claimed detection of CMB polarisation induced by gravitational waves in early universe has been provided by BICEP2 (Ade et al., 2014). However, this detection is still controversial (BICEP2/Keck et al., 2015). Recent Planck results seem to go against natural inflation as they show that it is dominated by polarised dust emission with an upper bound on the tensor-to-scalar ratio of $r < 0.12$ (Planck Collaboration et al., 2015a).

Dark Matter

Another important addition to the model, necessary to explain many observations, is the assumption that most of the matter in the universe is dark and non-baryonic.

Fritz Zwicky (1933) observed clusters of galaxies and found that in general the mass required to keep a galaxy cluster gravitationally bounded is much higher than the sum of the masses of galaxies within the cluster. Another observation that suggests the existence of dark matter is the rotation curves in spiral galaxies (Trimble, 1987), where the velocities of the stars cannot be explained by the observed mass of the galaxy.

Further evidence of dark matter is provided by CMB studies of anisotropies. Anisotropies in the matter distribution of 10^{-5}, assuming that they are same order of magnitude as temperature distribution anisotropies, are not sufficient to give rise to the structures we see today (Padmanabhan, 1995). To explain this structure formation, it is necessary to assume the existence of non-baryonic matter that is not linked to photons and for this reason can have larger anisotropy at the recombination epoch from which the cosmic structures have formed.

BBN predicts that the amount of baryonic matter cannot be greater than $\Omega_B \sim 0.02$ (Kolb and Turner, 1990), and this is confirmed by CMB anisotropy studies, which estimate $\Omega_B h^2_{100} = 0.02226 \pm 0.00023$ (Planck Collaboration et al., 2015b). This value of Ω_B is unable to account the for the observed mass in galaxies and clusters of galaxies. This means that most of the matter present in the Universe must be of the non-baryonic nature.

The presence of dark matter is further suggested by gravitational lensing studies. These studies allow us to probe the matter distribution and, in some cases (e.g. the Bullet cluster), it is found that the bulk of is located in a different position to that of the baryonic matter (Bradač et al., 2006; Clowe et al., 2006).

Finally, the CMB anisotropy measurements show that the amount of matter in the Universe is $\Omega_m = 0.308 \pm 0.012$ (Planck Collaboration et al., 2015b). Comparing this value to Ω_B, it is clear that the amount of matter is 10 times larger than that of baryonic matter.

At present, some hypotheses on the nature of dark matter include that it may be constituted of neutralinos (Bertone et al., 2005), axions (Skivie, 2009) and sterile neutrinos (Abazajian et al., 2007).

Dark Energy

To account for a static universe, Einstein included a parameter in his equations of general relativity called the cosmological constant (Eq. 1.4). After the discovery of the expansion of the universe this term was dropped up until the discovery, by means of the observation of supernovae Ia, that the universe was accelerating in its expansion (Perlmutter et al., 1999). This acceleration can be explained by the cosmological constant or more generally speaking

by a dark energy component which drives the accelerated expansion. The amount of dark energy is estimated by means of CMB anisotropy power spectrum estimations from Planck measurements to be $\Omega_\Lambda = 0.692 \pm 0.012$ (Planck Collaboration et al., 2015b).

Presently, the nature of the dark energy component is not understood. There are some hypotheses related to vacuum energy or quintessence (e.g. Peebles and Ratra (2003)). The equation of state in a general form is:

$$p = w\rho \tag{1.9}$$

where if $w < -1/3$ it gives rise to accelerated expansion. If $w = -1$ then we get a cosmological constant that is assumed to be the energy density of empty vacuum. In the general case with $w \neq -1$, its effect can be associated with a dynamical field (quintessence), i.e. it can vary with time.

One problem associated with dark energy is the value associated with this field because there is a large difference between the measured value and the predicted value. The measured value is approximately 7×10^{-30}g cm^{-3}, which is over 120 orders of magnitude smaller than the predicted value (see Steinhardt & Turok (2006)). Another problem is known as the "coincidence problem", constituting the fact that matter and dark energy have different evolutions with redshift. It is expected that at very high redshift the dark energy is negligible while in the future it is expected to be the dominant component. For this reason it is difficult to explain why we are observing in the moment where the effects from both are comparable (Bousso, 2012).

1.3 Cosmological Structure Formation

Current observations of the local universe reveal that the Universe is not homogeneous from very small scales, for e.g., that of our solar system, to large scales of the order of superclusters of galaxies (size 100 Mpc or more).

Due to the attractive nature of gravity, galaxies tend to group together into gravitationally bound structures. Small groups of galaxies have been observed, containing 10 to 100 galaxies. Larger groups, containing approximately 100 to 1000 galaxies, are known as clusters of galaxies. Approximately 10% of all observed galaxies are known to belong to clusters. Most of the observed clusters were discovered with optical images and a significant number of them by imaging the x-rays emitted by hot intracluster gas. Galaxy clusters themselves

have been known to group together into even larger structures called superclusters. In 1937, Holmberg identified the supercluster that contains our galaxy, which was later characterised by de Vaucouleurs in 1953. The study of the distribution of galaxies in 3 dimensional space has revealed other interesting features such as voids (regions devoid of bright galaxies of size $30h^{-1}$ Mpc) and great walls of galaxies that stretch across a significant fraction of the sky and appear to be separated by about $100h^{-1}$ Mpc. Our current knowledge of the large structures of the universe is presented in Fig. 1.5 below.

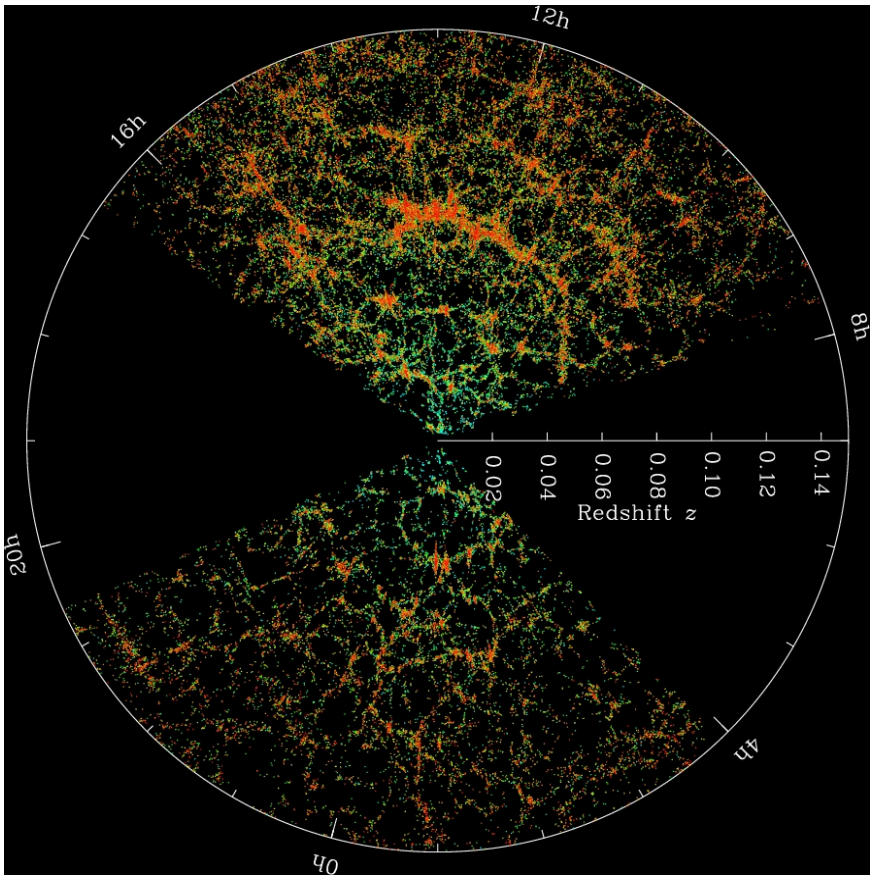

Figure 1.5: Large-scale structure in the Universe traced by bright galaxies: a 3D map of the universe by SDSS, where each dot represents a galaxy.

To understand these structures, several surveys have been carried out that have observed a large area of the sky producing a 3D map. One of the biggest known surveys is the Sloan Digital Sky Survey (SDSS) in operation since 1998 (Eisenstein et al., 2011). This survey created the most detailed three-dimensional maps of the Universe ever made (see Fig. 1.5), with deep multi-colour images of one third of the sky, and spectra for more than three million astronomical objects. Using the light from quasars the SDSS is able to map further distances. Other surveys carried out were, for example, the 2dF Galaxy Redshift Survey (2dFGRS)

which measures the redshift of approximately 250000 galaxies (Colless et al., 2001) and the Centre for Astrophysics (CfA) redshift survey (de Lapparent et al., 1986; de Lapparent et al., 1988).

Significant advances in our understanding of the Universe and structures within it have been made by cosmological numerical simulations. One example of this is Millennium Simulations, the largest N-body simulation ever (Springel et al., 2005). The simulation, containing 10 billion particles, was carried out by the Virgo Consortium using a cluster of 512 processors located at the Max Planck Institute for Astrophysics in Garching, Germany. The aim of this simulation was to trace the evolution of matter distribution in a cubic region of the Universe. The results of the simulation are in agreement with current observations and show that at the present time the structures are abundant in the Universe manifesting themselves as stars, galaxies and clusters (see Fig. 1.6).

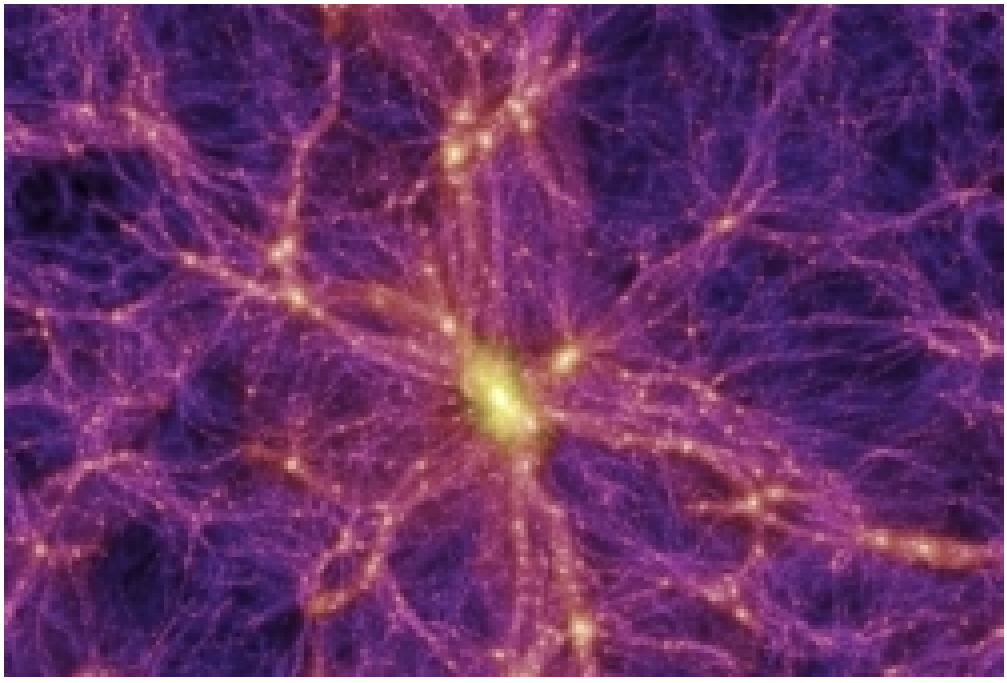

Figure 1.6: A 3D visualisation of the Millennium Simulation at redshift $z = 0.0$. Credit: *Max Planck Institute for Astrophysics*

Large surveys and large simulations reveal that the Universe at small scale is inhomogeneous, however the Universe at large scale is known to be homogenous and isotropic. Direct evidence comes from the smoothness of the temperature of the CMB and the anisotropy of order $\frac{\delta T}{T} \sim 10^{-5}$.

There are two possible ways in which structures could have formed, namely the top-

down and the bottom-up scenarios (Kolb and Turner, 1990). In the top-down scenario, large structures the size of galaxy clusters formed first then later fragmented into galaxies. This is based on the principle that radiation smoothed out the matter density fluctuations to produce large sheets. These sheets then accreted matter after recombination and grew until they collapsed and fragmented into galaxies.

The competing scenario, bottom-up, is one where dwarf galaxies were formed first and then merged into galaxy clusters. In this scenario the density enhancements at the time of recombination were close to the size of small galaxies today. Due to gravity these enhancements collapsed to form dwarf galaxies and these galaxies then merged by gravitational attraction to from larger galaxies and similarly these larger galaxies merged together to form filaments and clusters.

A combination of present observations and theory point towards the bottom-up scenario. This process is driven by dark matter. There are two possibilities with regards to dark matter: Hot Dark Matter and Cold Dark Matter. Hot Dark Matter is formed by relativistic particles at the recombination epoch, whereas Cold Dark Matter is formed by non-relativistic particles at the epoch of recombination. Present observations and theories suggests that Cold Dark matter is a good scenario (Kolb and Turner, 1990).

Structure formation can be described by linear perturbation when $\frac{\delta\rho}{\rho} << 1$ (Padmanabhan, 1995). When the density contrast grows and is close to 1, it is no longer linear and hence requires a complex solution which can be obtained with semi-analytical or numerical methods. One example of this is when modelling the formations of galaxy clusters.

1.4 Formation and Evolution of Galaxy Clusters

In the early universe the density fluctuation field is assumed to be a homogeneous and isotropic Gaussian. The initial primordial density field is characterised by the density contrast field: $\delta(x) = (\rho(x) - \rho_m)/\rho_m$, where ρ_m is the mean mass density of the Universe. It is believed that the clusters of galaxies are formed when the localised peaks in this field become gravitationally unstable and collapse (Peebles, 1980). The evolution of clusters of galaxies can be followed by using the simple spherical collapse model (Colafrancesco and Vittorio, 1994; Colafrancesco et al., 1994; Colafrancesco et al., 1997).

According to this model, a homogeneous, spherical perturbation detaches from the Hubble flow at time $t_m = [3\pi/32G\rho_b(t_m)]^{1/2}$, where $\rho_b(t_m)$ is the cosmological background density when $\delta_m = 1.06$. It collapses at time $t_c \approx 2t_m$ when $\delta_c = 1.69$, and reaches virial equilibrium

at time $t_v \approx 3t_m$ when $\delta_v = 2.2$ (δ_v independent of t_v). Under the assumption of linear growth the density contrast at virial equilibrium time is $\delta_v = \delta_{i,v} D(t_v)/D(t_i)$, where $D(t)$ is the linear growth factor in the chosen cosmology (see, Colafrancesco et al. (1997)). The non-linear density contrast of a cluster that virializes at a given redshift z is described by $\Delta(\Omega_0, z) = 18\pi^2/[\Omega_0(H_0 t)^2(1+z)^3)]$, where $\Delta = \rho/\rho_b$ (≈ 400 for a flat universe) with ρ being the density of perturbation and ρ_b the density of the background at t_v.

A statistical model for the abundance of collapsed objects as a function of their mass and redshift was pioneered by Press & Schechter (1974). This model by Press & Schechter provides a direct relationship between the mass function of the objects resulting from nonlinear collapse to the statistical properties of the the linear density contrast field. The reader is referred to Colafrancesco & Vittorio (1994) and references therein, for the derivation of the mass distribution as well as the discussion on selection criteria for nonlinear structures and cloud-in-cloud problems. The mass distribution by Press & Schechter is described as the number density of the objects at a given redshift z that have masses in range (M, $M + dM$):

$$N(M, z) = -\frac{\rho_b}{M}\frac{\delta_v}{\sigma^2}\frac{d\sigma}{dM}\frac{1}{\sqrt{2\pi}}\exp\left(-\frac{\delta_v^2}{2\sigma^2}\right) \tag{1.10}$$

where $\sigma(M, z)$ is the standard deviation of the linear density fluctuations at redshift z, smoothed over the region containing mass M.

Numerical models can be used to investigate the evolution of clusters of galaxies as a result of merging events (e.g. Roettiger et al. (1998)). These models were implemented to explore the underlying hydrodynamical processes that produced the observed morphological features. These investigations were carried out using hydrodynamical/N-body simulations and then following the development of these features by allowing the evolution of merging. In this way it was possible to obtain some insights into the more general evolution of galaxy clusters and hence more details about large scale structure formation.

Being the largest virialised structures in the Universe, clusters of galaxies are of particular interest for cosmological studies. Clusters are the result of a hierarchical formation process, in which clusters are the last objects to form and are, therefore, localised close to their formation place. The counts of these gravitationally bound structures as a function of mass and redshift is important for tracing large scale structures and to understand properties of the universe (e.g., Colafrancesco et al. (1997)). In the next section observations of these cosmological indicators are described in detail.

1.5 Phenomenology of Galaxy Clusters

1.5.1 Optical band

Galaxy clusters are the largest and most recent virialised structures in the Universe containing 100-1000 galaxies each (Sarazin, 1988). Galaxy clusters were first catalogued based on visual inspection of photographic plates from the Palomar Observatory Sky Survey by George Abell (1958). Clusters were further categorised using two properties: richness (the number of galaxies within detection aperture) and distance. This catalogue was then extended to the southern sky by Abell, Corwin & Olowin (1989), and it contained a sample of more than 4000 clusters. The Abell catalogue is widely used to classify and characterise galaxy clusters. The clusters in the catalogue were labelled with "A" followed by the number of a cluster. There were also earlier studies of clusters by Zwicky, Herzog & Wild (1961), but these were of poor galaxy systems.

Figure 1.7: The Perseus cluster of galaxies, one of the closest clusters of galaxies containing approximately 1000 galaxies. Image credit: Ken Crawford (Rancho Del Sol Observatory)

Initially clusters were classified into two categories, i.e., regular and irregular, based on their morphology. Regular clusters are spherically symmetrical with a pronounced central concentration of galaxies whereas irregular clusters lack symmetry and concentration of galaxies at the centre of the cluster. In fact, irregular clusters exhibit a significant number of subclusters within. The other distinction between regular and irregular clusters is that regular

clusters are generally rich in galaxies whereas the irregular clusters can be rich or poor. A typical example of a cluster that is regular and rich in galaxies is Coma (A1656). Virgo is an example of an irregular shaped cluster yet rich in galaxies. In the following images the properties described above are clearly present for each cluster.

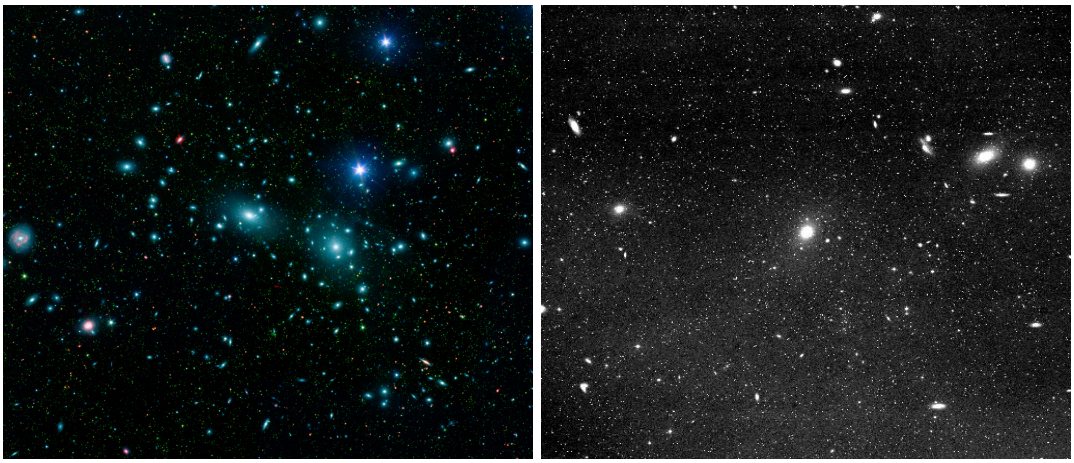

Figure 1.8: Image on the left is regular and rich cluster COMA: Image credit: NASA/JPL-Caltech/GSFC/SDSS. On the right is the image of Virgo cluster (Image credit: http://messier.seds.org/more/virgo˙pix.html), it is clearly irregular yet rich in galaxies.

A further morphological classification of clusters was pioneered by Bautz & Morgan (1970) and Rood & Sastry (1971). The galaxy clusters were binned according to the degree of domination by the brightest galaxies (Bautz and Morgan, 1970). Clusters that are dominated by a single cD galaxy (a galaxy with bright nucleus and extended halo) at the centre were binned into Type I. Clusters dominated by luminous intermediate type of galaxy, between cD and elliptical, were binned into Type II and clusters not dominated by any galaxy were grouped into Type III. If the clusters could not be characterised according to these bins then they were further binned into intermediate groups I-II and II-III. Rood and Sastry binned clusters according to the distribution of brightest galaxies in a cluster. The morphological bins cD, B, L, C, describe a cluster dominated by a single galaxy (A2199), a pair of galaxies (Coma), three or more bright galaxies arranged along a straight line (Perseus), and four or more luminous galaxies at the core (A2065) respectively. Clusters with a flat distribution (A2151) or uneven distribution (Virgo) of galaxies were placed into bins F and I respectively.

A general approximation of the distribution of galaxies in a regular cluster is:

$$n(r) = n_0[1 + (r/r_c)^2]^{-3/2}, \tag{1.11}$$

where r_c is the size of the central region of the cluster (King, 1962).

1.5.2 The intra cluster medium in X-ray band

Luminous X-ray sources were first detected in Virgo (Byram et al., 1966; Bradt et al., 1967), Perseus (Fritz et al., 1971; Gursky et al., 1971a) and Coma (Meekins et al., 1971; Gursky et al., 1971b) clusters. These observations show that galaxy clusters are extremely luminous in this spectral band and suggest that X-ray emission may be a common feature (Cavaliere et al., 1971). However, this hypothesis was only tested when a full sky survey in X-ray band was catalogued using the Uhuru satellite (Giacconi et al., 1972; Giacconi et al., 1974; Forman et al., 1978). The observations of Uhuru provided a better understanding of the properties of X-ray sources related to clusters. Gursky et al. (1972) and Kellogg et al. (1971; 1973) were the first to identify clusters among the observed Uhuru sources. From these observations it was deduced that clusters of galaxies are very luminous X-ray sources, with luminosity $\sim 10^{43}$ erg/s to 10^{45} erg/s, and the X-ray sources related to clusters of galaxies have extended emission (see Fig 1.9) that is not associated with an individual component of the cluster and does not vary with time (Elvis, 1976).

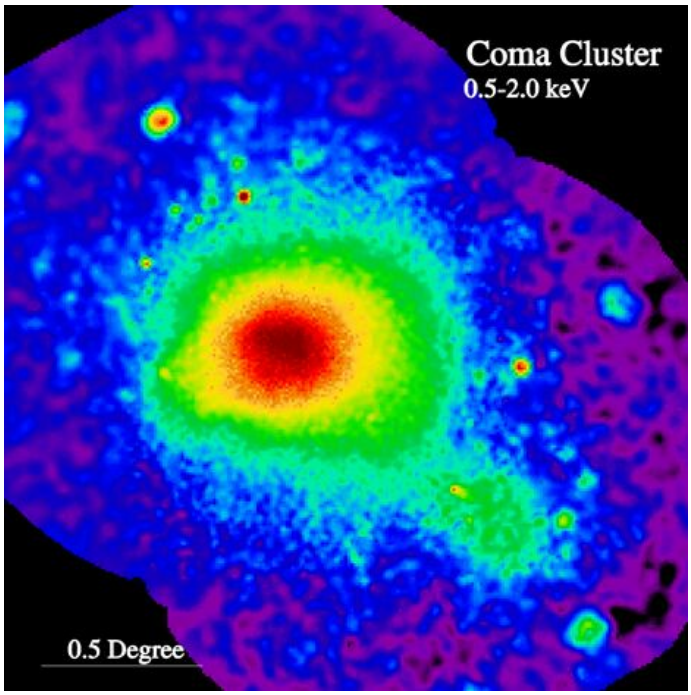

Figure 1.9: X-ray image of the Coma cluster from ROSAT. Image Credit: MPE

Initially, there was a fair uncertainty in the origin of X-ray emission, i.e it was not clear if the X-ray emission was of thermal or non-thermal origin. This uncertainty was due to the fact that the observed X-ray emission could be interpreted as thermal emission (bremsstrahlung emission) from a hot gas as well as non-thermal X-ray emission produced by Inverse Compton

Scattering (ICS) of the cosmic microwave background (CMB) by relativistic electrons in previously discovered radio halos (Perola and Reinhardt, 1972). The detection of the emission features resulting from transitions of highly ionised iron in the spectra of 18 clusters provided further evidence of thermal origin (Mitchell et al., 1976; Serlemitsos et al., 1977; Mitchell and Culhane, 1977; Berthelsdorf and Culhane, 1979; Mushotzky et al., 1978; Mushotzky and Smith, 1980). The presence of the iron line was later confirmed by Rothenflung & Arnaud (1985) to be a common feature in the spectrum of X-ray galaxy clusters (see for example Fig. 1.10) and thus thermal X-ray emission is a general property. The thermal origin of the X-ray emission implies that the space between the galaxies in a cluster must be filled by diffuse hot gas ($T \sim 10^8$ K), referred to as Intra Cluster Medium (ICM) with density as low as $n_{th} \sim 10^{-3}\mathrm{cm}^{-3}$ and total mass greater than that of the luminous material contained in galaxies.

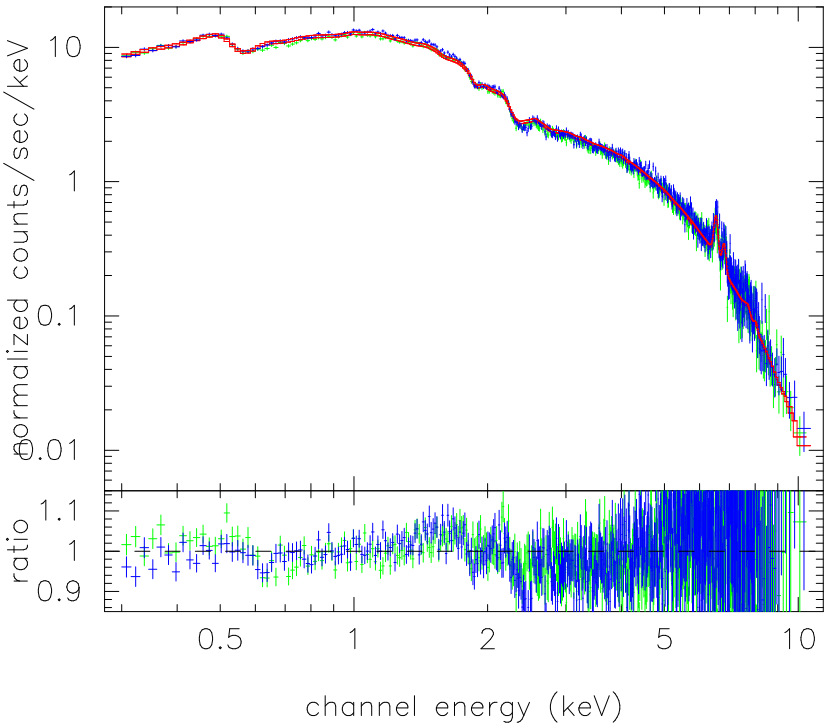

Figure 1.10: X-ray spectrum of Coma cluster taken with XMM (Arnaud et al. 2001). Note the iron line feature at ~ 7 keV suggesting evidence of thermal origin of this emission.

The two characteristics of ICM, density and temperature, are obtained using X-ray observations. The shape of the spectrum determines the temperature whereas the normalisation provides the density. The thermal emission model is used to fit the observed spectrum (obtained from instruments sensitive up to energies greater than 10 keV) to obtain the gas temperature (Arnaud, 2005). At low energies the spectral shape of thermal bremsstrahlung

emissivity is not very sensitive to temperatures (Longair, 1994) and therefore the gas density distribution can be obtained from X-ray images or surface brightness profiles (see, Fig. 1.11) extracted from the soft energy band (E $\leq$ 2 keV). The isothermal beta model by Cavaliere & Fusco-Femiano (1976) provides a good approximation to the distribution of hot gas density. This model assumes a constant temperature and a spherically symmetrical radial profile:

$$n_{th}(r) = n_{th,0}\left[1 + \left(\frac{r}{r_{c,th}}\right)^2\right]^{-3\beta_{th}/2} \tag{1.12}$$

where $n_{th,0}$ is the density at the centre of the cluster, $r_{c,th}$ is the radius of the core and β_{th} is the gradient of descent for $r > r_{c,th}$. This is given by $\beta_{th} = \frac{\mu m_p \sigma_r^2}{kT}$, where μ is the average molecular weight with units of atomic mass, m_p is the mass of proton, T is temperature and σ_r is the galaxy velocity dispersion.

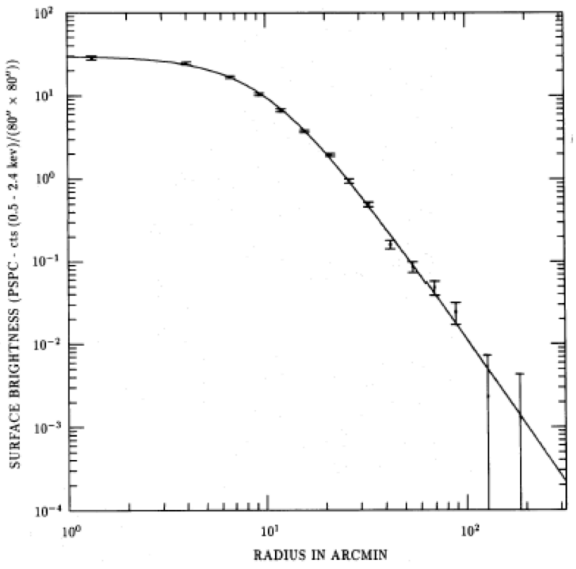

Figure 1.11: Surface brightness profile of Coma obtained by ROSAT (Briel et al., 1992).

Applying this model to 46 clusters of galaxies Jones & Forman (1984) found that the surface brightness profile of the hot gas in $\sim 2/3$ of their samples could be well approximated by this model. The expression for the angular profile of the surface brightness of the X-ray emission is:

$$S(\theta) = S_0\left[1 + \left(\frac{\theta}{\theta_{c,th}}\right)^2\right]^{-3\beta_{th}+1/2}, \tag{1.13}$$

here $\theta_c = r_{c,th}/D$, in radians, where D is the distance to the cluster. The distribution of the hot gas when $\beta_{th} \leq 1$, is wider compared to that of the luminous matter. This suggests that the heating of gas may take place by mechanisms such as merger events in the peripheral zones of galaxy clusters.

In the remaining 1/3 of the sample considered by Jones & Forman (1984), a large dispersion in the central region linked to the presence of cooling core was observed. Outside the central region the surface brightness profile is well fitted by the β - model. The cooling flow is formed in the central region of the ICM that continuously emits bremsstrahlung radiation with cooling time $t_{cool} \approx T^{1/2}/n_e$. In the centre of the galaxy cluster n_{th} is high and the cooling time is low. When t_{cool} is shorter than the age of the cluster cooling takes place and it is pushed to the centre of the cluster by the pressure of the surrounding gas. This drop in temperature is confirmed by both Chandra (Allen et al., 2001) and XMM-Newton observations (Kaastra et al., 2004).

The currently debated problem of cooling flow is that the temperature of the cooling gas at the centre of the galaxy is of order half of that found further out in the cluster while the expected value is much lower (Peterson et al., 2003). This phenomenon is observed, for example, in the following clusters: A1795 (Tamura et al., 2001), Hydra (David et al., 2001), A2029 (Lewis et al., 2002) and A2052 (Blanton et al., 2003). To understand this phenomenon many hypotheses are proposed in literature, such as the action of the heating by AGN (Böhringer et al., 2002; Kaiser and Binney, 2003), the effect of heating of the gas produced by cosmic rays (CR) accelerated by bipolar jets produced in the explosion of supernovae (Colafrancesco et al., 2004) and that they act as warming rays (Colafrancesco and Marchegiani, 2008). Other possibilities are AGN jets and lobes, pressure waves, buoyant bubbles and cavities, intra-cluster shock waves, as well as leptonic and hadronic cosmic-rays (see, e.g., (Böhringer et al., 2002; Churazov et al., 2002; Ruszkowski and Begelman, 2002; Fabian, 2004; Voit and Donahue, 2005; Brüggen and Kaiser, 2002; Ruszkowski et al., 2004; Vernaleo and Reynolds, 2006; Reynolds et al., 2005; Colafrancesco and Marchegiani, 2008)).

Significant progress in understanding the cluster as a whole was made by means of X-ray imaging using Einstein Observatory, ROSAT, ASCA, Chandra and XMM-Newton. With these instruments it was observed that the morphology of galaxy clusters varies from regular to complex systems with multiple substructures (Jones and Forman, 1992). If the sub-cluster is falling towards the main cluster a merging event is expected (Briel et al., 1991). The ROSAT observation of the gas compression in the sub-cluster of A2256 provided a first signature of a merger event. Further evidence of this event was provided by ASCA observation of a temperature increase in the interaction region between the sub-clusters of Cygn-A (Markevitch

et al., 1999). Merging of sub-clusters compresses and heats up the interacting regions. A shock is driven in ICM due to the moderately supersonic ($v \sim 2000$ km/s) motion of mergers. As a result, the gas of the final cluster is heated to its virial temperature, which is higher than the virial temperatures of the initial sub-clusters (Arnaud, 2005). An excellent example of a shock is present in the merging cluster 1E0657-56, known as the Bullet cluster (Markevitch et al., 2002).

Further observations by Chandra led to the discovery of substructure, cold fronts in merging cluster, initially discovered in A2141 by Markevitch et al. (2000) and in A3667 by Vikhlinin et al.(2001). Cold fronts are contact discontinuities between the cool core of a subcluster moving at near sonic velocity and the surrounding main cluster gas. Both shocks and cold fronts are observed in the cluster 1E0657-56 (see, Fig 8 and 9 from (Arnaud, 2005)). Chandra's arc-second spatial imaging also led to the observations of the complex interaction between AGN activity in the cluster centre and the ICM. X-ray cavities, known as bubbles, are created by the displacement of the X-ray gas by central AGN radio lobes (Blanton, 2004) and are usually dominated by the non-thermal component of clusters (Fabian et al., 2006).

1.5.3 Gravitational lensing

According to general relativity, light observed from a distant source appears to bend, which is explained by the gravity associated with mass concentration (Einstein, 1936). This bending of light when passing the concentrated mass is known as gravitational lensing. There are two types of this phenomenon: weak lensing, detected in the statistical appearance of the background galaxies observed through clusters, and strong lensing explained by strong distortions and multiple images of individual sources. A cluster mass and its distribution is derived by measuring the gravitational shear in a cluster of galaxies (see, Bartelmann (2010) for a further review).

This gravitational lensing effect is observed in some clusters - a good example is the Bullet cluster. From the observation of the Bullet cluster it is noted that the spatial distribution of the cluster mass is different to the distribution of the observed hot gas in X-ray (see Fig. 1.12 below). This is interpreted as the consequence of merging that leads to displacement of gas and dark matter distribution (Bradač et al., 2006; Clowe et al., 2006). This confirms that galaxy clusters are dominated by their dark matter component as suggested by CMB measurements and structure formation theory.

Figure 1.12: A clear representation of gravitational lensing in the Bullet cluster. The difference in the position of cluster mass (blue) and the hot gas (red) is clearly visible. Composite Image Credit: Composite Credit: X-ray: NASA/CXC/CfA/ M.Markevitch et al. (Markevitch, 2005)

1.5.4 Radio band

Using a single dish radio telescope, Large et al. (1959) detected diffuse and extended radio emission in galaxy clusters for the first time. By mapping the Coma cluster at radio wavelengths they detected an extended radio source (Coma C) at the centre of the cluster. Further evidence of the extended radio emission in Coma was provided by Wilson (1970), who compared the data of Large at al. (1959) to interferometric observations. From this data Wilson further determined that the observed radio emission was diffuse and not related to a single galaxy within the cluster. Since then, the presence of non-thermal diffuse radio sources in many clusters have been observed by sensitive radio telescopes (see Fig 1.13). For example giant radio halos were discovered in the clusters A665 (Giovannini and Feretti, 2000), A2163 (Feretti et al., 2001), A2219 (Bacchi et al., 2003), A2255 (Feretti et al., 1997a), A2319 (Feretti et al., 1997b), A2744 (Govoni et al., 2001a), 1E0657-56 (Liang et al., 2000) and CL0016 + 16 (Giovannini and Feretti, 2000). Radio halos of size $<<$ 1Mpc were detected in clusters A401 (Giovannini and Feretti, 2000), A1300 (Reid et al., 1999), A2218 (Giovannini and Feretti, 2000) and A3562 (Venturi et al., 2003). However, this non-thermal extended radio emission is not a common feature of galaxy clusters as it is only present in approximately 10% of the

observed clusters (Ferrari et al., 2008). Nevertheless, when only the most luminous X-ray clusters are considered ($L_{X[0.1-2.4keV]} > 0.6 \times 10^{45} h_{70}^{-2}$ erg s^{-1}) the number of clusters in which the radio emission is observed goes up to $\sim 35\%$ (Giovannini et al., 1999; Giovannini and Feretti, 2002).

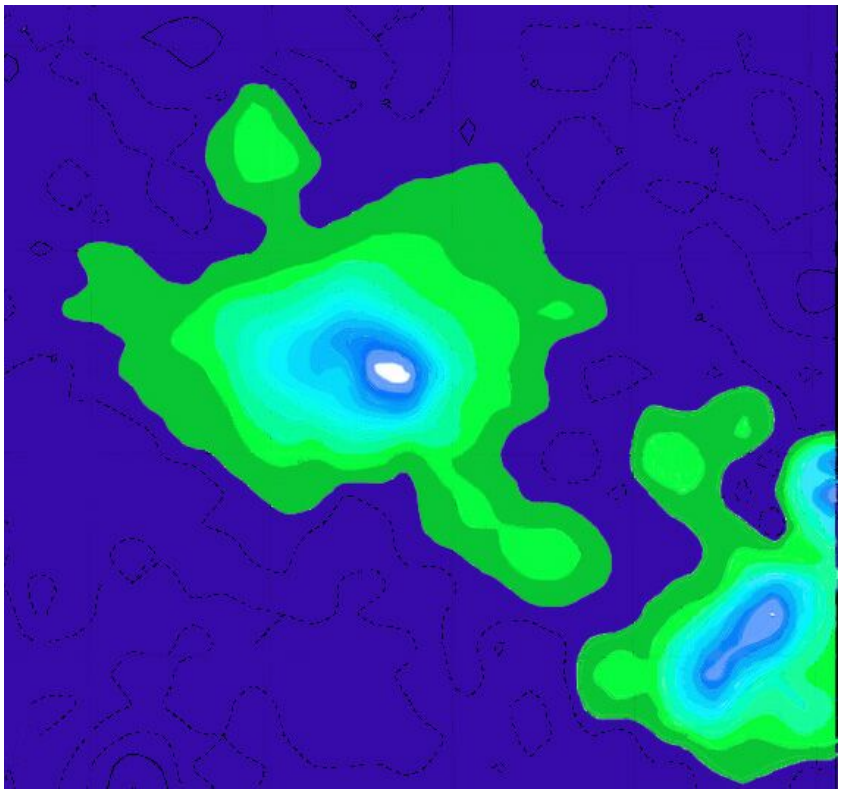

Figure 1.13: Image of radio halo and relic in Coma from Effelsberg Telescope, Deiss et al. 1997

Radio luminosity is correlated with L_x (Bacchi et al., 2003), T_x (Liang et al., 2000), Mass (Govoni et al., 2001a) and Y_{SZ} (Basu, 2012). However clusters at same x-ray luminosity seem to be bimodal with respect to their radio luminosity because there are some clusters with similar x-ray luminosity that show presence of a radio halo in some cases and in other cases show no halo (see Fig. 1.14).

Extensive studies of radio halos at multifrequency is limited by the sensitivity capabilities of current instruments. However, in order to obtain a more accurate integrated radio spectrum and spatially resolved spectral index map a lot of efforts have been put forward to carry out the multifrequency observations. Observations of diffuse emission from radio halos shows that they follow a power-law spectrum, suggesting that these sources are of non-thermal origin due to Synchrotron emission produced by relativistic particles in a magnetic field. Some observations have led to detection of a steepening of the halo spectrum at high frequency:

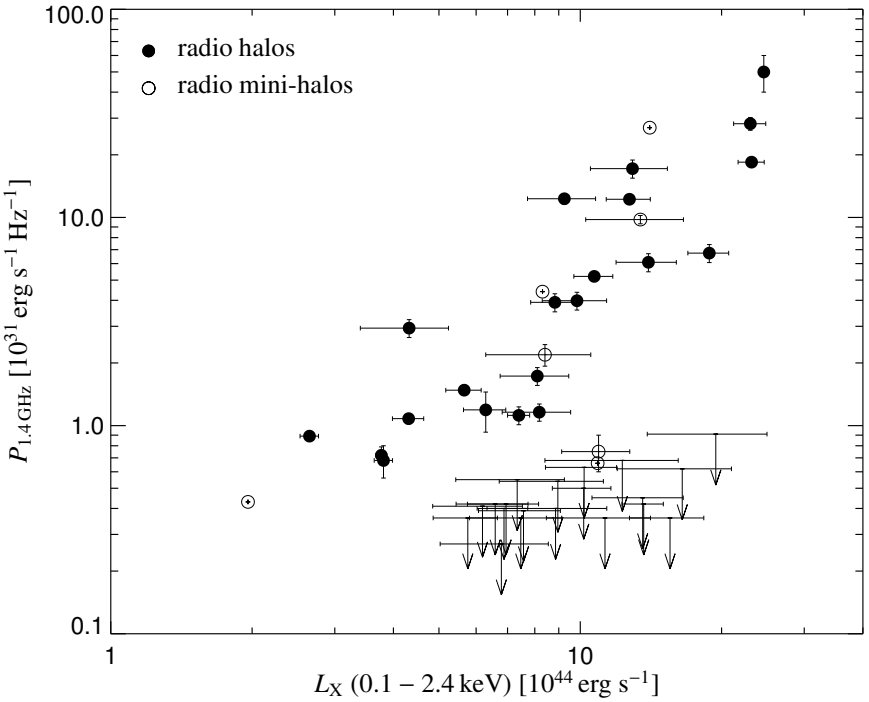

Figure 1.14: A presentation of the bimodal properties of clusters at same X-ray luminosity with respect to their radio luminosity. There is a large number of clusters that do not exhibit halos (Enßlin et al., 2011).

A 2319 (Feretti et al., 1997b), Coma (Thierbach et al., 2003), A 754 (Bacchi et al., 2003) and A 3562 (Giacintucci et al., 2005) (see Fig. 1.15 in the case of Coma cluster). Giovannini et al. (1993) while studying the Coma cluster, point out that the spectral index of the halo spectrum is radially dependent. This dependence was also noted by Ferreti et al. (2004) in cluster A665 and cluster A2163.

Radio/X-ray comparison suggests a similarity but not an exact identity between the morphology of radio halos and the X-ray emission of their host clusters (Deiss et al., 1997; Feretti, 1999; Liang et al., 2000). This similarity is clearly presented by Deiss et al (1997) who compared the azimuthally averaged surface brightness distribution of the diffuse radio halo of the Coma cluster at 1.4 GHz to the fit of azimuthally averaged surface brightness distribution of the X-ray halo observed with ROSAT (see Fig. 1.16. For more details see Deiss et al. (1997) and the references therein).

Studying the physical properties of diffuse and extended radio sources it is clear how sources differ in size, location within the host cluster, intensity of polarised signal, morphology and their association to other cluster properties. The diffuse radio sources are classified into

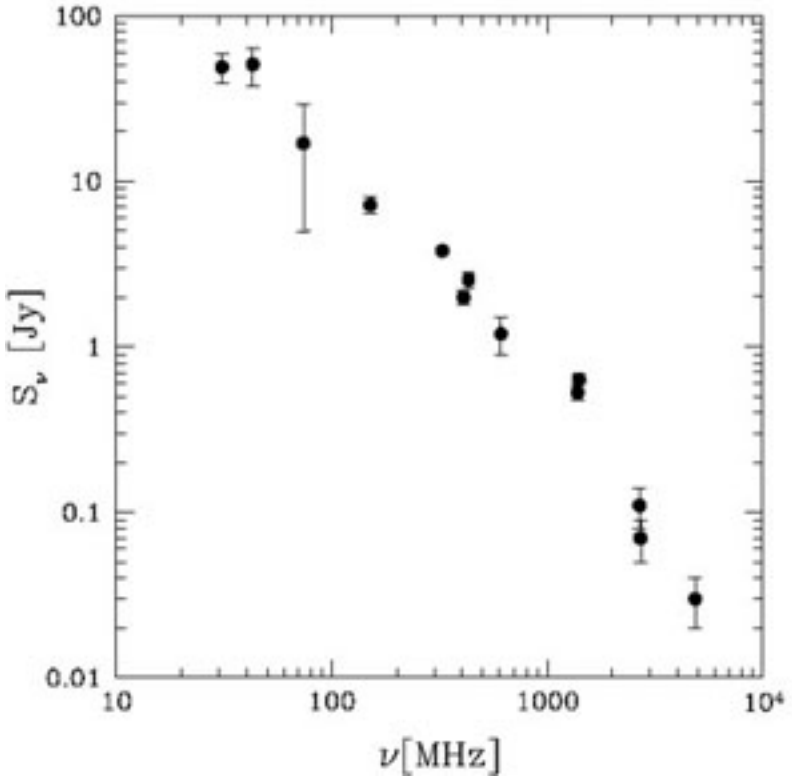

Figure 1.15: Spectrum of the radio halo in Coma cluster, Coma C. The steepening in the spectrum is clear at $\nu > 1000$ MHz (Thierbach et al., 2003).

three main categories: halos, relics and mini-halos. Radio halos have regular morphology and are usually situated at the centre of the host cluster whereas relics are elongated and located in the outskirts of clusters (also detected in merging clusters). Intensity of the polarised signal in radio halos is low whereas it is high in relics. This suggests that these two sources have different origin. Some evidence of relics in clusters are, A2256 (Bridle and Fomalont, 1976; Rottgering et al., 1994), A2255 (Burns et al., 1995; Feretti et al., 1997a), A1300 (Reid et al., 1999), A2744 (Govoni et al., 2001a), A754 (Bacchi et al., 2003; Kassim et al., 2001) and A3667 (Rottgering et al., 1997). Radio sources of size $\leq$ 500kpc detected at the centre of the cooling flow clusters are called mini-halos (Ferrari et al., 2008). For example in clusters Perseus (Burns et al., 1992), PKS0745-191 (Baum and O'Dea, 1991), Virgo (Owen et al., 2000) and A2390 (Bacchi et al., 2003) the presence of mini-halos were detected.

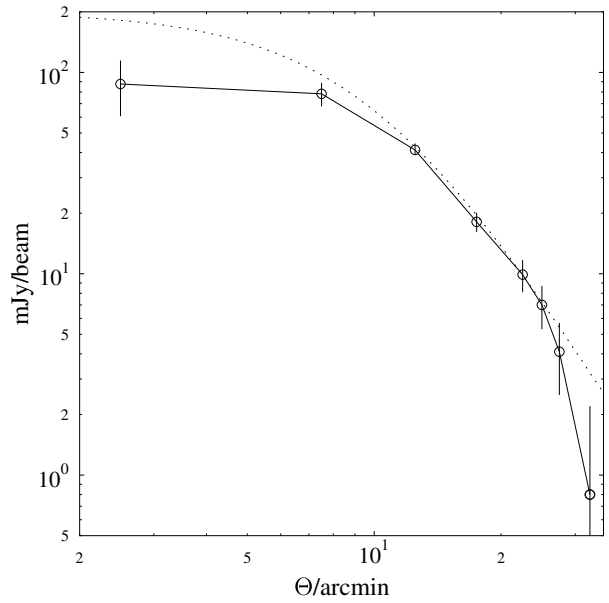

Figure 1.16: Dotted line represents the surface brightness distribution of the diffuse halo of the Coma cluster at 1.4 GHz, from this it is clear that the radial distribution is similar to surface brightness distribution of the X-ray halos (Deiss et al., 1997)

1.5.5 Faraday Rotation Measure

A direct method for measuring the magnetic field in a cluster is provided by the effects produced by the interaction of the magnetic field and the propagation of linearly polarised radiation. In a cluster, the Synchrotron emission from background or embedded sources is a source of linearly polarised radiation. The plane of polarisation of this radiation is rotated when it passes through a magnetised plasma, due to the different phase velocity of the two modes of circular polarisation. This effect is known as Faraday rotation, where the rotation of the polarised field is given by $\Delta\chi = RM\lambda^2$, and the rotation measure (RM) is given by:

$$RM = 0.812 \int_0^L n_e \overrightarrow{B} \cdot \overrightarrow{dl} \,\text{rad m}^{-2} \tag{1.14}$$

(e.g. Carilli and Taylor (2002)) where n_e is the density of electrons in the plasma (10^{-3}cm^{-3}), $\overrightarrow{B}$ magnetic field (μG) and the integral is performed along the line of sight l, with distances expressed in kpc. The density of electrons for a given radio cluster is measured by the x-ray emission from hot gas and can be estimated using the value of RM magnetic field values.

RM studies have been carried out for individual clusters and galaxies by analysing detailed high resolution RM images (e.g. (Perley and Taylor, 1991; Taylor and Perley, 1993; Feretti

et al., 1995; Feretti et al., 1999; Govoni et al., 2001b; Taylor et al., 2001; Eilek and Owen, 2002; Murgia et al., 2004; Govoni et al., 2006; Taylor et al., 2007)). These analyses deduced that the RM distribution of radio galaxies in interacting and relaxed clusters produce magnetic fields with rather small fluctuation scale ($\sim$ 10 kpc or less). Radio galaxies at the centre of relaxed clusters have extreme RM, with the magnitude of the RM roughly proportional to the cooling flow rate. Strong magnetic fields are derived in the high density cooling-core regions of some clusters, with values exceeding $\sim 10\mu$G (e.g., in the inner region of Hydra A, a value of $\sim 35\mu$G was deduced by Taylor et al. (2002)).

Magnetic field strengths in radio halo clusters were measured to be lower. For example, Kim et al. (1990) derived a magnetic field strength of $\sim 2\mu$G when analysing RM maps (at $\sim$ 9.2kpc resolution) for 18 bright radio sources in the Coma cluster region. However, Feretti et al. (1995) deduced a magnetic field of strength of $\sim 6\mu$G from the average value of RM and its dispersion across the source. Recent studies of magnetic field in Coma by Bonafede et al. (2010) provide a range of central magnetic filed strengths (3.9 μG – 5.4 μG) on an uniformity scale range ($\sim$ 2kpc – $\sim$ 34kpc). They also found that the magnetic field power spectrum is well represented by a Kolmogorov power spectrum, which is:

$$P(k) = P(k_0) \left(\frac{k}{k_0} \right)^{-5/3} . \tag{1.15}$$

Magnetic field strength in clusters is observed to be approximately zero out of the halo region, that is magnetic field is detected up until the end of the halo radius (Clarke et al., 2001). Rave et al. (2013) derived the magnetic field strength in the inner region of the halo and found it to be approximately constant.

Other techniques to estimate the values of magnetic fields in galaxy clusters are: equipartition between electrons and magnetic fields in radio halos, comparison between synchrotron and inverse Compton emissions, the study of cold fronts and the GZK limit. The values obtained from these studies are extremely variable, ranging from ~ 0.1 μG to ~ 10 μG. However, these values were obtained using basic version of these techniques and refining them it is possible to reconcile these values, pointing toward values of few μG (see, e.g. Carilli and Taylor (2002), Govoni and Feretti (2004)).

1.5.6 Other observations

We expect that non-thermal electrons (that emit radio halos) can produce emission in other spectral bands, such as Extreme Ultra Violet (EUV), Hard X-rays (HXR), and gamma rays

by Inverse Compton Scattering of CMB (Perola and Reinhardt, 1972; Harris and Grindlay, 1979; Rephaeli, 1979) and non-thermal Bremsstrahlung (Enßlin et al., 1999; Sarazin and Kempner, 2000; Blasi, 2000) with nuclei of thermal gas. Up until now there has been no clear evidence of non-thermal emission in these spectral bands in galaxy clusters.

Extreme Ultra Violet

The observations in EUV band have possibly detected excess emission with respect to the thermal gas radiation in some clusters such as Coma (Lieu et al., 1996a), Virgo (Lieu et al., 1996b), A1795 (Mittaz et al., 1998) and A2199 (Bowyer et al., 1998). However, there exists some uncertainty about the detection of this emission as it was only confirmed for the case of Coma and Virgo (Bowyer et al., 1999; Berghöfer et al., 2000). Also the origin of this emission in EUV is not clear, because it can be produced by a second component of the thermal gas (Lieu et al., 1996a) or by the Inverse Compton Scattering (ICS) of relativistic electrons of CMB (Sarazin and Lieu, 1998). Bowyer et al. (2004) claimed that the electrons emitting the ICS radiation in Coma can have secondary origin by hadronic interactions (see section 2.4.3) but this possibility has been excluded by Marchegiani et al. (2007) because in this case an excess of gamma-ray emission will be produced with respect to the available upper limits by EGRET.

Hard X-ray

The excess of HXR radiation was possibly detected in some clusters for example Coma (Fusco-Femiano et al., 1999; Rephaeli et al., 1999), A2256 (Fusco-Femiano et al., 2000), A2199 (Kaastra et al., 1999), A2319 (Gruber and Rephaeli, 2002), A754 (Valinia et al., 1999; Fusco-Femiano et al., 2003b), A119 (Fusco-Femiano et al., 2003a), and Ophiuchus (Eckert et al., 2008). The detection of HXR has been questioned (Rossetti & Molendi (2004), in the case of Coma) because it is not clear if the emission is real or if it is a result of imperfections in analyses of data. Like in the case of EUV, there are some possibilities that could explain the excess in HXR: thermal with high temperature(Eckert et al., 2007), ICS by relativistic electrons (Fusco-Femiano et al., 1999; Sarazin and Lieu, 1998), and non-thermal bremsstrahlung by supra-thermal tail of thermal electron spectrum (Enßlin et al., 1999; Sarazin and Kempner, 2000; Blasi, 2000). The interpretation of bremsstrahlung has been questioned by Petrosian (2001), because it would require unreasonably high energy input for electrons. Also if the ICS interpretation is correct then these electrons cannot be secondary, because they produce strong gamma-rays (Blasi and Colafrancesco, 1999). More recent studies in X-ray of galaxy

clusters performed with recent instruments like SWIFT (Ajello et al., 2009) and NuSTAR (Gastaldello et al. (2014), for the case of Coma), detected upper limits suggesting that there must have been some problems with previous detection of HXR excess.

Gamma-rays

The emission of gamma-rays from galaxy clusters is expected to be high because of several mechanisms that produce this emission, e.g. ICS and non-thermal Bremsstrahlung by relativistic electrons (Blasi and Colafrancesco, 1999), hadronic interactions between thermal and non-thermal protons (Colafrancesco and Blasi, 1998; Marchegiani et al., 2007) and dark matter annihilation (Colafrancesco et al., 2006). However, gamma-rays have not yet been detected in galaxy clusters (Ackermann et al. (2010; 2014)). This implies that either there are problems with proposed models or current observations. Also in observations at very high energy gamma rays ($E \sim TeV$), no galaxy clusters have been detected (e.g. Arlen et al. (2012)).

Sunyaev Zel'dovich effect

Another spectral band where galaxy clusters are observed is the microwave band, where we see the Sunyaev Zel'dovich (SZ) effect, i. e. the distortion in the CMB spectrum caused by ICS in gas of galaxy clusters (Zeldovich and Sunyaev, 1969). Complementary to X-ray measures, the study of SZE performed with the use of relativistic formalism (Colafrancesco et al., 2003) allows us to obtain information on both thermal and non-thermal properties of galaxy clusters (Colafrancesco, Marchegiani and Buonanno (2011b), in the case of the Bullet cluster). Since the SZ effect does not depend on the distance, it can also be used for statistical studies of counts of clusters (Colafrancesco et al. (1994; 1997)) to determine the cosmological parameters like the Hubble constant (Carlstrom et al., 2001) and the evolution of CMB temperatures with the redshift (Battistelli et al., 2002). SZ effects have been observed in several clusters: Coma (De Petris et al., 2002), A2163 (Holzapfel et al., 1997), MACS J0717.5+3745 (Mroczkowski et al., 2012), Bullet (Zemcov et al., 2010) and other references in Birkinshaw (1999). The Planck Collaboration recently published a list of clusters where the SZ effect has been detected (Planck Collaboration et al., 2015b). One example of the measure of the SZ effect in a galaxy cluster obtained by Planck is presented in the Fig. 1.17.

As we have seen above, galaxy clusters are one of the most important objects of study for both astrophysical and cosmological applications. Furthermore, a full understanding of the

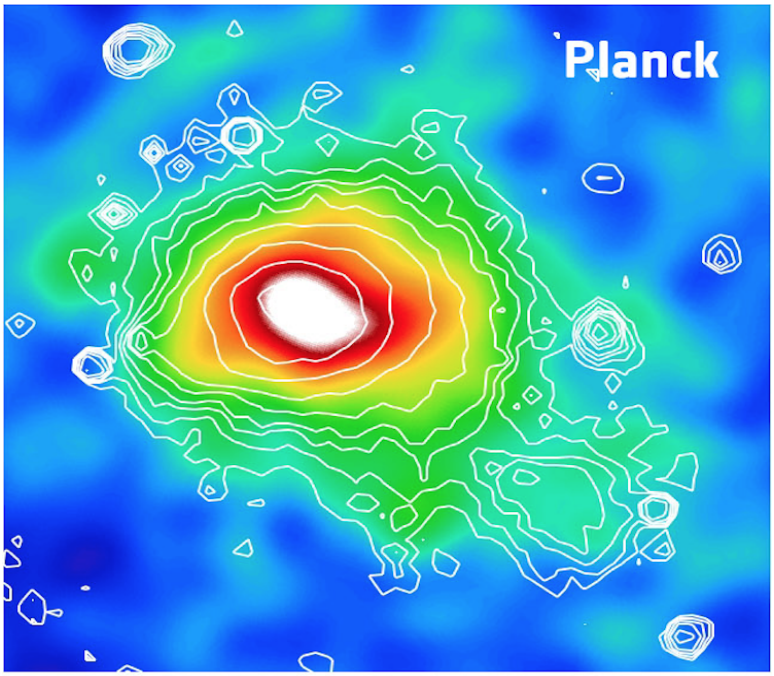

Figure 1.17: Image of Coma cluster through the SZ effect. The colours in the image represents the SZ effect by Planck and the contours show X-ray measured by ROSAT. Image credits: ESA / LFI and HFI Consortia.

properties of galaxy clusters is impossible without a deep understanding of the non-thermal content of these clusters. The discussion above has highlighted that radio halos are the main source of information about the non-thermal component of clusters. We will be primarily interested in the study of radio halos in the remainder of this thesis.

In the following chapter theoretical models will be discussed describing the origin of radio halos as well as extracting information on the physics of galaxy clusters from studies of radio halos.

Chapter 2

Origin of Radio Halos

"To every object there corresponds an ideally closed system of truths that are true of it and, on the other hand, an ideal system of possible cognitive processes by virtue of which the object and the truths about it would be given to any cognitive subject."

-Edmund Husserl

"Too often we hold fast to the clichés of our forebears. We subject all facts to a prefabricated set of interpretations. We enjoy the comfort of opinion without the discomfort of thought."

-John F. Kennedy

2.1 Introduction

Radio halos are extended diffuse radio sources located near the centres of galaxy clusters. The problem of their origin has been a central topic of great debate over several decades. As described in the previous chapter, it is believed that the presence of radio halos implies the presence of relativistic particles and magnetic fields. In order to understand the origin of radio halos, it is therefore necessary to understand the origin and evolution of relativistic particles and magnetic fields.

In this chapter we discuss several theories that have been proposed to explain the injection, acceleration and evolution of relativistic particles, as well as possible mechanisms for the production of magnetic fields. We then present several existing models that may explain the origins of radio halos. For each model we begin with an overview of the general ideas and discuss the observable consequences of the model, as well as known problems and conflicts

with observation. Finally, we propose a new framework that may explain the origins of radio halos. This framework will then be developed further in later chapters.

2.2 The Origin and Evolution of Relativistic Particles

2.2.1 Origin

The injection of relativistic particles (cosmic ray electrons and protons) in galaxy clusters is assumed to have resulted from energy sources such as galactic winds (Völk et al., 1996; Völk and Atoyan, 2000), accretion shocks (Enßlin and Biermann, 1998), merging shocks (Miniati et al., 2001b; Ryu et al., 2003) and radio galaxies (Enßlin et al., 1997). There are two other possible mechanisms for the injection of relativistic electrons: secondary electrons from hadronic interactions (Dennison, 1980; Blasi and Colafrancesco, 1999) and dark matter annihilations (Colafrancesco and Mele, 2001; Colafrancesco et al., 2006). These sources of injections are briefly described below.

Galactic winds are continuous flows of charged particles that blow out of galaxies into the intergalactic medium(Völk et al., 1996; Völk and Atoyan, 2000). In starburst galaxies, they are emitted primarily by supernova explosions and newly formed massive stars. We can estimate that in early galaxies, following the activity of starbursts and the explosion of supernovae, there was a large injection of cosmic rays with energy efficiency of around 10% (Biermann et al., 2003). The energy losses of these relativistic particles are mainly due to adiabatic expansion and therefore it is expected that only a fraction of the original energy is maintained. Hence it would not be realistic to consider galactic winds to be the dominant source for injection of relativistic particles.

During the hierarchical formation of galaxy clusters *accretion shocks* are produced by the accretion of diffuse and cold matter and are expected to be located far in the cluster periphery. These shocks can lead to the acceleration of cosmic rays with an estimated efficiency of 10% of the kinetic energy of the gas in the cluster (Enßlin and Biermann, 1998).

The *merging* of clusters produces very powerful shocks that inject large amounts of energy of order $10^{63} - 10^{64}$ ergs (the order of the content of the thermal energy storage). Hydrodynamic simulations (Miniati et al., 2001b; Ryu et al., 2003) predict that the total energy injected in cosmic rays by shocks from mergers could also be of the order of half the energy dissipated in thermal gas.

Radio galaxies and AGNs also produce a large amount of energy in the form of cosmic

rays. Enßlin et al. (1997) estimated that over the lifetime of a galaxy cluster, radio galaxies inject energetic particles with total energy at least equal to the present-epoch thermal energy content of the central region.

Berenzinsky, Blasi and Ptuskin (1997) compared the rates of energy injected in relativistic particles by the above sources. These authors estimated that the total energy content over the life time of a galaxy cluster due to galactic winds is of order 10^{60} ergs whereas the rate of energy released by accretion shocks as well as radio galaxies is of order 10^{44} ergs s^{-1}.

Due to the presence of non-thermal protons and thermal gas in the ICM, the production of *secondary electrons* is inevitable. Non-thermal electrons are continuously produced over a large region, approximately the size of the cluster, as a result of interactions between relativistic protons and nuclei of the thermal gas (Dennison, 1980; Blasi and Colafrancesco, 1999). The reactions that lead to the production of secondary electrons are described by the secondary electron model (SEM):

$$p + p \rightarrow \pi^{\pm} + X$$

$$\pi^{\pm} \rightarrow \mu^{\pm} + \nu_{\mu}$$

$$\mu^{\pm} \rightarrow e^{\pm} + \nu_{\mu} + \nu_{e}.$$

In the same interactions gamma rays are produced according to the following reactions:

$$p + p \rightarrow \pi^{0} + X$$

$$\pi^{0} \rightarrow \gamma + \gamma.$$

Another possible source of secondary electrons is the *annihilation of dark matter* that results in the production of stable Standard Model particles including electrons, positrons and gamma rays. The possibility that dark matter is composed of neutralino has been studied previously by Colafrancesco & Mele (2001), Colafrancesco et al. (2006). As dark matter is the main component in the mass of galaxy clusters (see section 1.2.3 and section 1.5.3), this emission is expected to be strong.

These mechanisms for the origin of cosmic rays will be considered in detail in section 2.4, where the properties of non-thermal electrons detected from observations of radio halos are compared to the predictions of these theories. However, in order to carry out these comparisons it is important to understand the process that determines the evolution of relativistic

particles after their injection in the cluster.

2.2.2 Evolution

The evolution of relativistic particles after their injection into the volume of a galaxy cluster is determined by the their interactions with the components of the ICM. The evolution of populations of these particles is described by diffusion in a magnetised plasma:

$$\frac{\partial N(r,\gamma,t)}{\partial t} = \nabla \cdot [D(\gamma)\nabla N(r,\gamma,t)] - \frac{\partial}{\partial \gamma}\left[\frac{d\gamma}{dt}N(r,\gamma,t)\right] + Q(r,\gamma,t) \tag{2.1}$$

where $N(r,\gamma,t)$ is the number of particles per unit of volume and energy at time t, $\gamma = E/mc^2$ is the Lorentz factor of the particle, $D(\gamma)$ is the diffusion term that is related to movements within the magnetised plasma,$Q(r,\gamma,t)$ is the source of injection of particles that takes into account all the mechanisms mentioned above, and $d\gamma/dt$ is the change in energy of particles when they interact with components of the ICM (Syrovat-skii, 1959; Sarazin, 1999). These processes lead to either losses ($d\gamma/dt < 0$) or gains ($d\gamma/dt > 0$) in energy. Gains in energy are related to acceleration and re-acceleration processes, which are not well known, however losses are related to well known physical processes described below for relativistic electrons and protons.

Electrons can lose energy by four mechanisms: at low energy the main processes are Coulomb interactions and non-thermal bremsstrahlung with hot gas and at high energy losses are dominated by radiative processes, namely Inverse Compton Scattering (ICS) with CMB photons and synchrotron emission in magnetic fields (see the following chapter for details). Due to these losses it has been found that the electrons have a short life-time with respect to the age of the cluster (see Fig 2.1).

The diffusion path of a particle is given by the distance that the particle may travel in a time equal to its average life, estimated by

$$R_d(\gamma) = \sqrt{4D(\gamma)t_{loss}} \tag{2.2}$$

where $t_{loss} = \gamma/b(\gamma)$ is the life time of electrons (Brunetti et al. (2003)). This expression implies that the electron travel distance within a cluster is $\sim$ 50 kpc which is very small compared to the typical size of a radio halo ($\sim$ Mpc).

The main channels of energy loss for protons are the hadronic (at high energy) and

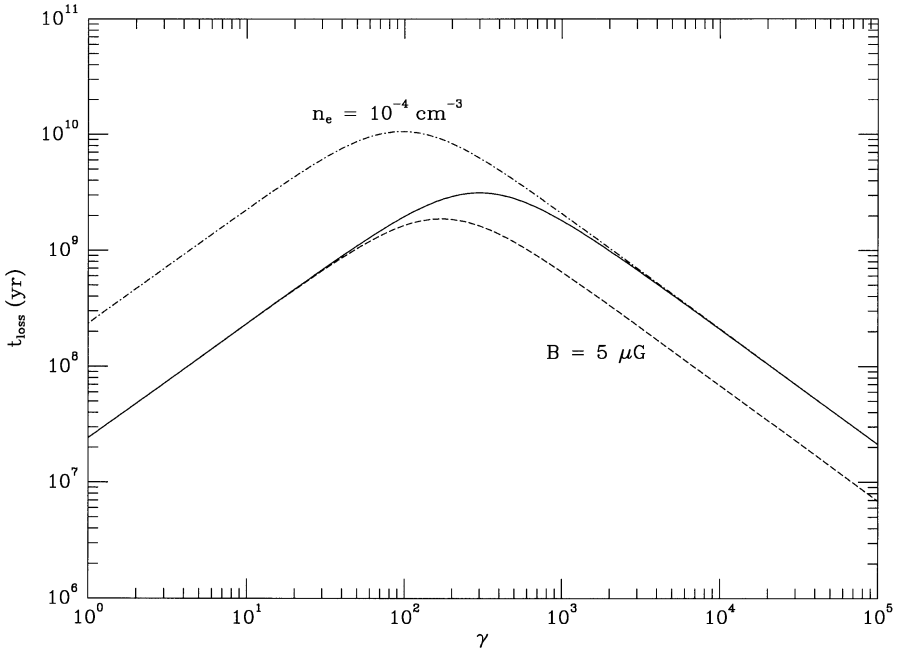

Figure 2.1: A plot of the life time of electrons as function of their energy from Sarazin (1999), for magnetic field $B = 1\mu$G with electron density $n_e = 10^{-3}$cm^{-3} (solid curve) and with $B = 5\mu$G (dashed) as well as $n_e = 10^{-4}$cm^{-3} (dot-dashed)

Coulomb (at low energy) interactions with hot gas (Brunetti et al., 2004). The time scale of these processes at the centre of a cluster is of the order of tens of billions of years. This implies that these protons do not lose a significant fraction of their energy over a very long time (approximately the age of the universe), hence they travel within the cluster and remain confined unless their energy is of the order of 1 TeV, above which they can escape from the cluster (Berezinsky et al., 1997).

2.3 Origin and Evolution of Magnetic Fields

It is still a matter of debate precisely which processes underlie the origin and evolution of magnetic fields in the ICM. Perola & Reinhardt (1972) found the adiabatic compression of magnetic fields in the intergalactic medium (IGM) to have an intensity of $B_{IGM} > 10^{-9}\mu$G (Carilli and Taylor, 2002). Subsequently, many scenarios have been proposed to explain the origin of magnetic fields in the IGM (see, e.g. Govoni and Feretti (2004) for a review).

The production of magnetic fields may be primordial. A mechanism for generation of primordial fields is related to the separation of charges between electrons and protons caused by the dynamo effect of Biermann (1950). Harrison (1970) suggested that this mechanism is possible because of swirling turbulence by which electric currents, and thus the magnetic field, can be generated. Other researchers have suggested that weak seed fields were formed during the quark-hadron phase transition (Quashnock et al., 1989), during the electro-weak phase transition (Baym et al., 1996) and mechanisms related to the physics of inflation (Turner and Widrow, 1988).

However it has been argued that the magnetic fields generated prior to recombination may not survive to the present age (Lesch and Birk, 1998; Battaner and Lesch, 2000). This leads to the hypothesis that magnetic fields are generated in later epochs of the Universe.

This scenario suggests that magnetic fields can be generated by normal or active galaxies (Kronberg, 1996; Rees, 1989), by AGNs (Rees and Setti, 1968; Daly and Loeb, 1990) or alternatively they might be generated during the events of merging between clusters (Dolag and Schindler, 2000; Roettiger et al., 1999). During these merging events, the rotation of clusters occurs when impact parameters are different from zero. This rotation of a cluster has not been observed, but it is believed that the energy associated with slow rotation is not sufficient to generate magnetic fields, and therefore strong merging events would be necessary (Carilli and Taylor, 2002).

To study the origin of magnetic fields by merging events several numerical simulations were carried out with an initial magnetic field value of $\sim 10^{-9}$G (Dolag and Schindler, 2000; Roettiger et al., 1999). These studies show that when a non-linear amplification in the shock from merging events combines with adiabatic compression, magnetic fields of order μG are produced in the ICM. These simulation studies have shown that the magnetic fields generated by these mechanisms are expected to have radial profiles that are similar to thermal gas (Dolag et al. (2001; 2002)).

2.4 Models for Radio Halo Origins

The presence of radio halos, observed in many galaxy clusters, implies that relativistic electrons and magnetic fields are present at a very large scale in these clusters, of the order of Mpc. Several models have been proposed to account for this phenomenon. Some of these models are discussed below, along with their advantages and disadvantages and their observational consequences.

2.4.1 Primary Electrons

As discussed in section 2.2.1 relativistic electrons can be produced in galaxy clusters by several mechanisms. In the primary electrons model these electrons directly produce the observed radio emission. Electrons can be accelerated in shocks (Tribble, 1993) according to the mechanism of Diffusive Shock Acceleration (Drury, 1983; Blandford and Eichler, 1987) or emitted by galaxies (Jaffe, 1977). Some well known problems with these theories include the short lifetime of electrons due to energy losses (see Fig. 2.1) and that electrons travel a shorter distance compared to the size of a radio halo (see Eq. 2.2). The primary electrons model implies that electrons remain very close to where they were accelerated and they produce radio emission for a very short time and this is not in accordance with the large size of the halos and their relative abundance (see Fig. 2.2).

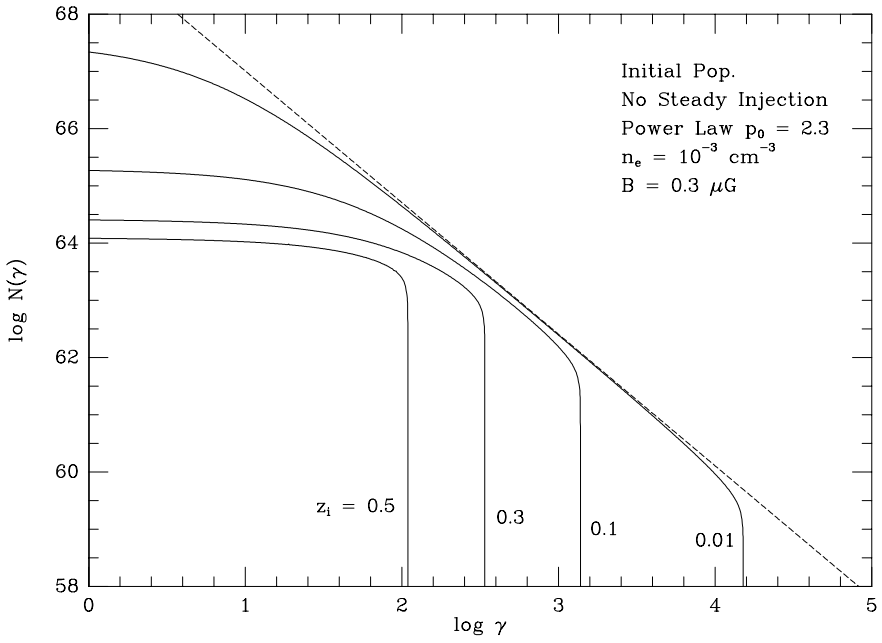

Figure 2.2: Evolution of spectrum of relativistic electrons from Sarazin (1999). The dashed line represents the initial population and the solid curves at redshift z_i : 0.001, 0.1, 0.3, and 0.5.

One hypothesis that has been proposed to mitigate these problems is that the shock produced by a merger can cross the cluster in a time less than the life of the particles, and in this way electrons can be accelerated on a large scale. It has been found that this would be

possible for a shock with a Mach number of the order of $M > 5$ (Brunetti, 2003). However, Miniati et al. (2001a) calculated the synchrotron radiation resulting from an event of this type, and found that the type of emission produced presents an irregular morphology that is similar to radio relics but not to radio halos.

Another problem with electrons accelerated in shocks is that this acceleration process has low efficiency because it imparts more energy to heating the thermal gas than to accelerating particles (Wolfe and Melia, 2006).

2.4.2 Re-accelerated Electrons

In this model, cosmic ray electrons are re-accelerated by magnetohydrodynamic (MHD) waves induced by turbulence produced in merging or accretion events. This is based on the assumption that there must exist a process that continuously provides energy to electrons in order to balance out the effects of the energy losses described above. That is to say if re-acceleration didn't occur frequently enough, the electrons at the centre of the cluster would lose their energy and would not be able to produce a radio halo. A two phase model was introduced by Brunetti et al. (2001) to account for an injection of relativistic electrons and the subsequent re-acceleration of these cosmic ray electrons.

It is important to note that this model is only efficient on a range of electron energies where the time scale of energy losses is greater than the time scale of re-acceleration. The loss and gain of energy is expressed as: $d\gamma/dt = \chi\gamma - (b_{synch} + b_{ICS})\gamma^2 - b_{Coul}$, where b_{synch} represents synchrotron losses, b_{ICS} represents losses due to Inverse Compton Scattering, b_{Coul} represents losses by Coulomb interactions, and χ is the efficiency of re-acceleration. Using this expression, we can obtain the range of energies (γ_1, γ_2) where acceleration is efficient: $\gamma_1 = b_{Coul}/\chi$ and $\gamma_2 = \chi/(b_{synch} + b_{ICS})$ (e.g. Brunetti et al.(2001)). Now imposing $\gamma_2 > \gamma_1$, we can show that the efficiency of re-acceleration must be $\chi^2 > b_{Coul}(b_{sunch} + b_{ICS})$. Considering typical values of losses in a galaxy cluster, i.e. $b_{Coul} \sim 10^{-15}\mathrm{s}^{-1}$ and $(b_{synch} + b_{ICS}) \sim 10^{-20}\mathrm{s}^{-1}$, the re-acceleration efficiency can be obtained as $(\chi \sim 10^{-17}\ \mathrm{s}^{-1})$ and hence the range of energies $\gamma \sim 10^2 - 10^3$. This is the range of energies of electrons that produce radio halos for magnetic field of order of μG, similar to the value found in galaxy clusters.

However, there are many problems with this model as the physical mechanisms that produce the re-acceleration are not known in detail leading to a large number of free parameters. Another problem is that the efficiency of this model scales with $(v_{wave}/c)^2 << 1$ which leads to inefficiency of second order Fermi acceleration. Also the acceleration efficiencies, i.e. the value of χ, are often tweaked to match with observations as the derivation of acceleration ef-

ficiency from first principles is complicated (Enßlin et al., 2011). Often the radial dependence of χ requires some adjustments to reproduce the observed power-law radio spectra seen in some radio halos. The magnetic field profiles are also fine tuned to fit the radio halo properties. However, as we can see in the figure, with this model it is not easy to reproduce the observed spectrum as it requires us to adjust some parameters. Moreover, the best fit holds only for a short range of time and does not really account for all the data (see Fig. 2.3).

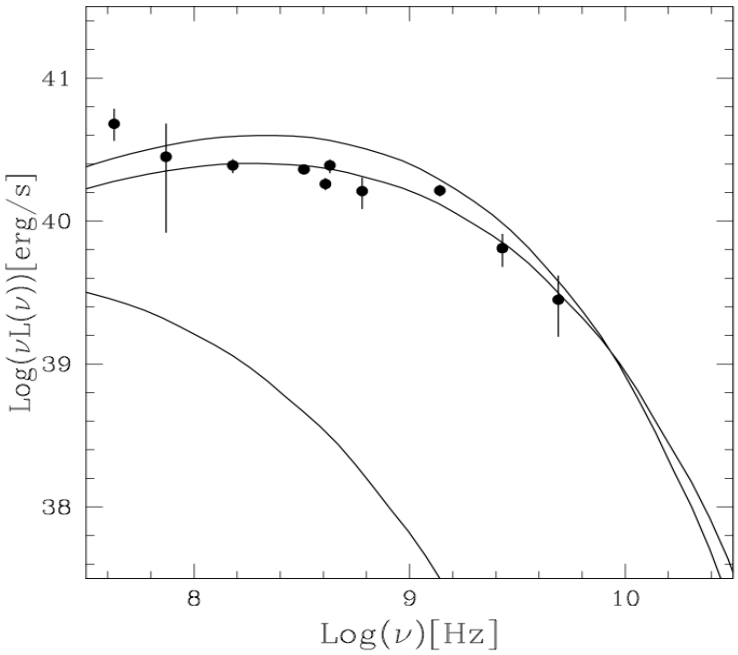

Figure 2.3: Predicted total synchrotron Coma radio spectrum compared with the flux measurements as a function of time. Plot from Brunetti et al. (2004). See this paper for details about the models used.

A consequence of the re-accelerated electron model is that gamma-ray emission is expected to be low because it is only produced by ICS and non-thermal Bremsstrahlung from relativistic electrons. The lack of gamma-ray detection could therefore be a point in favour of this theory (Ackermann et al. (2010; 2014)).

Another possibility to account for low efficiency is that the electrons that are re-accelerated are secondary electrons produced in hadronic collisions (see section 2.2.1, Brunetti et al. (2012)). In this case we have a similar problem to usual secondary models because the model predicts a strong production of gamma-rays (see section 2.4.3).

Another problem with this model is that it predicts intermittent re-acceleration of particles by turbulence and this is difficult to reconcile with the regular morphology of radio halos.

Due to insufficient information on the microphysics of the ICM, the scaling relations (L_ν - L_x) from this model are not immediate to derive. This model predicts a correlation between the synchrotron radio power (P_ν^{Synch}) and the total mass of the cluster inside a radius of 500 kpc (M_{500}) to be $\nu P_\nu^{Synch} \propto M_{500}^{4.0}$. However, this correlation is expected to have a high dispersion as a result of the number of free parameters present in this theory (Cassano et al., 2013).

2.4.3 Secondary Electrons by Hadronic Interactions

Another model for the production of secondary electrons is the well known hadronic collisions process ((Dennison, 1980; Blasi and Colafrancesco, 1999; Pfrommer and Enßlin, 2004; Marchegiani et al., 2007), see section 2.2.1). In this model, secondary electrons are continuously produced by interactions between protons in the thermal gas and non-thermal protons that are accumulated during the history of clusters. The advantage of this model is that the physical processes are well studied. The density of relativistic protons is expected to be relevant as some simulation studies predict that the energy content stored in non-thermal protons is of order 30% - 50% of the energy stored in thermal gas (Miniati et al., 2001b; Ryu et al., 2003). However, more recent simulation studies show that the energy content of non-thermal protons can be smaller than what was previously believed to be the case (Vazza et al., 2014).

Compared to the re-acceleration model, the hadronic model can be easily tested because it predicts a large quantity of gamma rays. In this respect there is a problem with this model due to the lack of detection of gamma-ray emission in galaxy clusters (Ackermann et al., 2010; Ackermann et al., 2014), and this implies that the amount of cosmic ray protons must be lower than previously calculated in simulations (Pinzke & Pfrommer (2010), see discussion in Vazza & Bruggen (2014)).

This model predicts a regular morphology as cosmic ray protons are expected to diffuse throughout the cluster. The volume and intensity of radio emission is proportional to the density of thermal gas (e.g. Miniati et al. (2001b)). Therefore this model is able to explain the morphology of regular radio halos but has some problems explaining radio halos with complex morphology.

The scaling relations predicted by this model show a strong correlation between L_ν and L_x, because the non-thermal electrons are correlated well with the thermal gas. The predicted scaling relation is given by: $\nu P_\nu^{Synch} \propto L_x^{1.58-1.46}$ (Cassano et al., 2013). Due to the strong scaling relation predicted by this model it is difficult to account for the presence of a cluster

with high observed x-ray luminosity and no radio halos (see discussion in Enßlin et al.(2011)).

Another possible problem with this model is that some properties of clusters, such as steepening at high frequencies of the radio halo spectrum (Thierbach et al.(2003), in the case of Coma) and the radial change of the spectral index (Giovannini et al.(1999), in the case of Coma) are difficult to explain (see Fig. 2.4 and see discussion in Enßlin et al.(2011)).

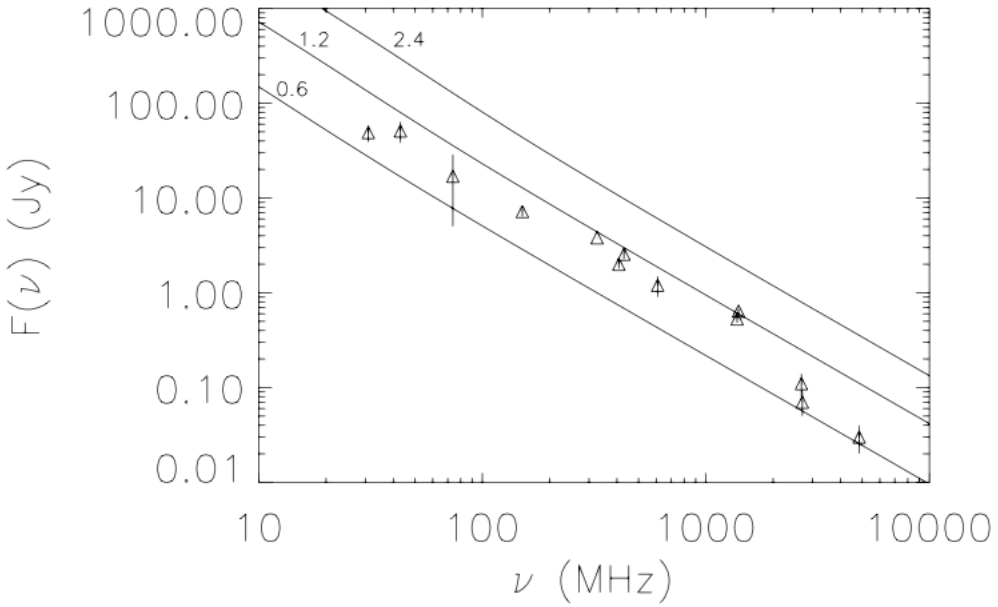

Figure 2.4: Coma radio halo spectrum for three different values of magnetic field strength from Marchegiani et al. (2007).

2.4.4 Secondary Electrons by Dark Matter Annihilations

As we saw in section 1.2.3, most of the mass in a galaxy cluster is expected to be in the form of dark matter. Some models of dark matter predict a large quantity of electrons, positrons and gamma-rays generated during the annihilation of dark matter particles. One of the most studied possibilities for the particles constituting dark matter is neutralinos, the lightest stable particle in the minimal super-symmetric extension of the standard model (e.g. Bertone et al. (2005)). The astrophysical consequences of this assumption have been explored by several authors (e.g. Colafrancesco & Mele (2001), Colafrancesco et al. (2006), Pérez-Torres et al.(2009) and others).

One of the advantages of this model is that it is able to explain the steepening of the radio halo spectrum at higher frequencies (Thierbach et al. (2003), see Fig. 1.15), because in

this model the spectrum of secondary electrons steepens when the energy of the electrons is similar to the mass of neutralinos, see Fig. 2.5, (Colafrancesco et al., 2011a). However the nature of dark matter, its composition and mass, the value of annihilation cross section and the presence of sub-structures in the spatial distribution are not well known and this makes it difficult to constrain all these properties from observations (e.g. Colafrancesco et al. (2015a)).

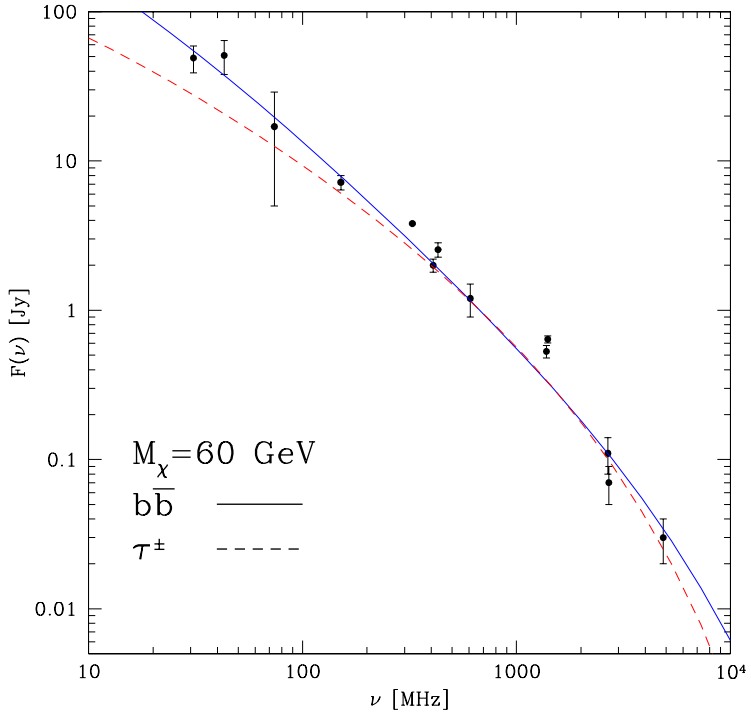

Figure 2.5: The radio halo spectrum of Coma and the best fits of DM model (Colafrancesco et al., 2011a).

This model also predicts a strong gamma-ray emission and due to the lack of detection of these gamma-rays it faces a similar problem to that encountered by the hadronic model (S. Zimmer for the Fermi-LAT Collaboration, 2015).

Observations have confirmed that certain clusters exhibit radio halos whilst others of similar mass do not. Therefore the mass of a cluster alone is not sufficient to determine whether a cluster will have a radio halo or not. It is difficult to reconcile this fact with the predictions of the dark matter annihilation model, in which radio emission is strongly correlated with the mass of the dark matter halo (Colafrancesco et al., 2015a).

As there are no expected interactions between dark matter particles and baryonic particles, this model predicts a reasonably regular morphology of radio halos excluding the irregular

morphology produced by sub-structures in the dark matter halo (Colafrancesco et al., 2015b).

2.4.5 UHE$\gamma + \gamma$ interactions

Another possibility for the production of secondary cosmic ray electrons was considered by Timokhin et al. (2004). In this model, secondary relativistic electrons are produced by ultra high energy gamma rays interacting with diffuse extragalactic radiation fields. However, they found that the synchrotron emission can be detected in HXR and not in the radio band (for more details see, e.g. Fig.2 in Timokhin et al. (2004)).

2.5 Problems with the Current Models

From the discussion in the previous section we can conclude that the origin of radio halos is still not clear. None of the proposed models can fully explain observations at this stage. The secondary hadronic model is founded on well known physics and provides a natural explanation for the presence of radio halos in galaxy clusters but this model predicts a large amount of gamma-rays that are not detected. The same problem is present in the case of secondary electrons produced by dark matter annihilation, in addition to which the physics of dark matter is not well known. For this reason the usually preferred model for the origin of radio halos is the re-acceleration model, which also explains the steepening of the radio halo spectrum at high energies observed in some clusters, for example in Coma. However this model is based on physics that is not well known and the processes that are assumed are not very efficient (e.g. Wolfe & Melia (2006)).

A common property of all these models is that they predict a strong correlation between the radio and thermal properties of clusters. In the case of the secondary hadronic model this is obvious because the intensity of the radio emission is proportional to the density of thermal gas as described in the previous section. A very strong correlation between mass and radio luminosity is predicted by the secondary dark matter model, and since the mass is related to the X-ray luminosity, a strong correlation is expected between the radio and the X-ray luminosities. The re-acceleration model is based on turbulence produced by shock that leads to the acceleration of relativistic electrons but also to the heating of thermal gas (Colafrancesco and Marchegiani, 2008) and the acceleration of relativistic protons (Brunetti et al., 2004). These relativistic protons produce secondary electrons and gamma-rays and heat the thermal gas. As a consequence there are two ways in which the thermal gas can be heated and this fact on one hand puts a limit on the amount of energy produced by this

mechanism and on the other hand predicts a strong correlation between radio and X-ray luminosities.

However, observations show that this correlation in some cases is not very strong. For example, looking at the comparison of radio and X-ray maps, we note that in some cases the peak of a radio emission is not located at the same place as the peak of an x-ray emission and appears to be located where there is a high concentration of galaxies, like in the cases of A800 (see Fig. 2.6), A1550 (Govoni et al., 2012) and other systems. Some other evidence is observed in complex clusters. One example is the Bullet cluster (Liang et al.(2000), Shimwell et al.(2014; 2015)), which exhibits more than one peak in its radio halo distribution where two of them are in the same position as that of the X-ray emission whereas the other is related to the concentration of galaxies (see Fig. 2.7 and Fig. 2.8). Another example is MACS J0717.5+3745, a cluster with four different concentrations of galaxies of which at least three correspond to observed peaks in radio emission (van Weeren et al., 2009; Bonafede et al., 2009; Pandey-Pommier et al., 2013). These last two clusters are good examples as the position of the radio halo peak is different to that of the X-ray peak. Other observations reveal that some clusters have peaks approximately at the same position in X-ray and Radio emission but their emissions show different orientations (see for example, the case of CL1446+26, Govoni et al. 2012).

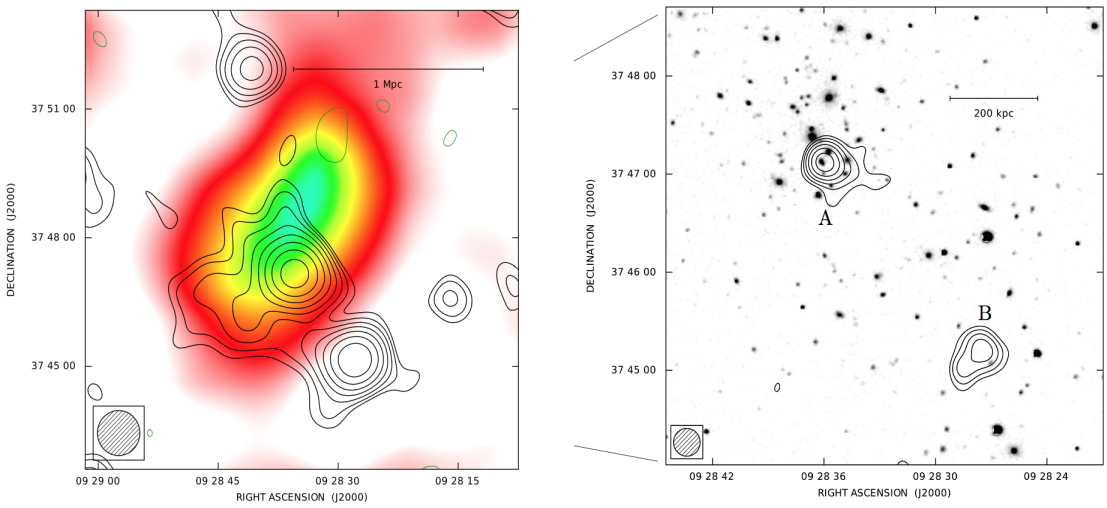

Figure 2.6: An example of a cluster, A800 from Govoni et al. (2012), where the radio halo is not located at the same place as the peak of the X-ray map (see figure on the left) and appears to be located where there is a high concentration of galaxies (see figure on the right). Also note that the orientations of the radio and X-ray maps are different.

A point-to-point comparison of radio and X-ray emissions was carried out by Govoni et al. (Govoni et al., 2001a) for a small sample of four clusters. It was found that in some

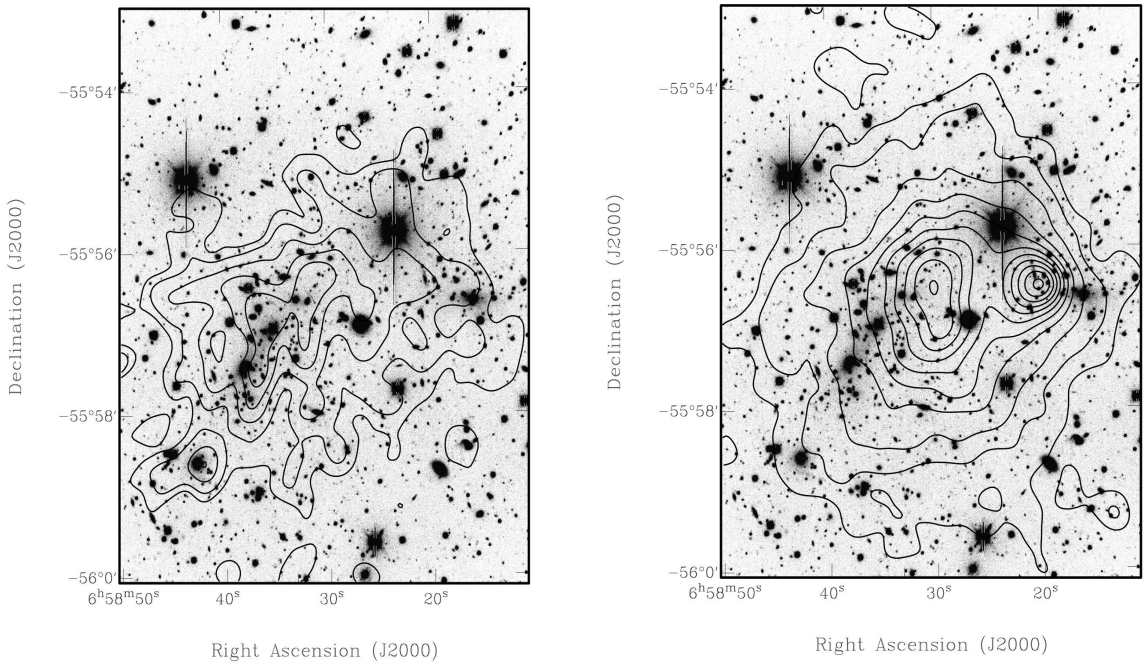

Figure 2.7: An example of a cluster, the Bullet cluster from Liang et al. (2000), in which the radio emission appears to be located where there is a high concentration of galaxies (see figure on the left) but the X-ray emission is displaced from the main concentration of galaxies (see figure on the right).

clusters such as Coma (see Fig. 2.9 on left) there is some correlation between the Radio-Xray surface brightness but with a large variation in radio values for a given X-ray value. It was also found that in other clusters such as A2319 (see Fig. 2.9 on right) there is a large scatter in X-ray values for a given radio value. From this study we can conclude that there is some correlation between the X-ray and radio surface brightness but it is not a strong correlation.

One of the fundamental assumptions of the current models is that the presence of radio halos is associated with merging clusters. However, some observations reveal the presence of a radio halo but no clear merging, for example the case of Coma where there is a large radio halo but it is not clear if there is a strong merging or an accretion shock produced by a small group of galaxies interacting (Ogrean and Brüggen, 2013). Also in the case of Ophiucus there is a diffuse emission usually classified as a mini halo but with a radius $\sim$ 500 kpc (Murgia et al., 2010) where the presence of merging is controversial (Fujita et al., 2008; Watanabe et al., 2001). Additionally, some merging clusters show no radio emission (e.g. A2146, Russell et al. (2011) and A119, Giovannini and Feretti(2000)). In some cases there is also not a strong coincidence between relics and shocks (see Ogrean et al. (2013; 2014), for the case of 1RXS J0603.3+4214 (Toothbrush cluster) and ZwCl 2341.1+0000) and as a

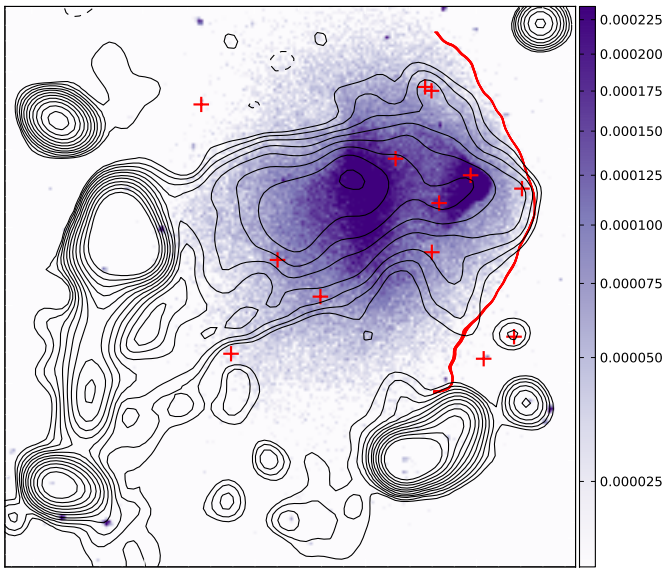

Figure 2.8: ATCA radio contours of the Bullet cluster overlaid on a X-ray colour image from Chandra, the red line represents the X-ray shock front (Shimwell et al., 2014).

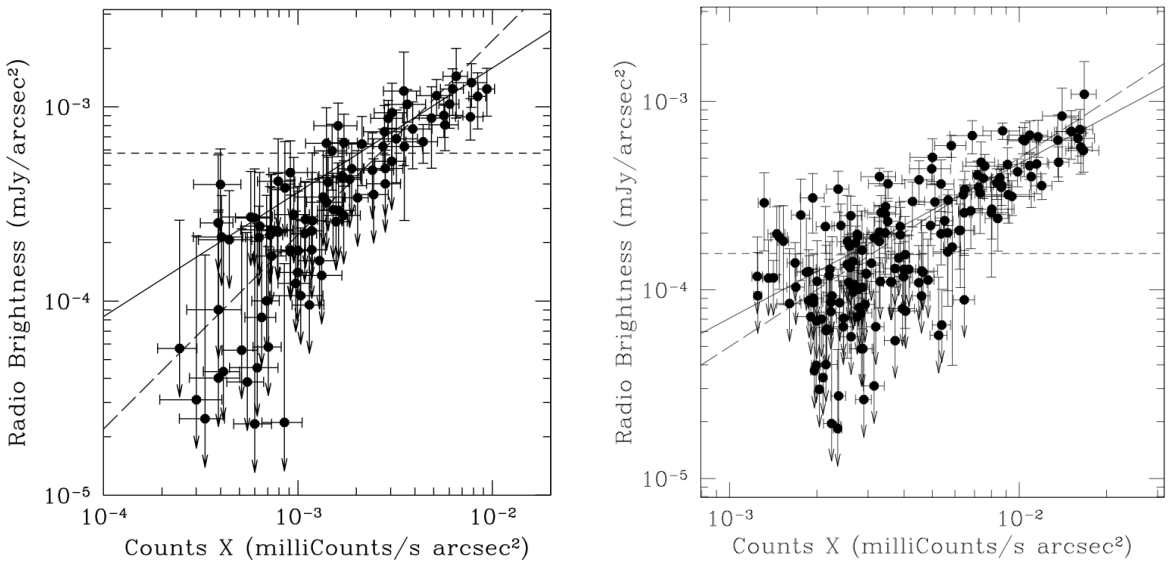

Figure 2.9: Radio and X-ray surface brightness point-to-point correlation for Coma (Left) and A2319 (Right). The correlation in these two clusters is not very strong as both the plots show some variation in Radio and X-ray points - especially in the lower surface brightness region. (Govoni et al., 2001a)

consequence it is possible that they do not have the same origin.

One of the predictions of these models is a reasonably strong correlation between radio and X-ray luminosities. While this correlation is good for a number of clusters with some

scatter, there are clusters which exhibit no radio halos at high X-ray luminosity (see Fig. 1.14) and other clusters with low X-ray luminosity showing a luminous radio halo (see Fig. 2.10), in the case of A523 (Giovannini et al., 2011), A1213 (Giovannini et al., 2009) and 0217+70 (Brown et al., 2011).

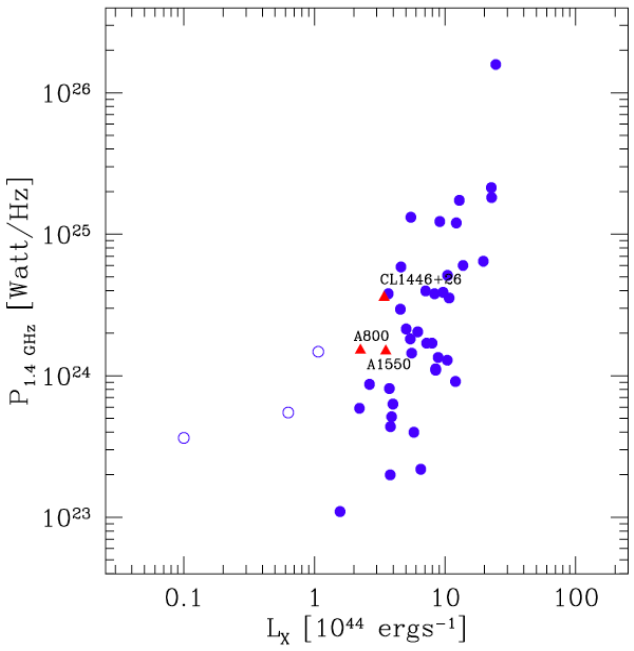

Figure 2.10: Radio power of radio halos at 1.4 GHz versus the cluster X-ray luminosity. From this plot it is clear that there is a correlation but with some scatter that is increasing at low L_x and $P_{1.4}$. The empty blue circles represent radio halos that are over-luminous in radio with respect to the cluster X-ray luminosity. Figure from Govoni et al. (2012)

For all these reasons we think that the origin of radio halos, at least in some cases, is not well accounted for by the present models. Hence there is a need for a new framework in order to explain the origin and evolution of radio halos in galaxy clusters. In the next section a new idea for these phenomena is presented.

2.6 A New Idea

In the light of the problems presented above, it is clear that the current models are not sufficient to account for all observations. Therefore we want to propose a new idea with the aim to better explain the origin and structure of radio halos. Motivated by the observations discussed in the previous section, where certain radio halos seem to correlate better with the concentration of galaxies than they do with the thermal gas, we propose a model to explore

the possibility that radio halos are originated by a combination of individual halos in the cluster galaxies.

In our proposed model we consider that electrons are produced in galaxies by the different mechanisms described in section 2.2.1 and diffuse in the ICM subject to diffusion in magnetised plasma and losses of energies (see section 2.2.2). Our model describes both the spatial and spectral properties of the electron distribution from each galaxy. It also allows us to express the time interval over which a galaxy is injecting electrons. In this way we can study both the present shape of radio maps and their evolution.

As a consequence of our new model we expect that there is not a strong correlation between the thermal gas and the radio halo in a low-L_x cluster because the electrons are injected directly from the member galaxies, and therefore they are related mainly to the physics of galaxies and not of the intra cluster medium. However, some correlation is expected between the radio and X-ray luminosity because we expect that rich clusters (luminous in X-ray) that contain many galaxies produce a large number of electrons hence a brighter radio halo. Radio halos in rich clusters are expected to have a regular morphology due to the high number of galaxies that can be distributed in a more uniform way.

In the past a similar model was proposed by Jaffe (1977) involving electrons injected by galaxies. However, Jaffe's model studied a steady state solution where the effect of diffusion was considered only by calculating the maximum distance that particles can diffuse under simplified assumptions like galaxies being point sources of electrons and the diffusion coefficient being a linear function of energy. Also, this model assumed that radio halos are formed by emission from radio galaxies only without considering that non-radio galaxies can contribute to the production of radio halos by smaller effects like galactic winds. It also did not consider that different galaxies can inject electrons at different times. For these reasons, Jaffe couldn't study the spatial and temporal properties of radio halos and was only able to calculate their spectral properties and integrated luminosities.

In order to describe our model, we first study (Chapter 3) the diffusion equation that describes the evolution of relativistic particles and solve this equation in a very general way regarding the spectral, spatial and time properties. Later in chapter 4 we apply this model to the radio halo of the galaxy M51 in order to reproduce its spectral and spatial properties. This enables us to fit the model parameters, and leads to an investigation of whether this model can reproduce a radio halo in a single radio galaxy. This model is then used to study radio halos in clusters via a combination of several contributions from different galaxies by changing their properties, number and positions, and we compare results with some observed

radio halos (Chapter 5). Finally in Chapter 6 we discuss the results of the model, ways of testing it, possible future applications and improvements and present our conclusion.

Chapter 3

Solutions of the Diffusion Equation

"In questions of science, the authority of a thousand is not worth the humble reasoning of a single individual."

-Galileo Galilei

"Subjectivism is not an absolute principle; it is a necessary but not sufficient condition for sound methodology."

-Murray Rothband

3.1 Introduction

As discussed in the previous chapter, the study of the diffusion of cosmic rays in galaxies and clusters of galaxies is crucial to model the structure and evolution of radio halos. Here we present a general model for the diffusion of these relativistic particles that takes a source term as input and produces the density of these particles as output. Density profiles of these particles can be used to study the integrated flux and surface brightness distribution of halos in galaxies and clusters. The diffusion of cosmic rays is described by a transport equation and the general analytical solution for electrons is presented in this section for an arbitrary source $Q(\mathbf{r}, \gamma, t)$, where $\mathbf{r}$ is the volume element, γ is the Lorentz factor of particle and t is time. Furthermore, numerical methods are developed to obtain the final density profiles for a time dependent source. The solutions are then compared with the existing steady state solutions.

3.2 General Method: Analytical Solution

Diffusion of relativistic electrons is described by a transport equation, which takes into account the presence of the source and the continuous loss/gain in energy during the diffusion process

(Syrovat-skii, 1959) derived from Eq.(2.1) for $D(\gamma)$ independent of radius:

$$\frac{\partial f(\mathbf{r},\gamma,t)}{\partial t} - D(\gamma)\Delta f(\mathbf{r},\gamma,t) + \frac{\partial}{\partial\gamma}[b(\gamma)f(\mathbf{r},\gamma,t)] + \frac{f(\mathbf{r},\gamma,t)}{T} = Q(\mathbf{r},\gamma,t). \tag{3.1}$$

Here, $f(\mathbf{r},\gamma,t)$ describes the spatial and energy distribution of a particle at a given time (i.e. the density of particles with energy γ at a distance r from the source at a given time t) and Δ is the Laplace operator. Scattering of particles from a source is described by $D(\gamma)$, an energy dependent diffusion coefficient. $b(\gamma) = \frac{d\gamma}{dt}$ is the rate of change of energy resulting from losses/gains in energy during the diffusion process. T is the average lifetime of particles, i.e. the time in which the energy of particles decreases, and $Q(\mathbf{r},\gamma,t)$ is the rate at which particles are produced(i.e. the source term). Following Syrovat-skii (1959), the general solution of this equation for an arbitrary source distribution is obtained using a Green's function, which is derived by solving the simplified equation:

$$\frac{\partial f_G}{\partial t} - D\Delta f_G + \frac{\partial}{\partial\gamma}(bf_G) + \frac{f_G}{T} = \delta(\mathbf{r}-\mathbf{r_0})\delta(\gamma-\gamma_0)\delta(t-t_0) \tag{3.2}$$

and is given by

$$f_G(\mathbf{r},\gamma,t;\mathbf{r}_0,\gamma_0,t_0) = \frac{e^{-\tau/T}}{|b(\gamma)|(4\pi\lambda)^{3/2}} Exp\left[-\frac{(\mathbf{r}-\mathbf{r}_0)^2}{4\lambda}\right]\delta(t-t_0-\tau), \tag{3.3}$$

where

$$\tau(\gamma_0,\gamma) = \int_{\gamma_0}^{\gamma}\frac{1}{b(\gamma')}d\gamma', \tag{3.4}$$

is the time required for electrons to escape from the source and

$$\lambda(\gamma_0,\gamma) = \int_{\gamma_0}^{\gamma}\frac{D(\gamma')}{b(\gamma')}d\gamma' \tag{3.5}$$

is related to the average path length of an electron.

The analytical solution of (3.1) for an arbitrary source distribution is then obtained using the above Green's function:

$$f(\mathbf{r},\gamma,t) = \iiint_{-\infty}^{+\infty} d\mathbf{r}_0 \int_1^{\infty} d\gamma_0 \int_{-\infty}^{t} dt_0 \quad Q(\mathbf{r_0},\gamma_0,t_0) f_G(\mathbf{r},\gamma,t;\mathbf{r_0},\gamma_0,t_0) \tag{3.6}$$

where $d\mathbf{r}_0$ is an element of volume.

3.3 Assumptions and Definitions

In order to find solutions of Eq.(3.1) we have to make some assumptions and definitions, each of which is described briefly below.

- We assume that the source function is variable separable:

$$Q(\mathbf{r_0}, \gamma_0, t_0) = Q_r(\mathbf{r_0}) Q_\gamma(\gamma_0) Q_t(t_0)$$

- We consider the production of relativistic particles in any source, such as galaxies and AGNs (see section 2.2.1). We can expect that the rate of relativistic electron production is greater at the centre of the source than away from it. This system can be described mathematically by a 3D Gaussian with axes x_s, y_s and z_s. This description is good for various sources as we are able to vary the size of the gaussian by varying x_s, y_s and z_s, for example setting $x_s = y_s = z_s$ we get a spherically symmetrical system and if $z_s = 0$ with $x_s = y_s$ we get a flat system (Syrovat-skii, 1959). In general, the energy distribution spectrum is taken as a power law and all the normalisation of the source is absorbed by the constant Q_0 in $Q_\gamma(\gamma_0)$. The time distribution is assumed to be a step function, with t_1 being the time at which electron production begins and t_2 being the time at which electron production ends:

$$Q_r(\mathbf{r_0}) = \exp\left(-\frac{x_0^2}{x_s^2} - \frac{y_0^2}{y_s^2} - \frac{z_0^2}{z_s^2}\right) \tag{3.7}$$

$$Q_\gamma(\gamma_0) = Q_0\, \gamma_0^{-\rho} \qquad \gamma_{min} < \gamma_0 < \gamma_{\max} \tag{3.8}$$

$$Q_t(t_0) = \theta(t_0 - t_1)\theta(t_2 - t_0) \tag{3.9}$$

- We assume an average magnetic field uniformly distributed over the source and we define the diffusion coefficient $D(\gamma)$ to be independent of r but dependent on energy. The energy dependence in $D(\gamma)$ is a result of the scattering of particles from magnetic field irregularities with the assumption of the Kolmogorov spectrum (see Eq.(1.15)).

$$D(\gamma) = d_0 \gamma^{1/3} \beta_\mu^{-1/3} \tag{3.10}$$

  [e.g. (Blasi and Colafrancesco, 1999; Berezinsky et al., 1997; Colafrancesco and Blasi, 1998)], where β_μ is the average magnetic field in μG units, and d_0 is a constant depicting minimum scale magnetic field fluctuations.

- The function $b(\gamma)$ for electrons, a sum of effects due to Inverse Compton, Synchrotron

radiation, Coulomb losses and Bremsstrahlung is defined as:

$$b(\gamma) = -\{1.3 \times 10^{-21}\beta_\mu^2\gamma^2 + 1.37 \times 10^{-20}\gamma^2 + 1.5 \times 10^{-16}\gamma\, n_{th}(\log(\gamma) + 0.36) + 1.2 \times 10^{-12} n_{th}\left(\frac{1}{75}\log\left(\frac{\gamma}{n_{th}}\right) + 1\right)\} \quad s^{-1} \tag{3.11}$$

[e.g. Sarazin(1999)], where n_{th} is the mean number density of thermal electrons in cm^{-3}. The values of these loss functions as functions of γ are given in Fig. 3.1 for $n_{th} = 1 \times 10^{-3}\mathrm{cm}^{-3}$ and average intra cluster medium magnetic field of $\beta_\mu = 1$ and $15\,\mu$G. Looking at the figure and the expressions for the loss functions it is clear that IC and Synchrotron losses are dominant at large energies, $\gamma \geq 200$, while at lower energies, $\gamma \leq 200$, the losses are dominated by the Coulomb term. The effects of Bremsstrahlung losses at low energy are always less than Coulomb losses and at high energy Synchrotron losses are comparable with IC losses with magnetic field of order $3.2\,\mu$G.

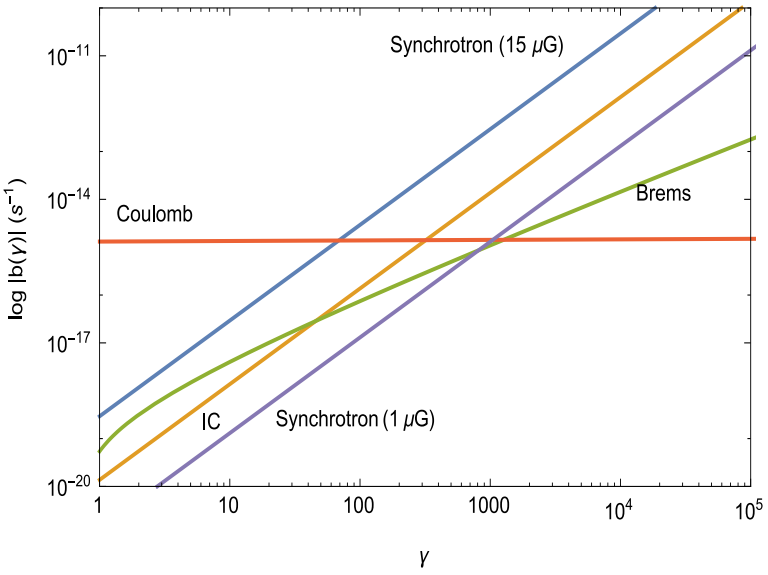

Figure 3.1: Values of the total loss function $b(\gamma)$ for Synchrotron losses, inverse Compton (IC) emission, Bremsstrahlung losses, and Coulomb losses as functions of γ, with $n_{th} = 10^{-3}$ cm^{-3} and $\beta_\mu = 1\,\mu$G, where the IC losses are dominant, and $\beta_\mu = 15\,\mu$G, where Synchrotron losses are dominant.

3.4 Steady State Solution

In the case of the particle source being independent of time, $Q_t(t_0) \equiv 1$ (corresponding to $t_1 \to -\infty$ and $t_2 \to +\infty$), the Eq.(3.3) can be integrated over time to obtain the number density of particles, which is independent of time:

$$\begin{aligned} f_G(\mathbf{r},\gamma,\mathbf{r_0},\gamma_0) &= \int_{-\infty}^{t} dt_0 \quad f_G(\mathbf{r},\gamma,t;\mathbf{r_0},\gamma_0,t_0) \\ &= \frac{1}{|b(\gamma)|(4\pi\lambda)^{3/2}} \exp\left(-\frac{(\mathbf{r}-\mathbf{r_0})^2}{4\lambda}\right) \exp\left(-\frac{\tau}{T}\right) \theta(\tau). \end{aligned} \tag{3.12}$$

The stationary solution is then obtained as follows:

$$f(\mathbf{r},\gamma) = \iiint_{-\infty}^{+\infty} d\mathbf{r}_0 \int_1^{\gamma_{Max}} d\gamma_0 \quad f_G(\mathbf{r},\gamma;\mathbf{r_0},\gamma_0) Q(\mathbf{r}_0,\gamma_0)\theta(\tau). \tag{3.13}$$

Here, the integral over $\mathbf{r_0}$ is calculated analytically:

$$\begin{aligned} f(\mathbf{r},\gamma) &= \iiint_{-\infty}^{+\infty} d\mathbf{r}_0 \int_1^{\gamma_{Max}} d\gamma_0 \quad \frac{Q_0\,\gamma_0^{-\rho}}{|b(\gamma)|(4\pi\lambda)^{3/2}} \exp\left(-\frac{(\mathbf{r}-\mathbf{r_0})^2}{4\lambda} - \frac{\tau}{T}\right) \\ &\quad \times \exp\left(-\frac{x_0^2}{x_s^2} - \frac{y_0^2}{y_s^2} - \frac{z_0^2}{z_s^2}\right) \theta(\tau) \\ &= \int_1^{\gamma_{\max}} d\gamma_0 \quad \frac{x_s y_s z_s Q_0}{|b(\gamma)|} \frac{\gamma_0^{-\rho}}{(x_s^2+4\lambda)^{1/2}(y_s^2+4\lambda)^{1/2}(z_s^2+4\lambda)^{1/2}} \\ &\quad \times \exp\left(-\frac{x^2}{x_s^2+4\lambda} - \frac{y^2}{y_s^2+4\lambda} - \frac{z^2}{z_s^2+4\lambda} - \frac{\tau}{T}\right) \theta(\tau). \end{aligned} \tag{3.14}$$

Assuming spherical symmetry we now set $x_s = y_s = z_s \equiv r_s$, and letting $r^2 = x^2 + y^2 + z^2$, the above integral is written as:

$$\begin{aligned} f(r,\gamma) &= \int_1^{\gamma_{Max}} d\gamma_0 \quad \frac{r_s^3 Q_0}{|b(\gamma)|} \frac{\gamma_0^{-\rho}}{(r_s^2+4\lambda)^{3/2}} \exp\left(-\frac{r^2}{r_s^2+4\lambda} - \frac{\tau}{T}\right) \theta(\tau) \\ &= \int_\gamma^{\gamma_{Max}} d\gamma_0 \quad \frac{r_s^3 Q_0}{|b(\gamma)|} \frac{\gamma_0^{-\rho}}{(r_s^2+4\lambda)^{3/2}} \exp\left(-\frac{r^2}{r_s^2+4\lambda} - \frac{\tau}{T}\right). \end{aligned} \tag{3.15}$$

The integration limits are due to the condition $\tau > 0$, which is only possible if $\gamma_0 > \gamma$, as only energy losses are considered, i.e. $b < 0$ in Eq.(3.4).

3.5 Time-dependent Solution

3.5.1 Analytical Solution

Before a numerical time dependent solution is obtained, the integrals over t_0 and $\mathbf{r_0}$ are solved analytically. Spherical symmetry in $\mathbf{r}$ is assumed once the integral over $\mathbf{r_0}$ has been carried out.

The integral over time t_0 is solved as:

$$f_G(\mathbf{r},\gamma,t,\mathbf{r_0},\gamma_0) = \int_{-\infty}^{t} dt_0 \quad f_G(\mathbf{r},\gamma,t;\mathbf{r_0},\gamma_0,t_0)\theta(t_0-t_1)\theta(t_2-t_0)$$

$$= \frac{1}{|b(\gamma)|(4\pi\lambda)^{3/2}}\exp\left(-\frac{(\mathbf{r}-\mathbf{r_0})^2}{4\lambda}\right)\exp\left(-\frac{\tau}{T}\right)$$

$$\times\,\theta(\tau)\theta(t-t_1-\tau)\theta(-t+t_2+\tau). \tag{3.16}$$

The integral over $\mathbf{r_0}$ is solved as:

$$f(\mathbf{r},\gamma,t) = \iiint_{-\infty}^{+\infty} d\mathbf{r}_0 \int_1^{\gamma_{Max}} d\gamma_0 \quad \frac{Q_0\,\gamma_0^{-\rho}}{|b(\gamma)|(4\pi\lambda)^{3/2}}\exp\left(-\frac{(\mathbf{r}-\mathbf{r_0})^2}{4\lambda}-\frac{\tau}{T}\right)$$

$$\times\exp\left(-\frac{x_0^2}{x_s^2}-\frac{y_0^2}{y_s^2}-\frac{z_0^2}{z_s^2}\right)\theta(\tau)\theta(t-t_1-\tau)\theta(-t+t_2+\tau)$$

$$= \int_1^{\gamma_{\max}} d\gamma_0 \quad \frac{x_s y_s z_s Q_0}{|b(\gamma)|}\frac{\gamma_0^{-\rho}}{(x_s^2+4\lambda)^{1/2}(y_s^2+4\lambda)^{1/2}(z_s^2+4\lambda)^{1/2}}\,\exp\left(-\frac{\tau}{T}\right) \tag{3.17}$$

$$\times\exp\left(-\frac{x^2}{x_s^2+4\lambda}-\frac{y^2}{y_s^2+4\lambda}-\frac{z^2}{z_s^2+4\lambda}\right)$$

$$\times\,\theta(\tau)\theta(t-t_1-\tau)\theta(-t+t_2+\tau).$$

Now assuming spherical symmetry, i.e. $x_s = y_s = z_s \equiv r_s$, and letting $r^2 = x^2 + y^2 + z^2$, the above integral is written as:

$$f(r,\gamma,t) = \int_1^{\gamma_{Max}} d\gamma_0 \quad \frac{r_s^3\, Q_0}{|b(\gamma)|} \frac{\gamma_0^{-\rho}}{(r_s^2+4\lambda)^{3/2}} \exp\left(-\frac{r^2}{r_s^2+4\lambda} - \frac{\tau}{T}\right)$$

$$\times\, \theta(\tau)\theta(t-t_1-\tau)\theta(-t+t_2+\tau). \tag{3.18}$$

3.5.2 Numerical Solution

The integral in Eq.(3.18) is of the form:

$$\int_1^{\gamma_{Max}} d\gamma_0 \quad f(r,\gamma,\gamma_0,t)\theta(\tau)\theta(t-t_1-\tau)\theta(-t+t_2+\tau). \tag{3.19}$$

It is necessary to find the support[1] of the integrand in order to facilitate efficient numerical integration. A large part of this determination is finding the support of the three Heaviside Theta functions above. We now proceed to find the values of γ_0 for which each of these functions is nonzero.

Theta function $\theta(\tau)$

$\theta(\tau)$ is nonzero whenever $\tau > 0$ (see Eq.(3.4)), in which case $\theta(\tau)$ is 1. It is important at this point to understand that as we are modelling energy losses, $b(\gamma)$ is always negative (See Eq.(3.11)). Thus τ is a strictly monotone increasing function of γ_0 (assuming γ to be fixed, see Fig.3.2).[2]

It is clear from Fig.3.2, that $\tau = 0$ when $\gamma_0 = \gamma$ and $\tau > 0$ whenever $\gamma_0 > \gamma$.

Therefore:

$$\theta(\tau(\gamma_0)) = \begin{cases} 0 & \text{if } \gamma_0 \le \gamma \\ 1 & \text{if } \gamma_0 > \gamma. \end{cases}$$

[1] The support of a function is the subset of its domain on which it is nonzero. $supportf := \{x \in domf : f(x) \neq 0\}$

[2] $\frac{d\tau}{d\gamma_0} = -\frac{1}{b(\gamma_0)} > 0$ by fundamental theorem of calculus.

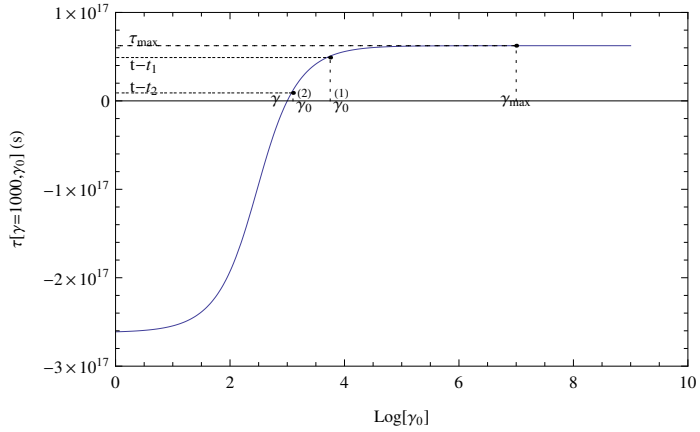

Figure 3.2: τ a strictly monotone increasing function of γ_0 at a fixed value of $\gamma = 1000$.

Hence, $\theta(\tau) = \theta(\gamma_0 - \gamma)$ and,

$$\int_1^{\gamma_{Max}} d\gamma_0 \quad f(r, \gamma.\gamma_0, t)\theta(\tau)\theta(t - t_1 - \tau)\theta(-t + t_2 + \tau)$$

$$= \int_\gamma^{\gamma_{Max}} d\gamma_0 \quad f(r, \gamma.\gamma_0, t)\theta(t - t_1 - \tau)\theta(-t + t_2 + \tau). \tag{3.20}$$

Theta function: $\theta(t - t_1 - \tau)$

We have already demonstrated that τ is a strictly monotone increasing function of γ_0 and therefore also an invertible function. Since it is invertible we can solve for γ_0 such that,

$$\tau(\gamma_0^{(1)}) = t - t_1. \tag{3.21}$$

Then it is clear that

$$\tau < t - t_1 \iff \gamma_0 < \gamma_0^{(1)}$$

and so:

$$\theta(t - t_1 - \tau) = \theta(\gamma_0^{(1)} - \gamma_0) = \begin{cases} 0 & \text{if } \gamma_0 \geq \gamma_0^{(1)} \\ 1 & \text{if } \gamma_0 < \gamma_0^{(1)}. \end{cases}$$

Theta function: $\theta(\tau - t + t_2)$

Here, let $\gamma_0^{(2)}$ be the solution of

$$\tau(\gamma_0^{(2)}) = t - t_2 \tag{3.22}$$

then clearly,

$$\tau > t - t_2 \iff \gamma_0 > \gamma_0^{(2)},$$

and so:

$$\theta(\tau - t + t_2) = \theta(\gamma_0 - \gamma_0^{(2)}) = \begin{cases} 0 & \text{if } \gamma_0 \leq \gamma_0^{(2)} \\ 1 & \text{if } \gamma_0 > \gamma_0^{(2)}. \end{cases}$$

Resulting Theta functions

Putting this all together, the remaining theta functions are:

$$\theta(\gamma_0^{(1)} - \gamma_0)\theta(\gamma_0 - \gamma_0^{(2)}) = \begin{cases} 1 & \text{if } \gamma_0^{(2)} < \gamma_0 < \gamma_0^{(1)} \\ 0 & \text{otherwise.} \end{cases}$$

The support of the three theta functions is thus:

$$[\gamma, \gamma_{\max}] \cap [\gamma_0^{(2)}, \gamma_0^{(1)}] = [\max(\gamma, \gamma_0^{(2)}), \min(\gamma_{\max}, \gamma_0^{(1)})].$$

Hence the integral in Eq.(3.18) can now be written as:

$$f(r, \gamma, t) = \int_{\max(\gamma, \gamma_0^{(2)})}^{\min(\gamma_{\max}, \gamma_0^{(1)})} d\gamma_0 \quad \frac{r_s^3 Q_0}{|b(\gamma)|} \frac{\gamma_0^{-\rho}}{(r_s^2 + 4\lambda)^{3/2}} \exp\left(-\frac{r^2}{r_s^2 + 4\lambda} - \frac{\tau}{T}\right). \tag{3.23}$$

Note that the time dependence in the integral Eq.(3.23) only comes from the integration limits, i.e. the integrand is independent of time. This means that the function will not change with time whenever the integral is performed over the entire interval from γ to $\gamma_{\max}$. That is to say that whenever $\gamma_0^{(1)} > \gamma_{\max}$ and $\gamma_0^{(2)} < \gamma$ the function is in a steady condition (see Eq.(3.15)). Refer to the Fig. 3.2 and Fig. 3.3, notice that these conditions on $\gamma_0^{(1)}$ and $\gamma_0^{(2)}$ are equivalent to conditions on time. Now consider what happens to the function $f(r, \gamma, t)$ if the integration is not performed over the entire interval.

We evaluate τ at two extreme values of γ_0: $\tau(\gamma, \gamma) = 0$ and $\tau(\gamma_{\max}, \gamma) = \tau_{\max}$ as indicated in Fig. 3.2 and Fig.3.3. Fixing time t_1, when the source starts to emit particles, and time t_2, at which the source is no longer emitting particles, we study the variation of the interval of integration with time. As we vary t, the window $[t - t_2, t - t_1]$ moves along the y-axis of a graph of $\tau(\gamma_0, \gamma)$ vs γ_0 (Fig. 3.2) from which we can determine the limits of integration. Indeed, the interval of integration will simply be the inverse image in τ of the overlap of the window $[t - t_2, t - t_1]$ with the interval $[0, \tau_{\max}]$.

Consider the following cases at two fixed points on the curve:

- If $t - t_1 = 0$ then $t = t_1$ and $f(r, \gamma, t) = 0$ as the source is not yet active.
- If $t - t_1 = \tau_{\max}$ then $t = t_1 + \tau_{\max}$ and $f(r, \gamma, t)$ will have enough time to get to steady state within the bracket.
- If $t - t_2 = 0$ then $t = t_2$ and $f(r, \gamma, t)$ starts to decrease as the source is no longer active.
- If $t - t_2 = \tau_{\max}$ then $t = t_2 + \tau_{\max}$ and $f(r, \gamma, t) = 0$ as the decreasing of the function has come to an end.

We should also note that if the window size $t_2 - t_1 < \tau_{\max}$, the two conditions $\gamma_0^{(1)} > \gamma_{\max}$ and $\gamma_0^{(2)} < \gamma_{\max}$ cannot be satisfied together. The function $f(r, \gamma, t)$ will not become steady on the given integration limit and will therefore continuously change with time. This implies $\tau_{\max}$ is the required time difference between t_1 and t_2 for the density distribution to reach equilibrium. Note that when equilibrium is attained, this equilibrium is temporary, lasting for time $t_2 - t_1 - \tau_{\max}$ (until the source stops injecting at time t_2).

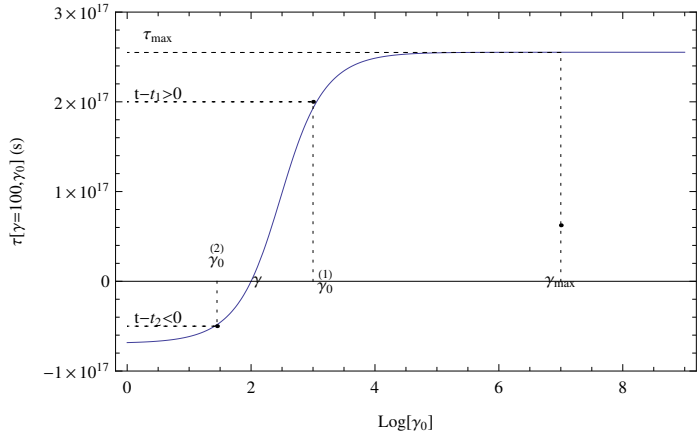

Figure 3.3: τ a strictly monotone increasing function of γ_0 at a fixed value of $\gamma = 100$.

Calculating $\gamma_0^{(1)}$ and $\gamma_0^{(2)}$

We now turn our attention to the numerical calculation of $\gamma_0^{(1)}$ and $\gamma_0^{(2)}$ in Eq.(3.23).

To obtain $\gamma_0^{(1)}$ we need to solve Eq.(3.21) and we let

$$f_1(\gamma_0) = \tau(\gamma_0) - t + t_1.$$

If $t - t_1 < 0$: we know that $\gamma_0^{(1)} < \gamma$ and the solution at that point is zero since it is before the injection begins.

If $t - t_1 > \tau_{\max}$: we know that $\gamma_0^{(1)} > \gamma_{\max}$ and hence the value of $\gamma_0^{(1)}$ is irrelevant, as the density of electrons has already reached the equilibrium point.

Otherwise,

$0 < t - t_1 < \tau_{\max}$.

Therefore $f_1(\gamma_0 = 1) < 0$, $f_1(\gamma_0 = \gamma_{\max}) > 0$ and thus we have established an initial bracket on the solution of $f_1(\gamma_0)$. A numerical bracketing method for zero finding such as the Method of False Position[3] works very nicely to find the zero from here.

Similarly when finding $\gamma_0^{(2)}$ we need to solve Eq.(3.22) and we let

$$f_2(\gamma_0) = \tau(\gamma_0) - t + t_2.$$

Once more we only calculate the solution if $0 < t - t_2 < \tau_{\max}$, otherwise it is irrelevant to calculate the values of $\gamma_0^{(2)}$ as it is either before injection has begun or after equilibrium is reached. Thus we have $f_2(\gamma_0 = 1) < 0$ and $f_2(\gamma_0 = \gamma_{\max}) > 0$ and hence we have once more established an initial bracket. With the integral only being evaluated over this (often much smaller) region on which the theta functions are nonzero, numerical integration methods are faster and more accurate.

3.6 Numerical Results

Having simplified the expressions for the integral in Eq.(3.15) and Eq.(3.23), for steady injection and time dependent injection respectively, numerical integration can now be performed. A Gauss-Kronrod integrator was implemented to accomplish this. Gauss-Kronrod is an extended version of the Gaussian Quadrature approach to integration. Gaussian Quadrature uses optimal sampling points (found by polynomial interpolation) and weights to approximate the integral by a weighted sum of integrand values taken at these points. Unfortunately, it is not possible to re-use points from low-order Gaussian Quadrature rules in higher order Gaussian Quadrature rules (in an analogous way to how one does with the Trapezoidal rule, for instance). The fix is to use the Kronrod extension, which adds new sampling points in

[3]The Method of False Position finds the zero of the straight line joining the two end-points of the bracket on every step : $c = \frac{af(b) - bf(a)}{f(b) - f(a)}$

between the Gaussian points and forms a higher order rule that re-uses the Gaussian Quadrature integrand evaluation. The numerical values presented in the Table3.1 were used to obtain the steady state solution as well as the time dependent solution.

Table 3.1: Table of quantities used to obtain the numerical solution.

Symbol	d_0	β_μ	n_{th}	r_s	Q_0	ρ	T	γ_{Max}
Value	$10^{28} cm^2 s^{-1}$	1μG	$10^{-3} cm^{-3}$	$1 Mpc$	$10^{-3} cm^{-3} s^{-1}$	2.4	$10^{20} s$	10^7

3.6.1 Solution for steady Injection

Using the values in Table 3.1, the following results were obtained. Fig.3.4 represents the number density of relativistic electrons, for a steady source, as a function of r with various γ values. Note that with an increase in γ the number density drops. This is also seen in Fig.3.5 where number density is plotted as function of γ with varying values of r.

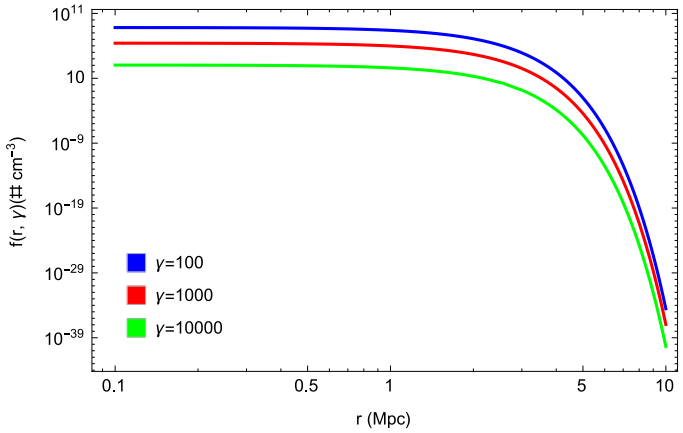

Figure 3.4: Number density of relativistic electrons as a function of radius with varying γ obtained using the numerical values in Table 3.1. As expected, the number density of relativistic electrons drops with an increase in γ.

The electron density as a function of radius at varying values of T is presented in Fig.3.6. For $T > 10^{17}$s the electron density changes only very slightly with change in T. We notice that for electrons the term $\frac{f}{T}$ is negligible for $T > T_U$, where $T_U = (4.354 \pm 0.012) \times 10^{17}$s is the age of the universe. Furthermore, the change in electron number density with various diffusion coefficients is presented in Fig.3.7. Note with a large value of d_0, the number density disperses quickly and the central density is smaller.

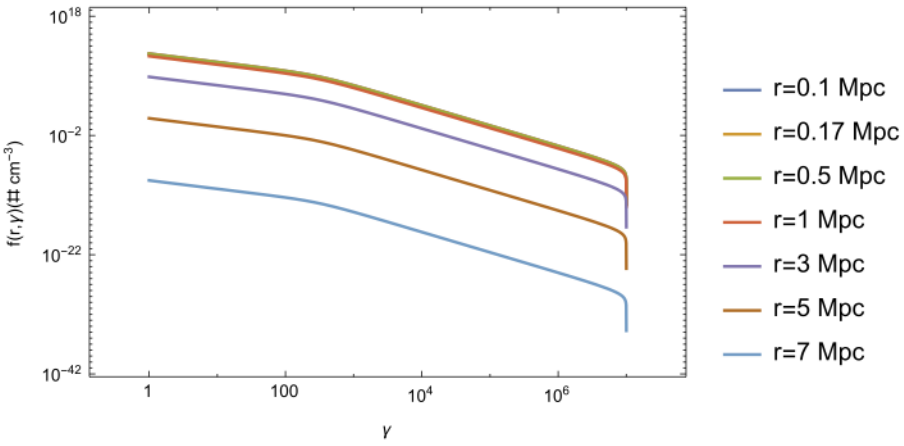

Figure 3.5: Number density of relativistic electrons as a function of γ with varying r, using the numerical values in Table 3.1.

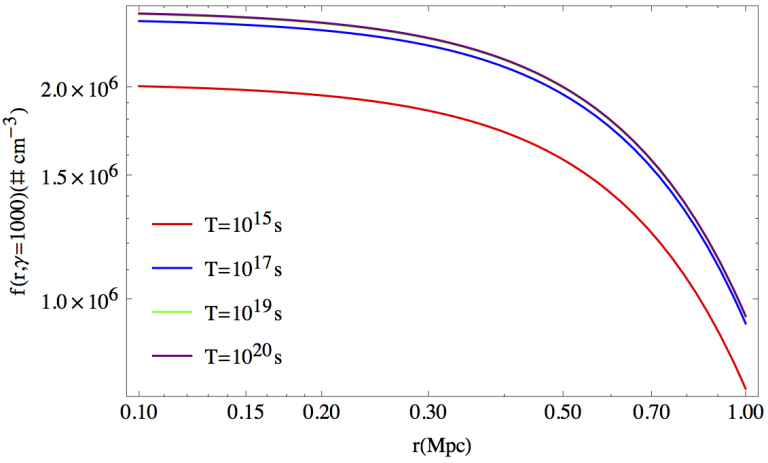

Figure 3.6: Number density of relativistic electrons as a function of radius with varying T obtained using the numerical values in Table 3.1. For $T > 10^{17}$s there is a small difference in the electron density and it appears to be the same for $T = 10^{19}$s and for $T = 10^{20}$s.

3.6.2 Time-dependent Solution

Here we discuss the time-dependent solution for the diffusion of relativistic electrons. Just as before the final integration in Eq.(3.23) is solved numerically using the Gauss-Kronrod rule of integration. The numerical constants used to obtain these solutions are listed in Table 3.1. A time dependent source, which starts to inject electrons at time t_1 and stops injecting electrons at time t_2, is used. The values $t_1 = 10^{15}$s and $t_2 = 10^{17}$s are used. Behaviour of the relativistic electron density as a function of time for different values of γ and for a fixed value

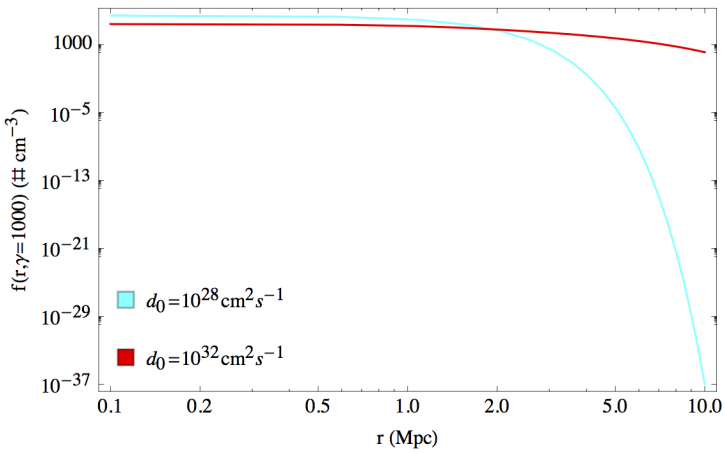

Figure 3.7: Density as a function of radius, with $\gamma = 1000$, and varying diffusion coefficient d_0. It is clear from the plot that for a large value of the diffusion coefficient the electron density disperses very quickly within a small radius.

of the radius $r = 0.17$ Mpc is presented in Fig.3.8. As $t \to t_2$ the solution becomes steady. Also, at higher energy the solution reaches steady state earlier. However, note that at $\gamma = 100$ and $\gamma = 10$, i.e. lower values of γ, the solution continues to increase while the electrons are injected and after that time starts to decrease without ever reaching equilibrium. This is in agreement with results obtained above, where for small window sizes $t_2 - t_1 < \tau_{\max}$, the solution will not reach steady state. Hence, the minimum value of $\gamma_{\rm eq}$, for which equilibrium is possible can be calculated for given values of t_1 and t_2 by $\tau(\gamma_{\rm eq}, \gamma_{\max}) = t_2 - t_1$. And so for $\gamma < \gamma_{\rm eq}$, the solution will continuously increase as $t \to t_2$ and once $t > t_2$ it will decrease rapidly and eventually becomes zero (see Fig.3.9).

Furthermore, the effect of increasing and decreasing Q_0 is presented in Fig.3.10 for $\gamma = 1000$ and $r = 0.17$ Mpc. The dashed line in the figure represents $t = t_2$. This plot physically makes sense as Q_0 represents the injection rate and therefore increasing/decreasing its value will result in a corresponding increase/decrease in the solution, i.e. the solution is linear in Q_0. This is immediate from the Green's Function solution because Q_0 can be taken out of the integral.

In Fig.3.11 we study the change in value of T, which is defined by Syrovat-skii as the average lifetime of particles(1959). We see how varying T at $\gamma = 10$, 1000 and 10000 changes the solution. Varying T changes the solution very slightly for values that are close to the age of the Universe but for smaller values there is a significant drop in the numerical solution.

Next we study the effect of changing the value of the diffusion coefficient d_0 for the

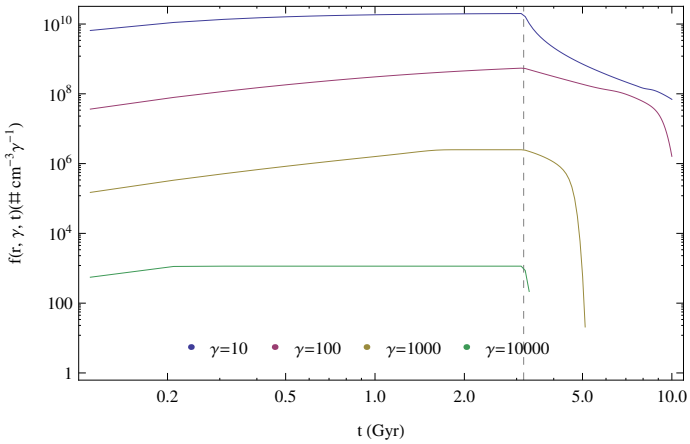

Figure 3.8: Electron density as a function of t for $r = 0.17$ Mpc and various values of γ. The dashed line is at $t_2 = 3.17$ Gyr. At higher energy the density of relativistic electrons reaches steady state in a relatively short time.

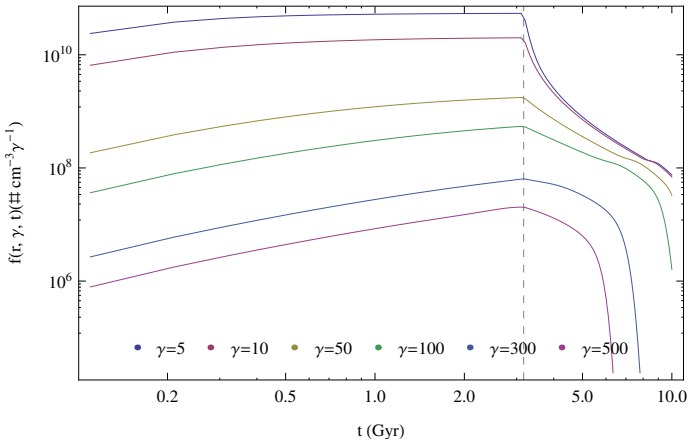

Figure 3.9: Electron density as a function of t for $r = 0.17$ Mpc and various values of γ for $\gamma < \gamma_{eq}$, in this case $\gamma_{eq} = 589.936$. The dashed line is at $t_2 = 3.17$ Gyr. It is clear that for the above values of γ the solution does not reach stability.

time dependent solution. To understand the effects of diffusion over time on the density of relativistic electrons, we plot the solution for various d_0 and γ values in Fig.3.12. In this case we note that the diffusion coefficient for $d_0 < 10^{28}\text{cm}^2\text{s}^{-1}$ is negligible. However, for large values of $d_0 >> 10^{28}\text{cm}^2\text{s}^{-1}$, the diffusion coefficient cannot be neglected.

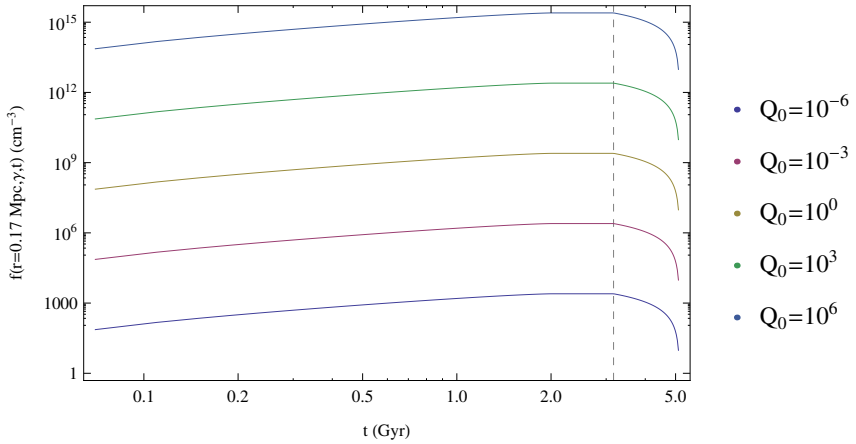

Figure 3.10: Density as function of time with varying values of Q_0 and $\gamma = 1000$. Note that the increasing Q_0 increases the values of number density and does not change the shape of the curve.

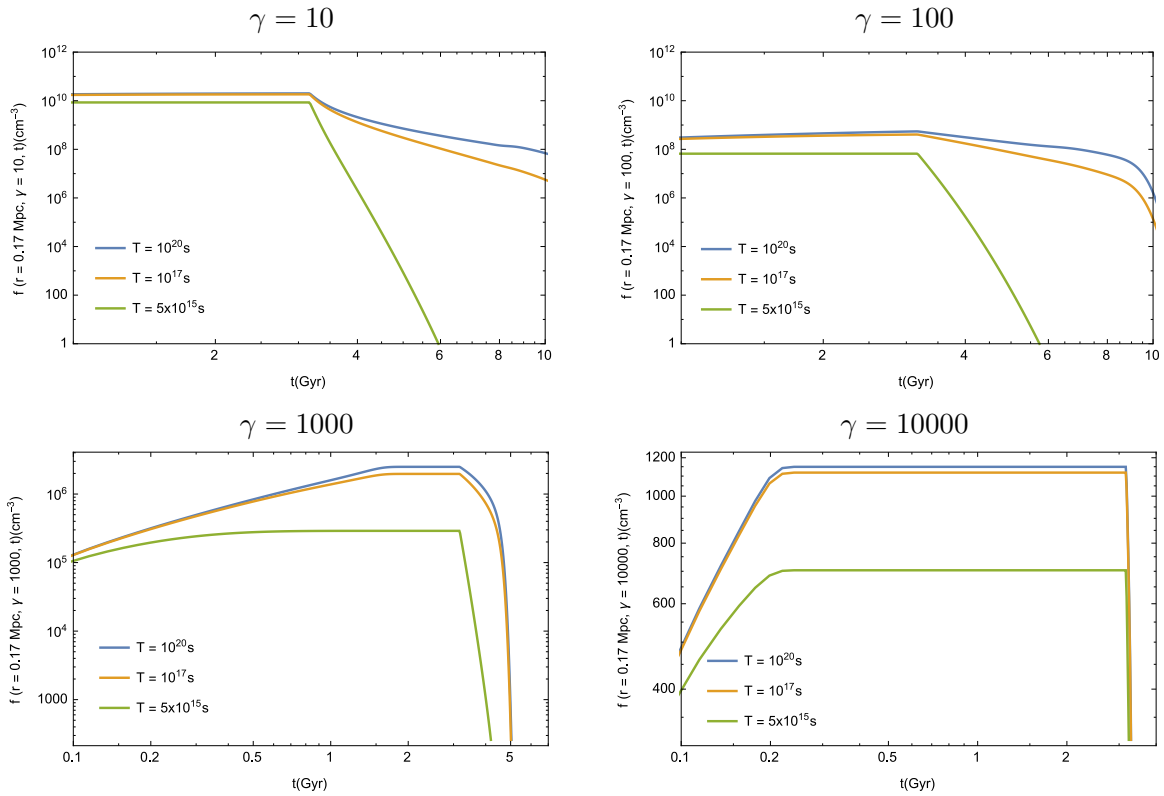

Figure 3.11: Electron density as a function of time for $r = 0.17$ Mpc and varying T, the average lifetime of particles, at various γ values.

3.7 Comparison with previous results

We now compare the solutions we have obtained using the model to existing solutions in the literature. The steady state solution of the model is compared to the steady state solution

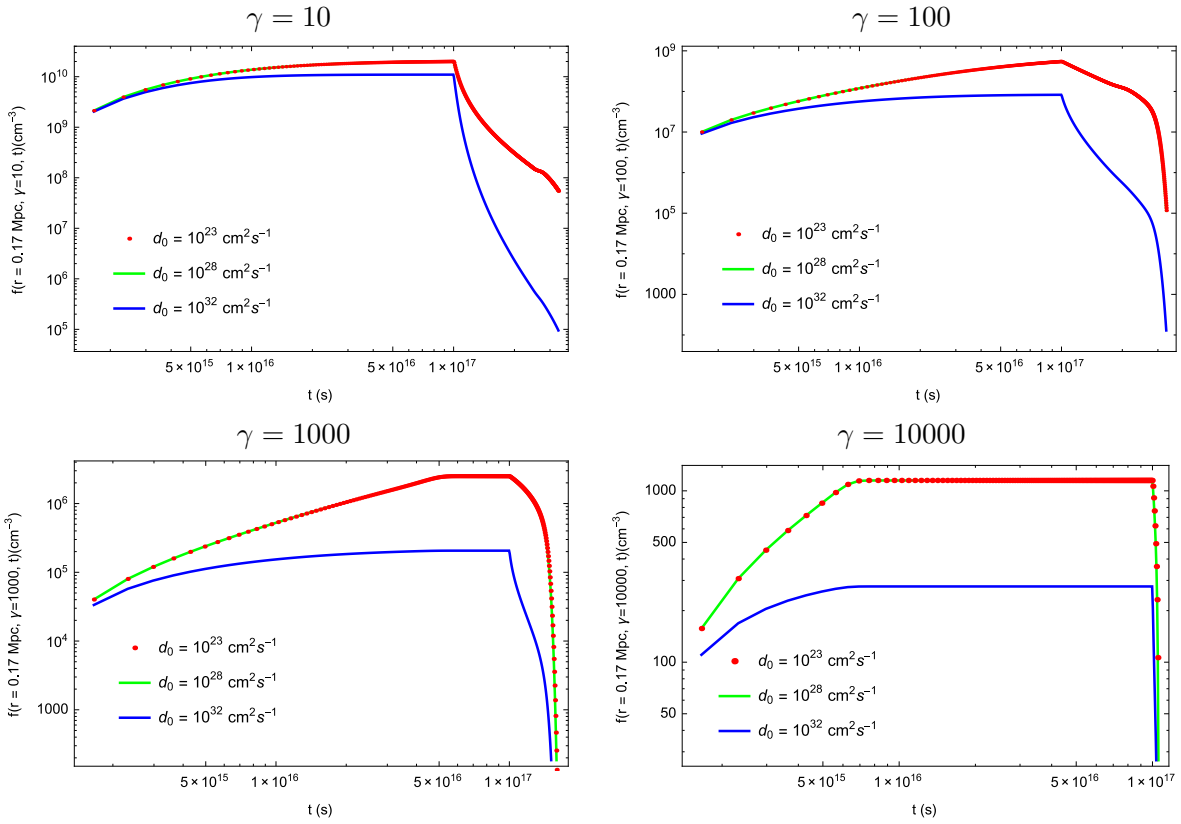

Figure 3.12: Density as a function of time for $r = 0.17$Mpc and $\gamma = \{10, 100, 1000, 10000\}$ for three different values of d_0. It is clear that for $d_0 >> 10^{28}\text{cm}^2\text{s}^{-1}$, the diffusion term cannot be neglected.

presented in Colafrancesco et al. (2006) as well as to the equilibrium solution calculated without the effects of diffusion. For each method a brief description is provided, the solution is obtained, and then results from are compared.

3.7.1 Solution from Colafrancesco et al. (2006)

The transport of relativistic particles from a source is described, in Colafrancesco et. al (2006), by the following equation taking the diffusion and energy losses of particles into account. Here, $\frac{dn_e}{d\gamma}$ is the same as f in Eq.(3.1):

$$\frac{\partial}{\partial t}\frac{dn_e}{d\gamma} - D(\gamma)\Delta\frac{dn_e}{d\gamma} - \frac{\partial}{\partial\gamma}\left[\tilde{b}(\gamma)\frac{dn_e}{d\gamma}\right] = Q(\mathbf{r},\gamma,t). \tag{3.24}$$

Note that in this case there is a difference in the definition of the loss term, because $\tilde{b}(\gamma) =$

$-\frac{d\gamma}{dt}$. These authors derived the Green's function by change of variables as follows:

$$\tilde{b}(\gamma)\frac{dn_e}{d\gamma} = -\frac{dn_e}{du} \tag{3.25}$$

which yields

$$u = \int_{\gamma}^{\gamma_{\max}} \frac{d\gamma'}{\tilde{b}(\gamma')}. \tag{3.26}$$

Transforming the equation (3.24) in terms of u:

$$\left[-\frac{\partial}{\partial t} + D(\gamma)\Delta - \frac{\partial}{\partial u}\right]\frac{dn_e}{du} = \tilde{b}(\gamma)Q(\mathbf{r},\gamma,t), \tag{3.27}$$

The Green's function is then determined by taking the four-dimensional Fourier transform of (3.27), in $(t \to \omega, \mathbf{r} \to \mathbf{k})$ and thereafter transforming back to $(t, \mathbf{r})$:

$$G_{free} = -\frac{1}{(4\pi(v-v'))^{3/2}}\exp\left[-\frac{|\mathbf{r}-\mathbf{r}'|^2}{4(v-v')}\right]\delta((t-t')-(u-u')) \tag{3.28}$$

where $v = \int_{u_{min}}^{u} d\tilde{u}D(\tilde{u})$ and the suffix *free* denotes that there are no boundary conditions. To obtain the solution of the equation (3.24), the authors further used the method of image charges, first described for this particular problem by Baltz and Edsjö (1999) and Baltz and Wai (2004), to implement boundary conditions. The approximation of spherical symmetry with Green's function vanishing at radius r_h was considered by introducing a set of image charges $(r_n, \theta_n, \phi_n) = ((-1)^n r + 2nr_h, \theta, \phi)$. Furthermore, Colafrancesco et al. (2006) chose their reference frame along the z polar axis ($\cos\theta = 1$) such that $|\mathbf{x}-\mathbf{x}'| = (r'^2 + r_n^2 - 2r'r_n\cos\theta')$. Assuming that the source function is independent of θ' and ϕ', integrals over these variables are performed explicitly and the analytical solution is given by:

$$\frac{dn_e}{d\gamma} = \frac{1}{\tilde{b}(\gamma)}\int_{\gamma'=\gamma}^{\gamma_{\max}} d\gamma' \frac{1}{(4\pi(v-v'))^{1/2}}\sum_{n=-\infty}^{\infty}(-1)^n$$
$$\int_{r'=0}^{r_h} dr' \frac{r'}{r_n} t\left[\exp\left(-\frac{(r'-r_n)^2}{4(v-v')}\right) - \exp\left(-\frac{(r'+r_n)^2}{4(v-v')}\right)\right] Q_e(r',\gamma',t'). \tag{3.29}$$

The steady state solution of Eq.(3.24) derived from the Green's function is:

$$\frac{dn_e}{d\gamma} = \frac{1}{\tilde{b}(\gamma)}\int_{\gamma'=\gamma}^{\gamma_{\max}} d\gamma' \hat{G}(r, v-v')Q_e(r',\gamma'), \tag{3.30}$$

where

$$\hat{G}(r, v - v') = \frac{1}{(4\pi(v - v'))^{1/2}} \sum_{n=-\infty}^{\infty} (-1)^n \times$$

$$\int_{r'=0}^{r_h} dr' \frac{r'}{r_n} \left[\exp\left(-\frac{(r' - r_n)^2}{4(v - v')} \right) - \exp\left(-\frac{(r' + r_n)^2}{4(v - v')} \right) \right]. \tag{3.31}$$

3.7.2 Equilibrium Solution Without the Effects of Diffusion

The equilibrium solution is obtained by letting $\frac{\partial f}{\partial t} = 0$ and neglecting the diffusion term in Eq.(3.24). The expression for equilibrium number density becomes (e.g. Sarazin 1999):

$$f_{eq}(\mathbf{r}, \gamma) = \frac{1}{|b(\gamma)|} \int_{\gamma}^{\gamma_{Max}} Q(\mathbf{r}, \gamma') d\gamma'. \tag{3.32}$$

The differences between the equilibrium solution and the steady state solution derived from the Green's function are the spatial diffusion factor in the integrand as seen above, i.e. the factor $f_G(\mathbf{r}, \gamma; \mathbf{r_0}, \gamma_0)$ in Eq.(3.13) and the factor $\hat{G}(r, v - v')$ in Eq.(3.31) as well as the presence of the quantity T.

3.7.3 Differences in Equations and Definitions

Comparing the diffusion equation Eq.(3.1) and Eq.(3.24), we observe that the signs of the loss term functions are different, i.e. the third term is positive in the equation (3.1) but negative in equation (3.24). This dissimilarity is due to their different definitions of the loss function $b(\gamma)$: $b(\gamma) = \frac{d\gamma}{dt}$ in Syrovatskii (1959) and $\tilde{b}(\gamma) = -\frac{d\gamma}{dt}$ in Colafrancesco et al. (2006). However, this difference is accounted for by the latter author by using a positive function of $b(\gamma)$.

There is also the extra term, $\frac{f}{T}$, in equation (3.1), which is negligible for large values of T (see Fig.3.13). The numerically obtained steady state solution for large values of T is similar to the equilibrium solution of equation (3.32). The other key difference is that Colafrancesco et al. (2006) implemented the method of image charges to the boundary free Green's function as shown above. This results in the change of boundary conditions over the spatial distribution. The role of the spatial distribution is described in detail below.

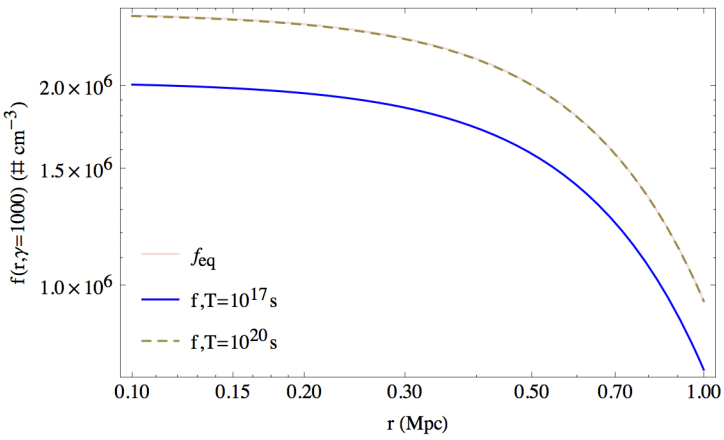

Figure 3.13: Density as a function of radius with constants, $\gamma = 1000$, diffusion coefficient $d_0 = 10^{28} cm^2 s^{-1}$, $\beta = 1\mu$G, and $\rho = 2.4$. The two numerical solutions for different values of T are compared with the equilibrium solution f_{eq}. For $t = 10^{20} s$, the solution is the same as the equilibrium solution.

3.7.4 Comparison of Solutions

In this section, the solution of Eq.(3.13) is compared to the numerical solutions of Eq.(3.31) and Eq.(3.32). It is clear from Fig.3.14 that the solutions in both cases are similar. Firstly, the plots of number density as a function of radius are obtained for both the Eq.(3.13) and Eq.(3.31) with the constants tabulated in Table 3.1 and $r_h = 10$ Mpc. It is evident from these solutions that the spatial distribution boundary conditions are insignificant for the steady state solution if $r_h >> r_s$; however for $r_h \leq r_s$ boundary conditions cannot be neglected. In Fig.3.15, a slight variation in the solution at smaller radius (at the centre of an object) is observed, which agrees with the results of Colafrancesco et al. (2006). Furthermore, the density distributions of relativistic electrons from different solutions are compared at different energies in Fig.3.16, and it is clear that the results are in good agreement.

The equilibrium solution is independent of the diffusion coefficient but the stationary solutions of Eq.(3.1) and Eq.(3.24) obtained from their respective Green's functions, are dependent on the diffusion coefficient. For a typical value of the diffusion coefficient $d_0 = 10^{28} cm^2 s^{-1}$ the steady state solution is similar to the equilibrium solution as seen in Fig.3.14. With a large value of the diffusion coefficient, for e.g $d_0 = 10^{32} cm^2 s^{-1}$, the solutions are different as the electron number density disperses faster (see Fig.3.7) and hence large d_0 can't be disregarded when calculating the equilibrium solution from the diffusion equation.

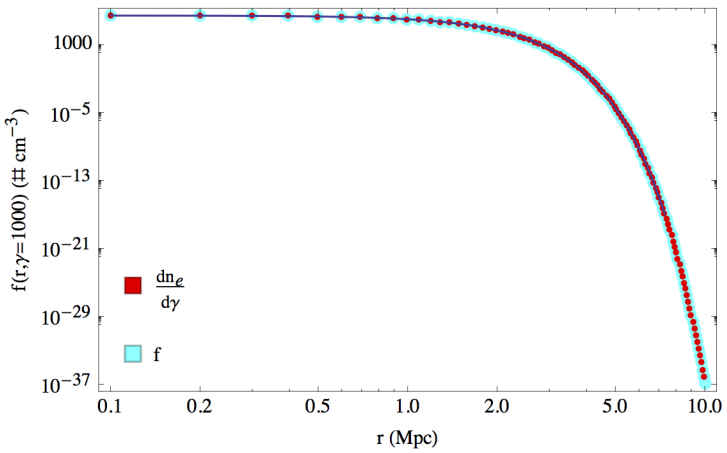

Figure 3.14: In this figure the solid line represents the equilibrium solution of Eq.(3.32), $\frac{dn_e}{d\gamma}$ - the solution of Eq.(3.31) and f - the solution of Eq.(3.13). The numerically solved solutions are in agreement with the analytical solution of the Eq.(3.32).

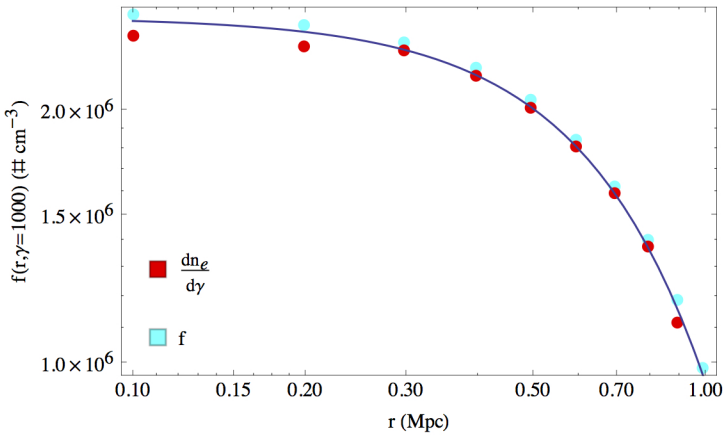

Figure 3.15: This figure is the zoomed in version of Fig.3.14 to see the change in electron number density at smaller radius. Here, number density slightly varies for each of the numerical solutions at the centre of the object. This result is in agreement with that of Colafrancesco et al. (2006)

3.8 Conclusion

In this chapter we presented a way to obtain the solution of the diffusion equation for relativistic electrons under very general conditions. We found that the solutions from the literature are particular cases of our general solution and they coincide with our solution when the same assumptions are made. Since the solutions we obtained are very general, they can be applied

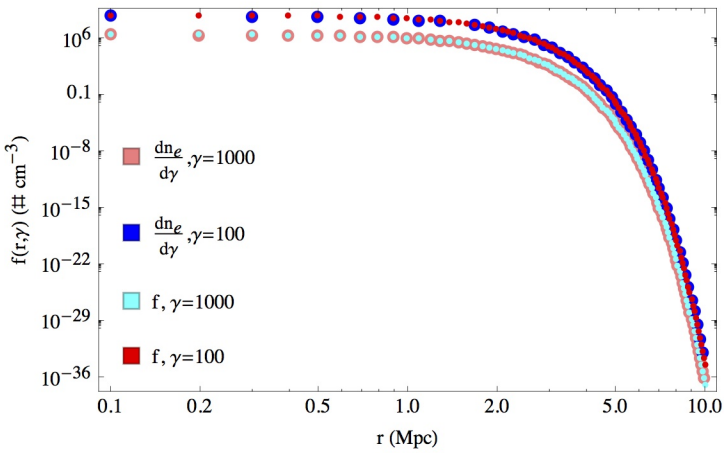

Figure 3.16: Electron number density as function of r with varying γ. The results are similar for both methods.

to different problems with different conditions. Therefore they allow us to study different systems with varying conditions related to the origin and evolution of relativistic electrons.

In subsequent chapters, we make use of this general solution to study the spectral, spatial and temporal properties of radio halos both in the case of a single galaxy and in the case of galaxy clusters.

Chapter 4

Galaxy Radio Halo: Case of M51

"It doesn't matter how beautiful your theory is, it doesn't matter how smart you are. If it doesn't agree with experiment, it's wrong."

-Richard P. Feynman

4.1 Introduction

Since our proposed model claims that cluster radio halos are the sum of galactic radio halos, we must first discuss the formation and evolution of typical radio halos in galaxies in order to understand cluster radio halos.

We use the general solution of the diffusion equation derived in previous chapter to study the spatial and spectral properties of galactic radio halos. We have chosen as a benchmark the radio galaxy M51, a nearby object that is well studied.

We begin by describing some observed properties of the galaxy M51 and explaining why we chose this galaxy to test our model in section 4.2. Thereafter, in section 4.3 we describe the observational data we are using to test our model, and apply our model to reproduce the spectral and spatial properties in this data by varying the parameters and comparing our solutions to the observed data. We then calculate the evolution of these properties in the rest frame of M51 (section 4.4) and at different redshifts in section 4.5 and finally present our conclusions in section 4.6.

4.2 Observations of M51

The galaxy M51 is a spiral galaxy which is classified as "grand design" because the spiral arms are well defined, long, symmetrical and dominate the appearance of the galaxy (see, Elmegreen

and Elmegreen (1982; 1987)). Because it is one of the nearest galaxies and because it is oriented nearly face-on (see Fig.4.1), it is an ideal candidate for the study of star populations and morphology at several spectral bands, e.g. optical , infrared, UV, radio and X-rays.

Figure 4.1: An optical image of the galaxy M51 taken with the 0.9-meter telescope located at Kitt Peak National Observatory. Image credit:T.A.Rector and Monica Ramirez/NOAO/AURA/NSF

The galaxy M51 is interacting with the dwarf galaxy NGC 5195 (Vorontsov-Velyaminov, 1959). This interaction, however, does not have a strong effect on the star formation rate (SFR) as the measured SFR is moderate, $3.4\,M_{\odot}\mathrm{yr}^{-1}$(Calzetti et al., 2005). The SFR in the external disk has been measured to be smaller than the SFR in the internal part of the galaxy by an order of magnitude (Thornley et al., 2006). It has also been observed that the neutral gas emission follows the spiral arms closely (Rots et al., 1990). Some observations in optical and radio (see e.g., Ford et al. (1985)) show the presence of a bipolar jet which is produced by a low-luminosity Seyfert 2 nucleus.

An extended radio emission (see Fig.4.2) is observed in this galaxy at various frequencies (see Mulcahy et al. (2014) and references therein). From these observations we have detailed information about the integrated spectrum of the radio halo and about its spatial properties. The radio emission is polarised (Mathewson et al., 1972) and appears to originate from both the disk and the spiral arms; the pattern of magnetic field lines seem to follow the pattern of the spiral arms observed in optical images (e.g. Fletcher et al. (2011)).

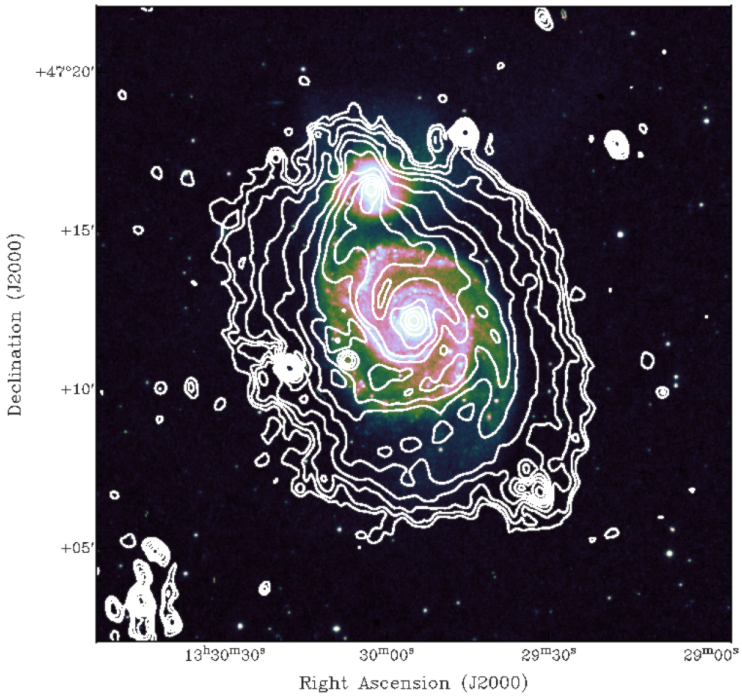

Figure 4.2: M51 at a central frequency of 151 MHz overlayed onto an optical DSS image from Mulcahy et al. (2014).

Recently Mulcahy et al. (2014) observed the radio halo of M51 using LOFAR at 151 MHz. Together with the previously measured flux they found that the integrated spectrum of the total radio emission is well described by a power law with a constant spectral index $\alpha = 0.79 \pm 0.02$ in the frequency range $0.15 - 22.8$ GHz, without any clear indications of steepening/flattening in the spectrum. They also measured spectral index as a function of position in the galaxy and found a decrease in spectral index with increasing radius. Furthermore, they found a steepening of the spectral index in the inter-arm regions compared to the value measured in the arms.

In their study the radio halo emission was detected out to a radius of 16 kpc with confidence level 3σ. This result was compared to the extension of the halo observed at 1.487 GHz by Fletcher et al. (2011) using VLA. This comparison shows that the extended radio emission is detected out to a smaller radius, approximately 11 kpc, at high frequency. A break in the radial surface brightness slope was observed at both frequencies 151 MHz and 1.487 GHz at radius of about 10 kpc (see Fig. 4.3).

These authors further calculate magnetic field as function of radius using the simple equipartition assumption between cosmic rays and magnetic field. The results of this calculations show that the magnetic field in the central region decreases rapidly from $\sim 30\,\mu$G to

$\sim 15\,\mu$G between 0 and 2 kpc. In the intermediate region ($2-5$ kpc) the mean value is almost constant around $15\,\mu$G while in the external region with $r > 5$ kpc the magnetic field shows a slow and constant decrease to the value of 10 μG at radius 12 kpc.

By comparing the observations in the spiral arm and the inter-arm region, these authors conclude that the effects of spatial diffusion of electrons in this galaxy are very important, with the estimated value of the diffusion coefficient $D \simeq 3.3 \times 10^{27}$ cm^2 s^{-1}. For this reason it is important to consider the full version of the diffusion equation to model the extended radio emission from this galaxy.

4.3 Modelling the Radio Emission of M51

Here we model the radio emission of M51 by using the general solution of the diffusion equation described in section 3.6. In our method we make some assumptions regarding the properties of the source term and then numerically solve the diffusion equation. Using the result of this computation we calculate the synchrotron radio emission (see Appendix A) and compare the results with the observed emission from M51. For this comparison we use the data on the spectrum (see Table 4.1) and the surface brightness at different frequencies of 151 MHz and 1.487 GHz (see Fig.4.3). Using these data we find the best fit parameters and the source terms in our model.

Table 4.1: Table of integrated flux density at various values of frequency (ν), as presented in Mulcahy et al. (2014) from various papers in the literature.

ν(GHz)	Flux Density (Jy)	Reference
22.8	0.147±0.016	Klein et al.(1984)
14.7	0.197±0.021	Klein et al.(1984)
10.7	0.241±0.041	Klein and Emerson(1981)
8.46	0.308±0.103	Dumas et al.(2011)
4.86	0.604±0.201	Fletcher et al.(2011)
2.604	0.771±0.049	Klein et al.(1984)
1.49	1.36±0.09	Fletcher et al.(2011)
0.61	2.63±0.06	Segalovitz(1977)
0.408	3.5±0.1	Gioia and Gregorini(1980)
0.15	6.9±0.69	Hales et al.(1988)
0.15	6.48±0.65	Waldram et al.(1996)
0.15	8.1±0.6	Mulcahy et al.(2014)
0.0575	11±1.5	Israel and Mahoney(1990)
0.0263	31±8	Viner and Erickson(1975)

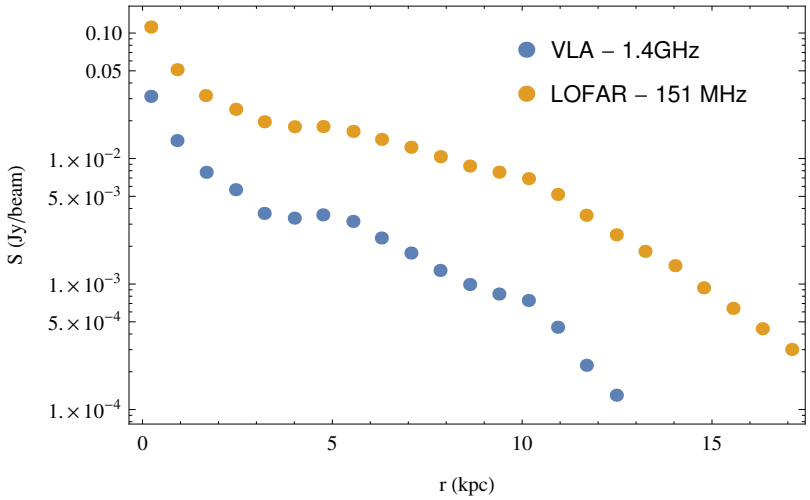

Figure 4.3: The radial profile of M51 at 151 MHz and 1.4GHz extracted from Mulcahy et al. (2014). These authors derive the radial profile by averaging the surface brightness in concentric rings at corresponding frequencies.

4.3.1 Basic Model: Single Gaussian Source

The model described in sections 3.2 – 3.6 is used to fit the observed data presented above. In this model it is necessary to assume some properties of the source term $Q(r, \gamma, t)$ and the properties of the environment of the galaxy (i.e. magnetic field β_μ, thermal gas n_{th}, diffusion d_0 and lifetime of particles T). For some of these parameters we chose reference values: $d_0 = 10^{28}\text{cm}^2\text{s}^{-1}$, which is of the order of magnitude of the values usually assumed in literature (e.g. (Syrovat-skii, 1959)) and it is in between the values estimated by Mulcahy et al.(2014) (3.3×10^{27} cm^2 s^{-1}) and Moskalenko and Strong (1998)($(2-4) \times 10^{28}$ cm^2 s^{-1}); $T = 10^{20}$ s – we assume a high value of the average lifetime of electrons because we assume that the effects of T are not important compared to the radiative losses of electrons, this is verified mathematically in section 3.6; $n_{th} = 10^{-3}$ cm^{-3}, a reference value that is typical in a cluster of galaxies. We believe that this value of n_{th} is acceptable in the calculation of synchrotron emission since the effects of thermal density appear in the Bremsstrahlung and Coulomb losses, which affect the lower part of the electron spectrum, and electrons with lower energy are not important for synchrotron emission in the frequency range. Furthermore, in the expression of the plasma frequency the effects of n_{th} are small.

Other parameters were fixed on the basis of observations: the source spectral index $\rho = 1.58$ was derived from the spectrum of the radio flux α using the well known relation $2\alpha = P - 1$, where P is the equilibrium spectral index of electrons which in our case is related to the spectral index ρ of the source by $P = \rho + 1$ as a result of diffusion equation. The magnetic

field $\beta_\mu = 15\,\mu$G was chosen as a constant value in order to simplify the calculations. We expect that this assumption is not overly harsh for three reasons: firstly, the chosen value coincides with the average value of the magnetic field over the spatial region where the latter is quite flat; secondly, the central region where the magnetic field has a strong peak is quite small; and finally the decrease in magnetic field at high radius is slow.

In the model we assume that the source M51 emits particles from time $t_1 = 10^{15}$s to time $t_2 = 10^{17}$s. These values were chosen arbitrarily. The flux and radial profile of M51 are calculated at time $t = 10^{17}$s, corresponding to the value of t_2 at which the injection of electrons has ended. This value of t does not correspond to the age of the galaxy, but this is not important because only the time differences $t-t_1$ and $t-t_2$ are important in our proposed model. To obtain real values of time with respect to the age of the universe it is sufficient to rescale these numbers to the appropriate time derived from the cosmological model. We will do this in the next section when we consider the evolution with redshift of the spectrum and surface brightness of the galaxy.

The luminosity distance of M51, $D_L = 7.6$ Mpc, was obtained from Ciadullo et al. (2002).

Table 4.2: Parameters based on reference values and on observations used to obtain solutions of the model.

Symbol	d_0	T	n_{th}	ρ	t_1	t_2	t	D_L
Value	$10^{28}\text{cm}^2\text{s}^{-1}$	$10^{20}s$	10^{-3} cm^{-3}	1.58	10^{15}s	10^{17}s	10^{17}s	7.6 Mpc

The free parameters in the model are Q_0, the normalisation parameter; r_s, the width of the Gaussian source; and R_{max}, the distance to which the Gaussian can extend. In order to determine if the single Gaussian source $Q_r(r_0)$ defined in section 3.3 could fit the observed data, we used the model to calculate surface brightness and flux tables for various values of Q_0, r_s and R_{max}:

$$Q_r(r_0) = Q_0 \exp\left(-\frac{r_0}{r_s}\right)^2 \qquad \text{for } r_0 \leq R_{max}.$$

Due to computing time and resource constraints, we evaluated the model over a finite mesh in radii with step size 0.5 kpc of r_s and 1 kpc for R_{max} values. Our reference data are of the form:

$$\{(r_i, S_i)|i = 1, 2, 3, ...\},$$

where r_i is the radius and S_i is the corresponding surface brightness at given frequencies of 151 MHz and 1.487 GHz, as seen in the Fig. 4.3. The objective function for evaluating our model is the least squares error from the observed value, i.e.

$$g(r_s, Q_0, R_{max}) = \Sigma_i (S(r_i; r_s, Q_0, R_{max}) - S_i)^2,$$

where $S(r_i; r_s, Q_0, R_{max})$ is the surface brightness evaluated at r_i at a fixed frequency described in Appendix A with r_s, Q_0 and R_{max}. Note that there are no error bars in the reference data and therefore we cannot make use of sophisticated statistical model fitting in this case. It is sensible, therefore, to assume that the errors are independent and identically normally distributed, and therefore the maximum likelihood model will be the one that minimises the sum of squares error, g. We picked r_s, Q_0, and R_{max} so as to minimise this error by performing a grid search over r_s and R_{max} values and then a subsequent numerical minimisation of the objective function g as a function of Q_0 for each fixed r_s and R_{max} value.

The basic model was fitted with $r_s = 0.008$ Mpc, $Q_0 = 4 \times 10^{-24}$ cm^{-3} s^{-1} and $R_{max} = 18$ kpc. The flux predicted by this model fits the observed flux quite well (see Fig.4.4). However, the predicted surface brightness does not fit the observed data for the surface brightness satisfactorily, as indicated in Fig.4.5 because it is not able to fit the data at smaller radius (≤ 3 kpc).

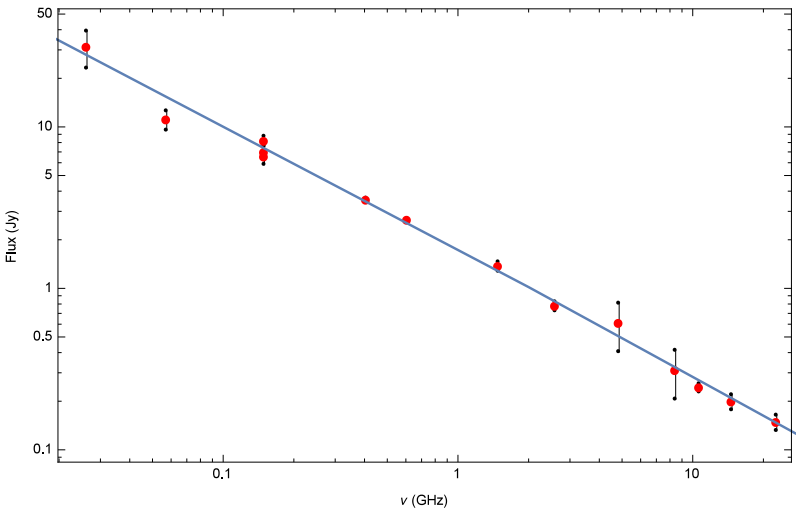

Figure 4.4: Flux density fitted to data presented in Table 4.1 with $r_s = 0.008$ Mpc and $Q_0 = 4 \times 10^{-24}$ cm^{-3} s^{-1} and $R_{max} = 18$ kpc.

We conclude that a single Gaussian source distribution cannot fully explain the observations of the M51 brightness distribution. While the fit does not match the data for small

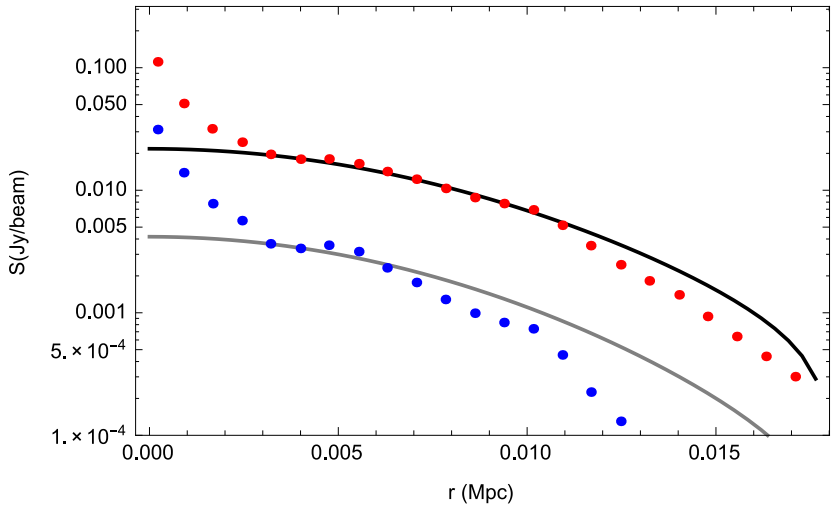

Figure 4.5: Radial Profile fits at 151 MHz and 1.487 GHz with the same parameters as Fig.4.4. The red points are for $\nu = 151$ MHz and the blue points are for $\nu = 1.487$ GHz.

values of r, it does however seem to fit reasonably well for $r > 7$ kpc at $\nu = 151$ MHz. However, at higher frequency, i.e. 1.487 GHz, these parameters do not produce a good fit and seem to over-estimate, indicating a smaller value of r_s. In order to fix this problem we tried changing values of β_μ, d_0 and also the form of magnetic field fluctuation spectrum using the Böhm diffusion (e.g. Berezinsky et al. (1997)). However this did not produce better results. We were able to resolve this problem by means of introducing a double Gaussian source with the tail resembling a single Gaussian at large values of r but with marked differences at smaller values of r.

4.3.2 Improved Model: double Gaussian Source

As indicated in the previous section, a single Gaussian source is insufficient to explain the observational data of M51. In this section we fit the model to the data using a double Gaussian source. A double Gaussian is a superposition of two Gaussian functions of different width and height but centred at the same point. Mathematically, a double Gaussian source has the form:

$$Q_r(r_0) = Q_0 \left[Q_1 \exp\left(-\frac{r_0}{r_{s_1}}\right)^2 + Q_2 \exp\left(-\frac{r_0}{r_{s_2}}\right)^2 \right] \qquad \text{for } r_0 \leq R_{max}. \tag{4.1}$$

Using the above $Q_r(r_0)$, the analytical solution of the diffusion equation is:

$$f(r,\gamma,t) = \int_1^{\gamma_{Max}} d\gamma_0 \quad \frac{Q_0\,\gamma_0^{-\rho}}{|b(\gamma)|}\left[\frac{Q_1\,r_{s_1}^3}{(r_{s_1}^2+4\lambda)^{3/2}}\exp\left(-\frac{r^2}{r_{s_1}^2+4\lambda}\right)\right.$$

$$\left.+\frac{Q_2\,r_{s_2}^3}{(r_{s_2}^2+4\lambda)^{3/2}}\exp\left(-\frac{r^2}{r_{s_2}^2+4\lambda}\right)\right]$$

$$\times\exp\left(-\frac{\tau}{T}\right)\theta(\tau)\theta(t-t_1-\tau)\theta(-t+t_2+\tau). \qquad (4.2)$$

Once more, different values of r_{s_1} and r_{s_2} for the two sources were chosen from a discrete mesh with step size 0.5 kpc and R_{max} was chosen from a mesh with step size 1 kpc. For each value of r_{s_1}, r_{s_2} and R_{max}, Q_1 and Q_2 were optimised numerically to minimise the least squares error with observational data. The fitted model is $R_{max} = 18$ kpc, $r_{s_1} = 0.00005$ Mpc, $r_{s_2} = 0.007$ Mpc , $Q_0 = 1 \times 10^{-22}$ cm^{-3} s^{-1}, $Q_1 = 1.2 \times 10^3$, $Q_2 = 8.75 \times 10^{-4}$. This model fits both the flux data and the observed surface brightness data satisfactorily, as shown in figures 4.6 and 4.7. Notice that where a single Gaussian source could not explain the surface brightness at small values of r, the double Gaussian source can do this. There are still some problems at large values of r for 1.487 GHz, similar to what we saw in the single Gaussian case.

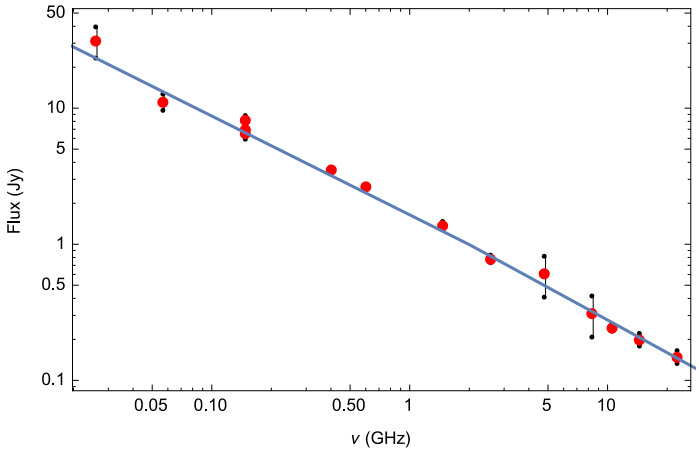

Figure 4.6: Flux density as a function of frequency is obtained from a double Gaussian model, with parameters $R_{max} = 18$ kpc, $r_{s_1} = 0.00005$ Mpc, $r_{s_2} = 0.007$ Mpc, $Q_0 = 1 \times 10^{-22}$ cm^{-3} s^{-1}, $Q_1 = 1.2 \times 10^3$, $Q_2 = 8.75 \times 10^{-4}$.

The above results were obtained using the value of $n_{th} = 10^{-3}$ cm^{-3}. If the bulk of the observed emission is produced in the disk, it is possible that this value of density is small

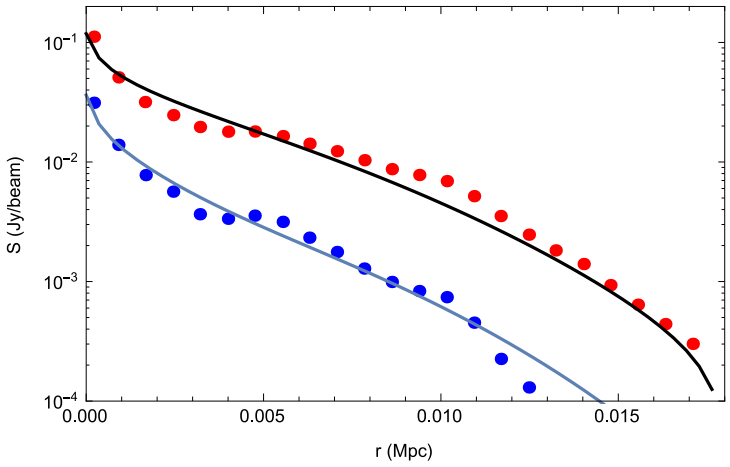

Figure 4.7: A double Gaussian was fitted with parameters in Fig.4.6. This model with a double Gaussian source is able to explain the surface brightness at small values of r. The red points are for $\nu = 151$ MHz and the blue points are at $\nu = 1.487$ GHz.

compared to typical values found in galaxies (e.g. Mulcahy et. al 2014). Therefore to estimate the effect of higher value of thermal density we calculated the emission for $n_{th} = 10^{-1}\text{cm}^{-3}$. The results of surface brightness is presented in the Fig. 4.8. Note that the surface brightness at lower frequency is slightly different compared to the Fig. 4.7, while the surface brightness at higher frequency is similar to that presented in the Fig. 4.7. The change in surface brightness at lower frequency may be due to the effects of Coloumb losses, which are stronger for higher values of thermal density for low-energy electrons.

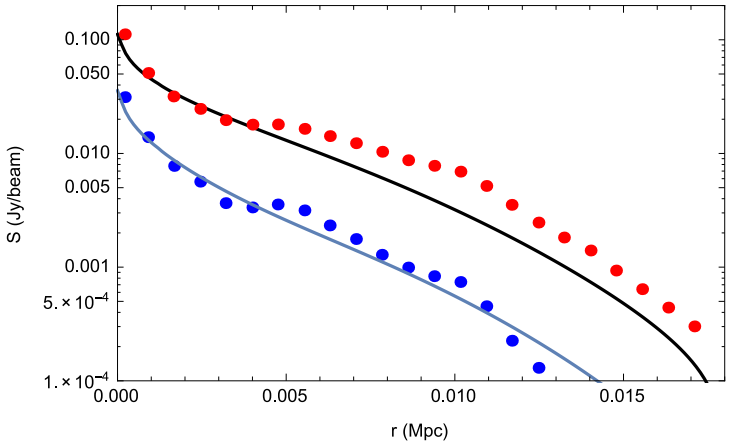

Figure 4.8: Like the Fig. 4.7 for the value of $n_{th} = 10^{-1}\text{cm}^{-3}$.

4.4 Evolution of Radio Emission in the Rest Frame

Having paramaterised the model for both the spectral and spatial properties for the galaxy M51, we will now study the time evolution of these properties. As discussed in the previous section the time parameters in our model were chosen arbitrarily. Therefore it is useful to investigate these properties at different t values with the same values of t_1 and t_2 used in previous section.

We used the paramaterised model that provides a good description of both the spectral and spatial properties, i.e. the double Gaussian distribution in the source term with fitted parameters described in the previous section (see Fig. 4.6), and other parameters based on reference values and observations presented in Table. 4.2. We calculated the evolution of flux spectrum and surface brightness at 151 MHz and 1.487 GHz for different values of t.

Results of the evolution of spectral properties for $t = \{1.5 \times 10^{15}; 2 \times 10^{15}; 5 \times 10^{15}; 1 \times 10^{16}; 1.0 \times 10^{17}; 1.001 \times 10^{17}; 1.01 \times 10^{17}\}$ s are presented in Fig. 4.9. Note that for $t < t_2 = 10^{17}$ s the solution reaches the equilibrium state quickly at higher frequencies. As t approaches t_2 we find that for increasing values of t, the equilibrium state is reached at decreasing values of frequency. Analogous behaviour takes place for $t > t_2$, where the solution leaves the equilibrium state at decreasing values of frequency with increasing values of t.

We also calculated the surface brightness evolution for the same values of time at two different frequencies, i.e. 151 MHz and 1.487 GHz. Note that at lower frequencies for $t < t_2$ the solution reaches the equilibrium state slowly compared to the solutions at higher frequencies. For $t > t_2$ the solution leaves the equilibrium state faster at higher frequencies compared to the solutions at lower frequencies. Interestingly, in this case the smaller component of the surface brightness distribution seems to disappear gradually with time. This effect may be due to the diffusion process. Since electrons are mainly produced at the centre of the source, when the source is no longer active the electrons from the centre are diffused to the extended halo.

4.5 Evolution with Redshift of Spectrum and Surface Brightness

In section 4.3 we studied the spectral and spatial properties of the galaxy M51 by fitting the observed data using a double Gaussian source in our model. Here, we use these properties to study the evolution of M51-like galaxies with redshift. To study these properties at different

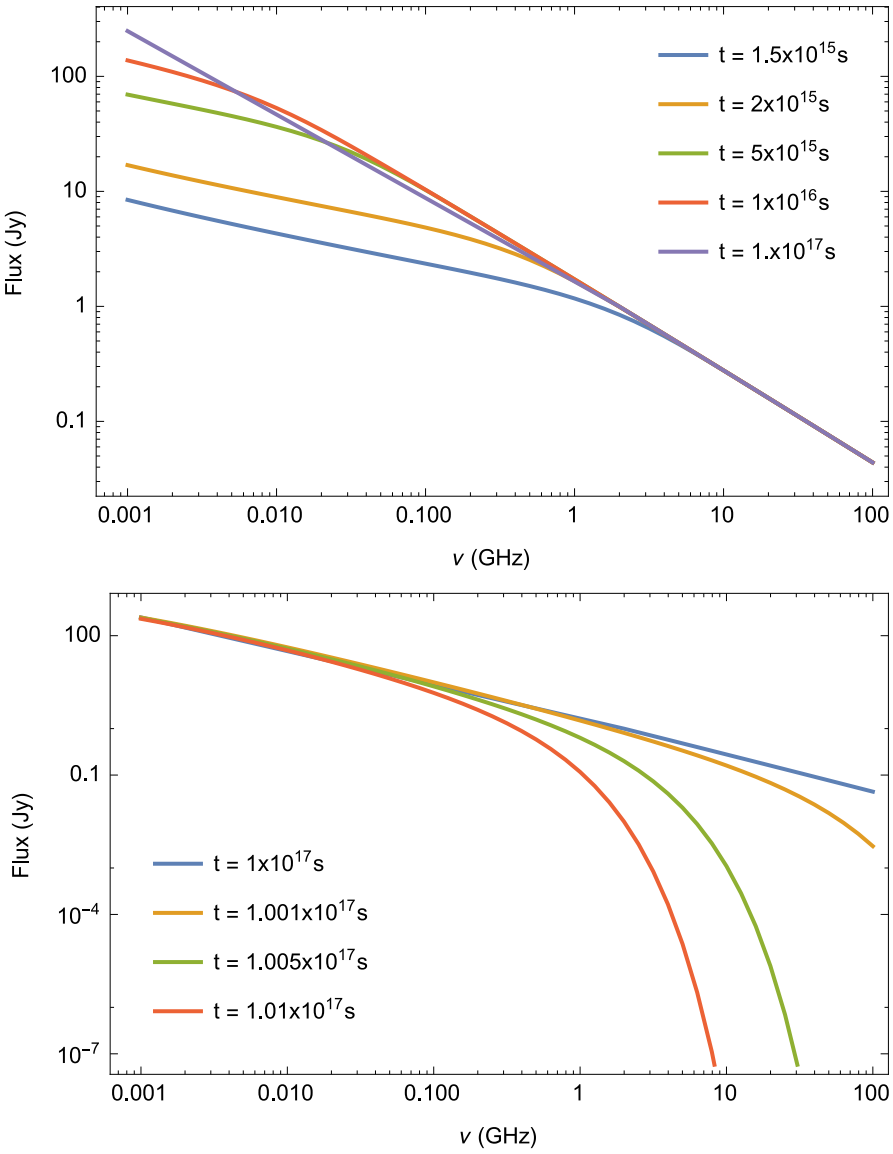

Figure 4.9: Evolution of the radio flux spectrum of M51 in its rest frame. Top figure: the radio flux spectrum calculated for values of $t < t_2$; Bottom figure: the radio flux spectrum calculated for values of $t > t_2$.

redshifts we scale the parameters according to the standard model (see section 1.2). The parameters that are affected by redshifts are r_s, d_0, R_{max}, n_{th}, D_L (see Table 4.3). The scaling laws, with $z_i = 0.0017$ being the reference redshift corresponding to M51 and z the redshift where evolution is calculated, are:

- scaling the value of r_s :

$$r_s = \frac{r_{s_i}}{1+z}(1+z_i)$$

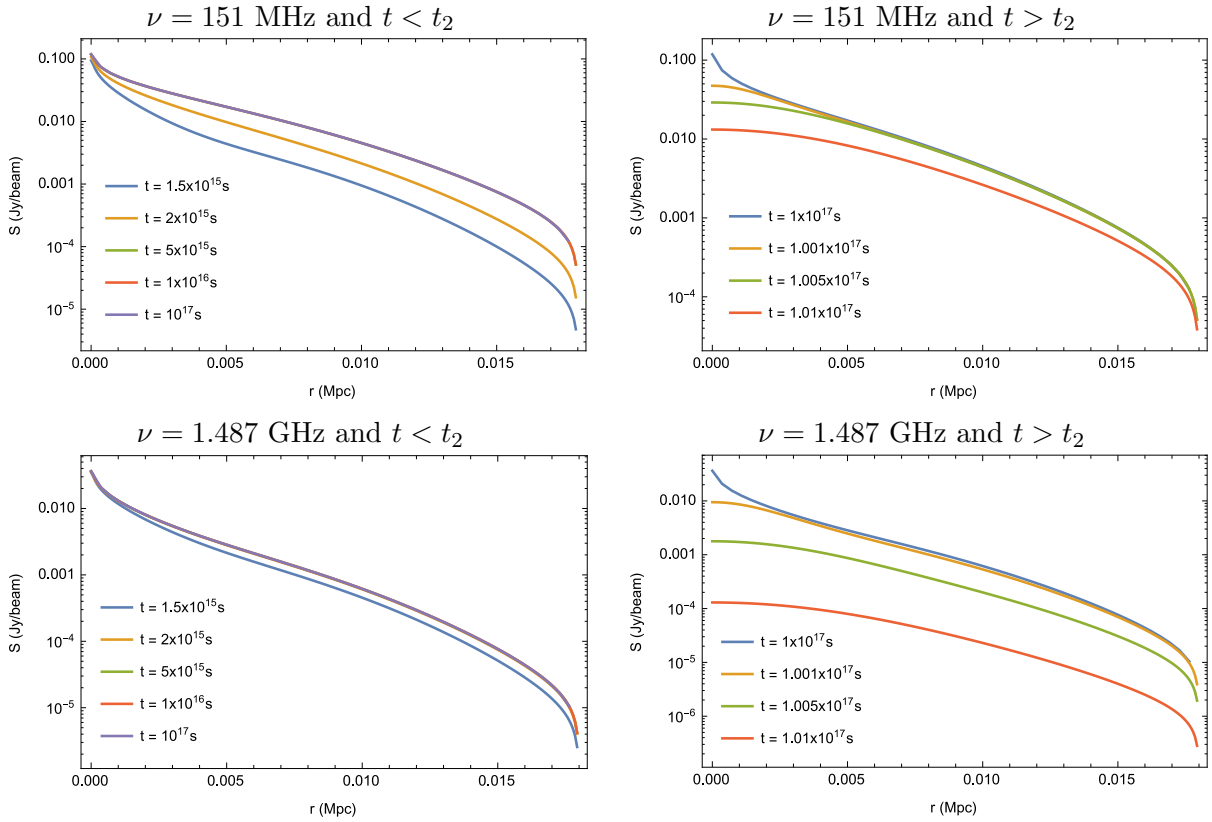

Figure 4.10: Evolution of radio surface brightness for the galaxy M51 in its rest frame at two different frequencies and different times.

- scaling the value of d_0 is dependent only on the minimum scale of the magnetic field fluctuations l. Here $d_0(l) = d_0\, l^{2/3}$, where l is scaled as :

$$l = \frac{l_i}{1+z_i}(1+z)$$

- scaling the value of R_{max} :

$$R_{max} = \frac{R_{max,i}(1+z_i)}{1+z}$$

- scaling values of n_{th} :

$$n_{th} = n_{th,i}(1+z)^3$$

- scaling values of luminosity distance $D_L = (1+z)D_M$, where D_M is the transverse comoving distance that is dependent on the cosmological model (Weinberg, 1972). The

Table 4.3: Scaled parameters with change in redshift.

z	r_{s_1}(Mpc)	r_{s_2} (Mpc)	$d_0(l)$ (cm^2 s^{-1})	$R_{\max}$ (kpc)	n_{th} (cm^{-3})	D_L (Mpc)
0.0001	0.00005	0.007	1.001×10^{28}	18.0288	10^{-3}	0.4
0.0017	0.00005	0.007	1×10^{28}	18	10^{-3}	7.6
0.1	0.0000455	0.00636	9.384×10^{27}	16.3915	1.33×10^{-3}	478.1
0.2	0.0000416	0.00583	8.856×10^{27}	15.0255	1.728×10^{-3}	1016.4

first approximation for small values of z is :

$$D_L = \frac{cz}{H_0}.$$

With the change in redshift, the observational frequencies are also shifted by the following law:

$$\nu_{obs} = \frac{\nu_{emitted}}{1+z}.$$

We assume that the rate of injection does not change with the change in redshift.

We calculated the spectral evolution of M51-like galaxies at redshift values $z = 0.0001$, 0.0017, 0.1, and 0.2. As discussed in the previous section the important quantities for the evolution of the electron spectrum are the time differences between the time t, corresponding to the age of the source, and the times t_1 and t_2. To maintain the validity of the results obtained in the previous section, we scale the values of t_1 and t_2 by setting the value of t to be equal to the age of the universe at the redshift of M51: $z = 0.0017$, fixing $t_2 = t$, and scaling t_1 such that the difference between t_1 and t_2 remains the same as in the previous section.

In Fig.4.11 we present our results for the evolution of the flux density spectrum at different redshifts. Note that at higher redshift the scaling of the flux density spectrum is mainly affected by larger distance while the shape of the spectrum remains the same. This is because at redshifts of 0.1 and 0.2 the time difference between t and t_1 is sufficient to reach equilibrium. At these redshifts the flux density spectrum at around 1 GHz is of the order of 10^{-4} Jy, which will be easily observed by instruments like SKA (Dewdney et al., 2012). At small redshift the flux density spectrum is higher due to shorter distance. At this redshift we can see a steepening of the radio spectrum at high frequencies. This is because at this redshift the injection of electrons has ended (i.e the time at this redshift is greater than t_2) and in the higher energy part of the electron spectrum there is a large decrease due to energy losses (see sections 3.5 – 3.6).

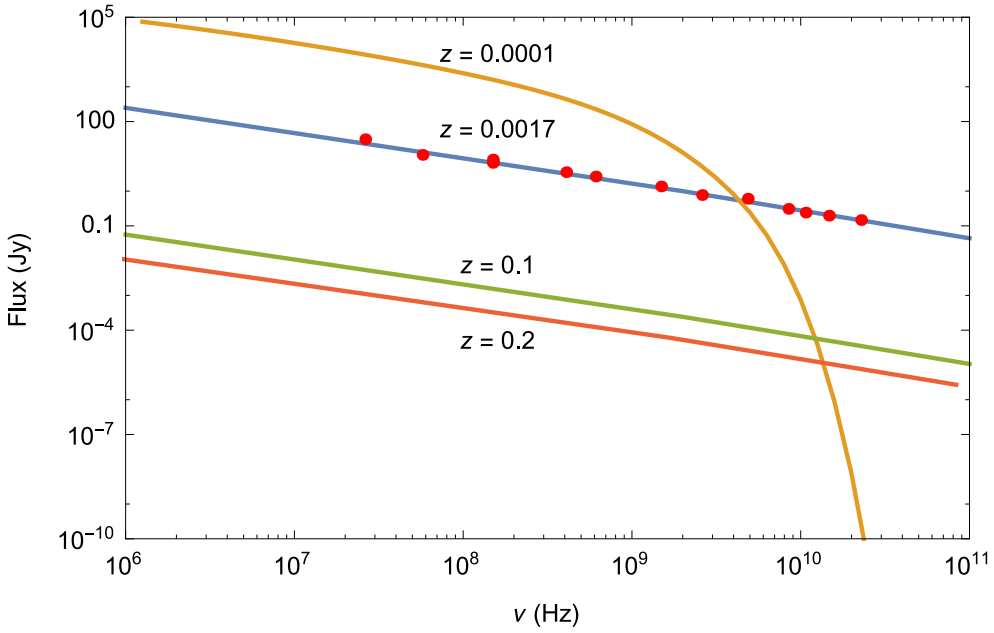

Figure 4.11: Evolution of Flux Density at varying values of redshift.

We present in Fig.4.12 the evolution of surface brightness at two frequencies for three redshifts. In this case the effects of distance are not present as the surface brightness is not dependent on distance (see Appendix A). The residual difference between different redshifts is due to the scaling of parameters related to the source, i.e. size of the source. As a result the surface brightness at smaller redshift is extended further compared to the surface brightness at higher redshift. Also, the normalisation of the surface brightness curve is larger at smaller redshift due to the larger size of the source along the line of sight.

4.6 Discussion

In this chapter we applied our model to the radio halo of the galaxy M51 and found that the flux spectrum can be reproduced with only two free parameters in the source term: r_s and Q_0. Other parameters in the model were given reasonable values based on simplifying assumptions and observations: d_0, T, n_{th}, $\beta_m u$ and ρ (see Fig. 4.4).

While the model with a single Gaussian source is able to fit the observed flux data, it fails to fit the surface brightness data in the internal part of the curve. We found that by using a double Gaussian source in our model we were able to fit the surface brightness data at all radii reasonably well at both 151 MHz and 1.487 GHz. This is a promising result for a simple model that assumes spherical symmetry of the source and a constant magnetic field inside

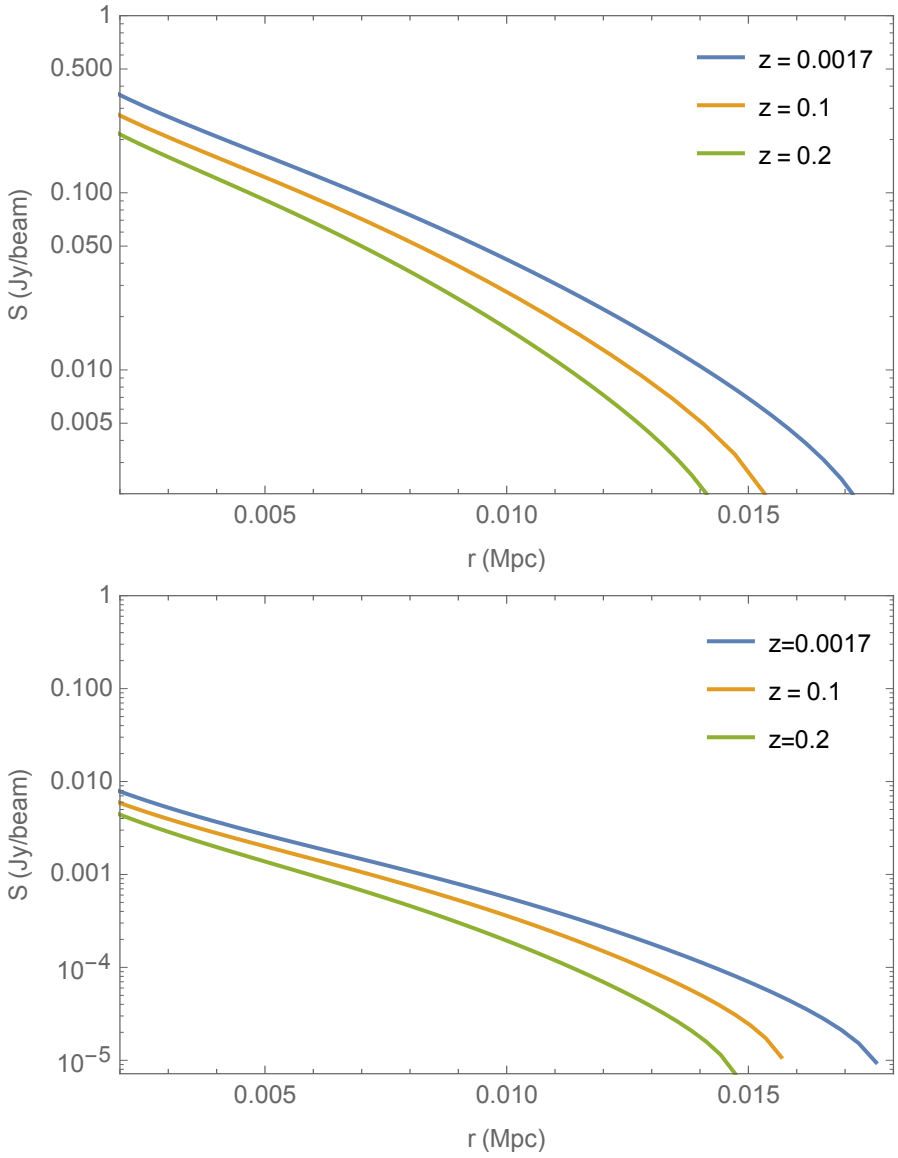

Figure 4.12: Evolution of surface brightness at 151MHz on the left and at 1.487 GHz on the right, measured at different redshift.

the source.

A possible physical mechanism leading to a double Gaussian source is the production of electrons from two different sources having different injection rates and spatial distributions. In section 4.2 we mentioned the presence of a Seyfert-like nucleus and starburst activities in M51. It is possible that the Seyfert-like nucleus is the source of the smaller component and the starburst activities are a source of the larger component, with the sum of these two effects being well described by a double Gaussian distribution.

Using the fitted double Gaussian model we studied the evolution of radio halo properties in the rest frame of M51. We found that the solution of the flux spectrum reaches equilibrium state (at a value of $t < t_2$) and leaves the equilibrium state (when $t > t_2$) quickly at higher frequencies, which is in accordance with the behaviour of electron spectra presented in chapter 3. Similarly these effects can be seen in the plots of surface brightness. For $t > t_2$ the effect of the smaller component of the surface brightness distribution appears to disappear with increasing time. We believe that this may be because of diffusion, as the electrons are diffused away from the centre when the source is no longer emitting electrons.

We calculated the evolution of radio halo properties at different redshifts and found that at redshifts 0.1 and 0.2 the time difference between the beginning of electron injection and measurement time is sufficient to reach an equilibrium state and as a result the shape of the spectrum remains the same. The only difference in the spectrum at high redshift is that it has smaller values due to increasing distance. At lower redshift we found a steepening in the spectrum at high frequencies due to the steepening of the electron spectrum caused by energy losses after the end of injection. In the case of surface brightness we found that the effect of distances is not important but the change in surface brightness is a result of scaling the halo size with redshift. With instruments like SKA we will be able to observe M51-like galaxies at redshifts 0.2 and more and from these observation derive the epoch when the injection of electrons begins and ends.

We also note that, since M51 is a face-on spiral galaxy, a full study of its radio halo would require an observation of the radial distribution of the radio emission in a direction perpendicular to the disk in order to disentangle the contribution from the halo and the disk. Since this is obviously not possible, it will be important to extend the study presented in this chapter to other galaxies halos also in edge-on galaxies, like NGC 891 and NGC 4631 (Dahlem et al., 1995), NGC 4945 (Elmouttie et al., 1997), NGC 4666 (Dahlem et al., 1997) and NGC 253 (Heesen et al., 2009). To consider these cases, it will be necessary to extend our formalism to the case of a not-spherically symmetric source term. This is necessary to account for the elongated shape of the radio emission usually found in these galaxies and for different mechanism of injection of electrons in the halos, like the well-known super-wind observed in the last case. Very interestingly, in most of these galaxies it appears that the radial shape of the radio emission changes with the radius. Also the spectrum of the radio emission presents different spectral indices in the overall halo and in the central part. This suggests a possibility that a source term has at least two different components, as found for the double Gaussian term in M51.

Now that we have demonstrated that our model is able to reproduce spectral, spatial and

temporal properties for a single galaxy radio halo, we will apply this model to the population of galaxies residing within a cluster to study its global radio halo as a combination of several radio galaxy halos. In the next chapter we discuss how this model is applied to a cluster of galaxies.

Chapter 5

Modelling Clusters of Galaxies

"All the mathematical sciences are founded on relations between physical laws and laws of numbers, so that the aim of exact science is to reduce the problems of nature to the determination of quantities by operations with numbers."

-James C. Maxwell

5.1 Introduction

In this chapter we will explore our proposed theory that the radio halos observed in clusters are the results of summing galaxy radio halos in the galaxies of these clusters. We will use this theory to describe the overall morphology of radio halos in clusters. In chapter 3 we described the diffusion model for relativistic electrons and in chapter 4 we applied this model to the galaxy M51. We calculated the spatial, spectral and temporal distributions of radio emission from M51 and found that our model is good at describing these properties. We now turn our attention to applying this diffusion model to calculate the properties of a radio halo in a galaxy cluster.

We begin in section 5.2 by describing the mathematical framework necessary to apply our model to a cluster. In section 5.3 we consider several sources in a cluster with same time window (the time period between the beginning and ending of injection). We calculate the resulting surface brightness map of the cluster and study its evolution over time. We then refine the model by changing the time window for each source independently and studying the evolution of the cluster halo. By allowing the time windows for sources in the cluster to be different from each other we are able to study the morphology of radio cluster halos and their evolution. We apply this model to the cluster CL1446+26 to study its surface brightness distribution in section 5.4 and we fit our model to the observed data. We study the

morphology of cluster halos with an increasing number of sources in section 5.5 by calculating surface brightness and spectral properties. Finally we conclude this chapter with a discussion of our results and describe possible improvements to our model.

5.2 Diffusion Equation with Many Sources

In this section we describe the mathematical framework necessary for modelling the radio emission from a cluster. In the previous chapter we presented a model that takes into account a single source and were able to use that model to fit the observed data of M51. We proposed in section 2.6 that the diffuse radio emission from a cluster of galaxies is the superimposed emission of the sources present in a cluster. Hence we need to define a model that takes into account many sources. In modifying our single-source model to account for multiple sources, it is instructive to revisit the diffusion equation governing the density distribution of electrons in presence of many sources:

$$\frac{\partial f(\mathbf{r},\gamma,t)}{\partial t} - D(\gamma)\Delta f(\mathbf{r},\gamma,t) + \frac{\partial}{\partial \gamma}[b(\gamma)f(\mathbf{r},\gamma,t)] + \frac{f(\mathbf{r},\gamma,t)}{T} = \Sigma_i a_i Q_i(\mathbf{r},\gamma,t)\ . \tag{5.1}$$

Since the diffusion equation presented above is a linear equation, the solution of the equation is simply given by:

$$f(\mathbf{r},\gamma,t) = \Sigma_i a_i f_i(\mathbf{r},\gamma,t) \tag{5.2}$$

where $f_i(\mathbf{r},\gamma,t)$ is the solution of the diffusion equation for the source $Q_i(\mathbf{r},\gamma,t)$. The terms Q_i represent sources with similar properties located at different positions in a galaxy cluster. Just as before the source terms are expressed in terms of the injection rate of particles as a function of position, energy and time.

When studying the extended emission of radio halos in galaxy clusters we are interested mainly in the extended part of each single halo. Therefore in the model with many sources we will be using a single Gaussian distribution to describe the spatial distribution of each source and not a double Gaussian as in the case of M51. This is because the single Gaussian model was able to match the surface brightness accurately in the extended part.

Once the electron density solutions for all of the sources are obtained we use these solutions to calculate the radio spectral and spatial properties of these sources by calculating

synchrotron emission as described in Appendix A. Since the diffusion equation is linear, the overall density is a sum of densities as presented above, and this sum can be interchanged with the integral in the calculation of surface brightness, so that the total surface brightness at a point is simply the sum of surface brightness contributions from each source at that point. Therefore the solutions for spectra and surface brightness of sources can be summed to obtain the solution for a cluster.

5.3 Studying the Morphology of Cluster Halos

The model described above for many sources is used to study the overall shape of the halo produced by summing the surface brightness distributions of all the sources within the cluster. We consider two cases: in the first case we assign the same properties to all of the sources within the cluster and study the evolution of surface brightness distribution as a function of time; and in the second case we assign the same spatial and spectral distributions to each source within the cluster but we vary the time at which injection begins and ends for each source (i.e. time window) and study the evolution of the surface brightness distribution of the cluster as a whole over time.

5.3.1 Sources with Equal Time Windows

Here we present the first case for a cluster with all sources having the same properties. We have applied this model to 9 sources with positions that are similar to those of radio sources in cluster CL1446+26 (see section 5.4 for more specific analysis of this cluster). Here we assume all the sources start to inject electrons at time t_1 and stop injecting at time t_2. Surface brightness profiles of all these sources are calculated at various times t with the use of parameters listed in Table 5.1.

We are using the same reference values used for the case of M51 for these parameters: n_{th}, d_0, T and γ_{max}. The value of the magnetic field was chosen to be $\beta_\mu = 1\,\mu$G because this is a typical value of the magnetic field in the ICM (see section 2.3). The value of Q_0 is a reference value and it is the same order of magnitude found in the case of M51. The reference value for the parameter ρ is in the range of values usually found for cosmic rays in galaxies and clusters of galaxies (Schlickeiser, 2001). The luminosity distance D_L refers to a typical value of rich and nearby clusters, for e.g. Coma. Since we are mainly interested in the overall radio morphology of a cluster we choose this value which entails a large angular size, in order to obtain detailed properties of diffuse radio emission. For r_s we choose a value of 0.3 Mpc

Table 5.1: Parameters used to obtain radial distribution of sources.

Symbol	β_μ	n_{th}	d_0	R_{max}	γ_{max}
Value	1μG	10^{-3} cm^{-3}	10^{28} cm^{2}s^{-1}	5 Mpc	10^7
Symbol	r_s	D_L	T	Q_0	ρ
Value	0.3 Mpc	100 Mpc	10^{20} s	10^{-23} cm^{-3} s^{-1}	2.4

because we have found that generally it is of the order of the extended diffuse emission size of sub-regions in radio halos (see Fig. 2.6). Note that this is a large value compared to the value used for M51 but since we are considering a small number of sources we can assume in this early version of the model that it refers to a concentration of galaxies and not a single galaxy. The value of $R_{max} = 5$ Mpc was chosen to allow electrons to diffuse on a large scale. This value is also large in comparison with the typical size of radio halos, however this value of R_{max} is much bigger than the value of r_s hence its specific value in this case is not very important.

We studied the cluster surface brightness using the time window $t_1 = 10^{15}$s and $t_2 = 10^{16}$s for all the sources. We obtained the results at $t > t_1$, $t = t_2$, and for $t > t_2$. The surface brightness maps are presented in the Fig. 5.1. It is clear from this figure that the overall distribution shape of sources remains the same for all t values, however as t goes from t_1 to t_2 there is a gradual increase in brightness and after the time t_2 the surface brightness starts to decrease as the source is no longer emitting electrons.

5.3.2 Sources with Different Time Windows

When all the sources are active for the same period, it is clear that the overall morphology of the spatial distribution maintains the same shape during the evolution of the cluster. Therefore in what follows, different time windows are chosen arbitrarily for each source, keeping all the other parameters the same. The positions of the sources are presented in Fig. 5.2 (first image) and the corresponding time windows are presented in the Table 5.2.

We calculated the total surface brightness of the cluster at different values of time. Contour plots of surface brightness for these time values are presented to investigate the evolution of morphology of the cluster (see Fig.5.2). The values of t are chosen as such to illustrate the change in morphology of a cluster when some of the sources are active while others are not.

It is clear from the figure that the morphology of the surface brightness distribution changes as time is varied. Notice that at certain times it exhibits features that are very

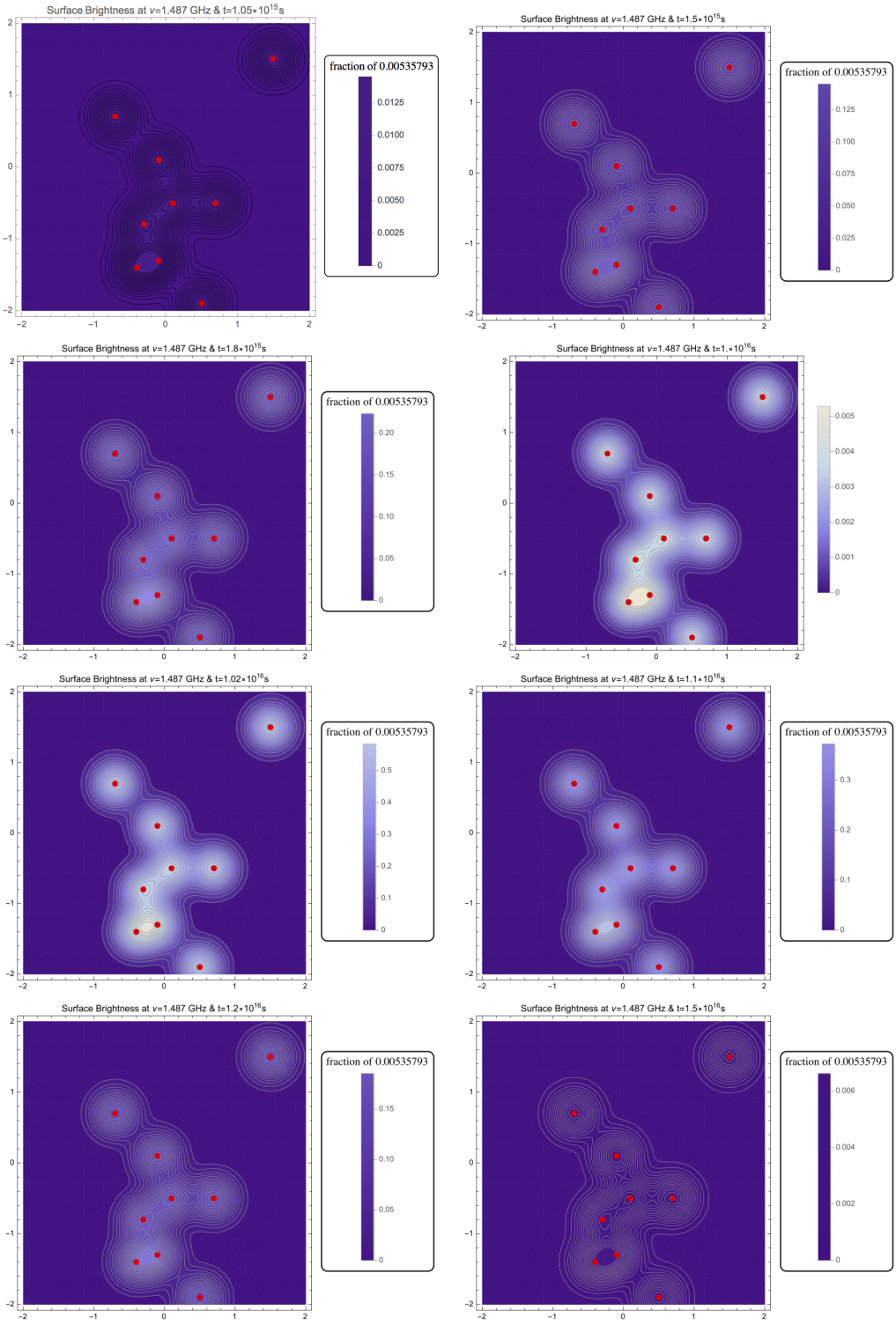

Figure 5.1: The evolution of cluster surface brightness maps when all nine sources have the same properties. It is clear that the overall radial distribution remains the same over time and the surface brightness increases for $t_1 < t < t_2$ and starts dropping for $t > t_2$.

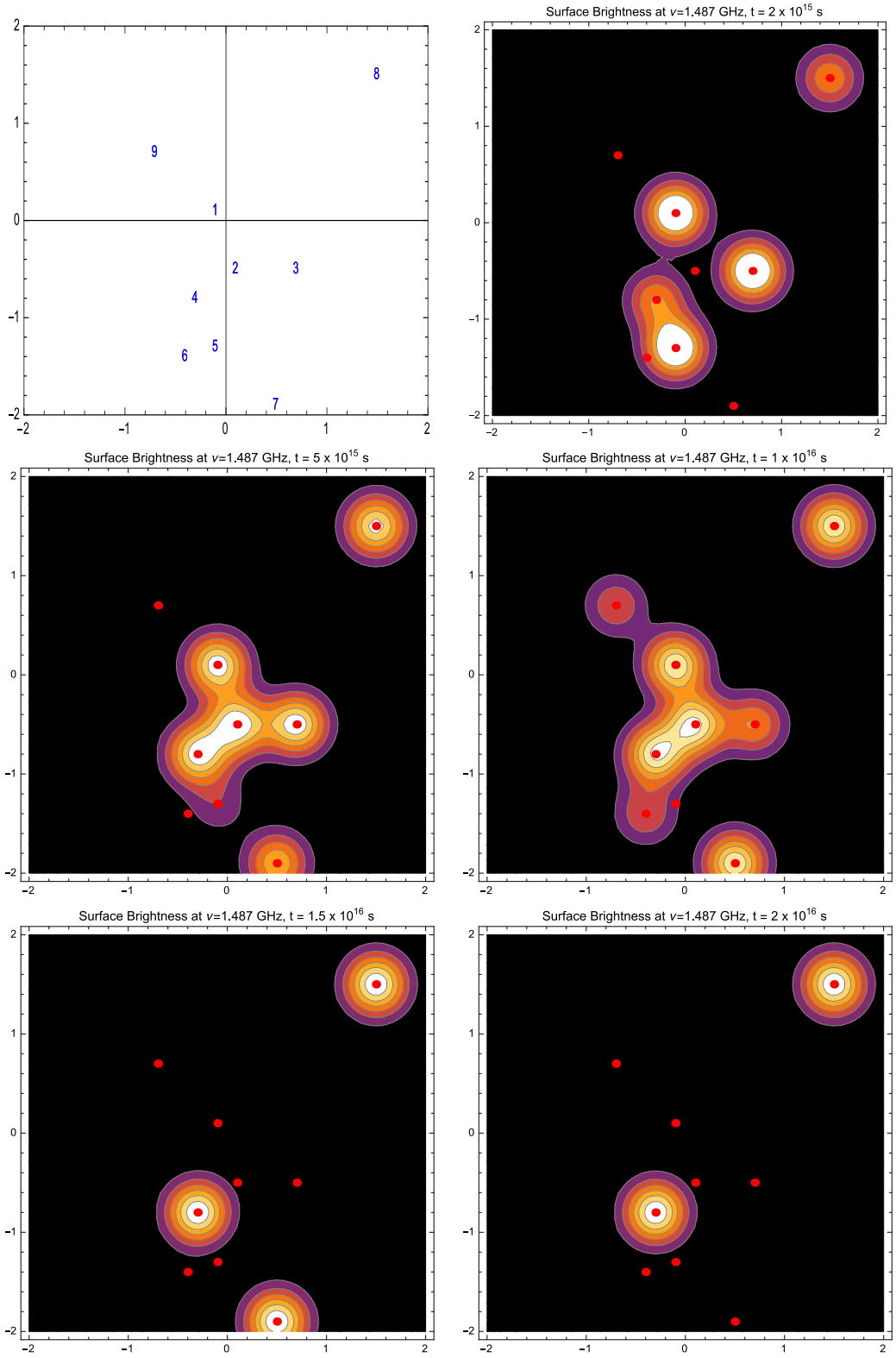

Figure 5.2: The evolution of the cluster surface brightness radio map at 1.4 GHz for various values of time is presented from left to right for increasing values of t. These sources were assigned t_1 and t_2 values as in Table 5.2 while keeping all the other parameters same among different sources.

Table 5.2: Assignments of time windows to the sources positioned as in the first image of Fig. 5.2.

Position	$\mathbf{t_1}$	$\mathbf{t_2}$
1	1×10^{15}s	1.1×10^{16}s
2	1.05×10^{15}s	1.02×10^{16}s
3	1×10^{15}s	9×10^{15}s
4	1.5×10^{15}s	2×10^{16}s
5	1×10^{15}s	3×10^{15}s
6	9×10^{15}s	$1.1 \times 10^{16}s$
7	3×10^{15}s	$1.5 \times 10^{16}s$
8	1.5×10^{15}s	2×10^{16}s
9	9×10^{15}s	$1.1 \times 10^{16}s$

similar to observed clusters. In particular for our chosen values at $t = 1 \times 10^{16}$ s the shape of the distribution appears to be similar to the shape of the cluster CL1446+26 (see Fig. 5.3). This similarity in shape is obtained using a simplified version of our model where the positions of the sources were approximated by looking at the radio maps. In the next section we apply our model to the cluster CL1446+26 by obtaining the positions of the sources in a more accurate way.

5.4 Application of the model to the cluster CL1446+26

In the previous section we have seen that our model with many sources is capable of producing similar features to observed radio halos in clusters. We now apply this model to a particular cluster, CL1446+26, to compare the results with the observed radio emission.

CL1446+26 is a rich cluster located at the redshift 0.37 (Dressler et al., 1997) which corresponds to luminosity distance of 2050 Mpc in the present cosmological model. The cluster appears to be quite luminous in X-rays with luminosity 3.41×10^{44} erg/s in the 0.1 – 2.4 keV band (Wu et al., 1999). When comparing the X-ray luminosity with the radio luminosity this cluster appears to be more luminous in radio ($P_{1.4} = 3.57 \times 10^{24}$ W Hz^{-1} for halo and 2.46×10^{24} W Hz^{-1} for the possible relic) compared to other clusters with same luminosity in X-ray, as we can see in the $P_{1.4} - L_x$ plot in Fig.2.10. Also, this cluster has complex morphology in X-Ray and optical bands and there is no clear spherical symmetry in X-ray emission (see Fig. 5.3).

The cluster CL1446+26 has been studied in radio by Owen et. al (1999), Giovannini et al. (2009) and Govoni et al. (2012). Giovaninni et al. (2009) and Govoni et al. (2012) both

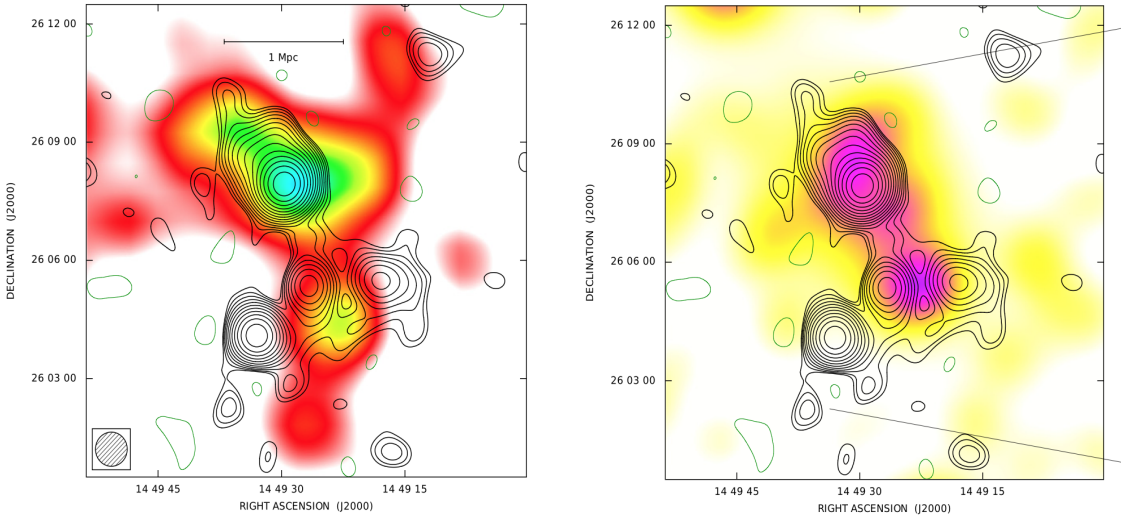

Figure 5.3: Left: radio contours taken with VLA for CL1446+26 are overlaid onto the X-ray image by ROSAT PSPC. Right: radio contours overlaid onto isodensity map of likely cluster members (Govoni et. al 2012).

observed the cluster using Very Large Array (VLA) but in different configurations, C and D respectively. Giovannini et al. suggested the presence of a relic in the northern part of the cluster but when it was observed at low resolution by Govoni et al. a larger extended emission was detected and it was concluded that this extended emission may correspond to a central halo. Govoni et al. also detected an elongated diffuse emission in the southern part of the cluster and attributed this emission to a possible relic. They also detected a weak connection between the radio halo and the possible relic and therefore they suggested that deeper observations of this cluster are necessary in order to determine the nature of this diffuse emission.

Govoni et al. (2012) presented a low-resolution radio contour map at 1.4 GHz of CL1446+26 overlaid on the isodensity map of likely cluster members and on the X-ray maps (See Fig.5.3). These authors noted that the overall diffuse radio emission seems to follow the galaxy distribution more closely than the intra cluster gas distribution. We note that the morphology of the radio and X-ray maps appear to be different because the peaks of the emission in these distributions are not in exactly the same place and the overall distributions are elongated in different directions (see also the discussion in section 2.5). We chose this cluster to test our model because we expect that the radio distribution in our model follows the optical galaxy distribution more than the intra cluster gas distribution as discussed in section 2.6.

As a first step we obtained the positions of the main radio sources in the map. We then assigned a source at each of these positions by writing the source term in the diffusion equation

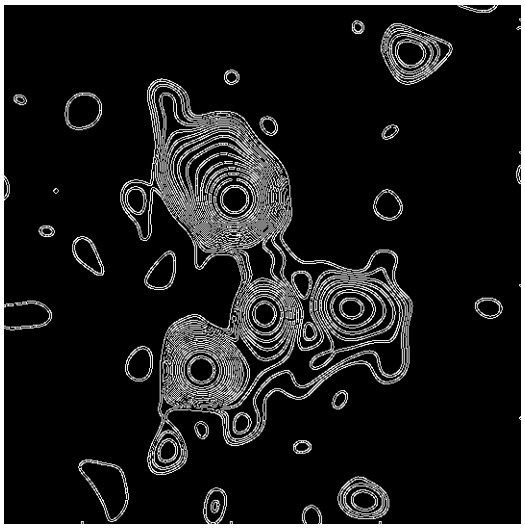

Figure 5.4: Radio Contours extracted from Fig.5.3.

as a linear combination of single source terms centred at these positions. We then assigned different time windows to each of these sources by keeping all the other parameters same as in the previous section (see Table 5.1) and only changing the luminosity distance to the real distance value of this cluster (i.e. $D_L = 2050.4$ Mpc). Using the mathematical framework described in section 5.2 we calculated the radio map and total flux spectrum of this cluster.

In order to accomplish our first step the radio emission from Fig.5.3 was extracted using image processing techniques, such as channel separation and edge detection. Once the contours were extracted (See Fig.5.4), the positions of the sources within the cluster were noted and converted to Mpc scale. The time windows were then chosen to be similar to those presented in Table 5.2, as the overall shape of the radio morphology obtained in the previous section was similar to the observed radio emission. The positions of the sources are presented in Fig. 5.5 and their respective time windows in Table 5.3.

Following the procedure described in the previous section, we calculated the cluster radio emission at $t = 1 \times 10^{16}$ s. According to the results presented in the previous section, at this value of time the calculated shape of the surface brightness radio map was most similar to the observed one and therefore we chose this value.

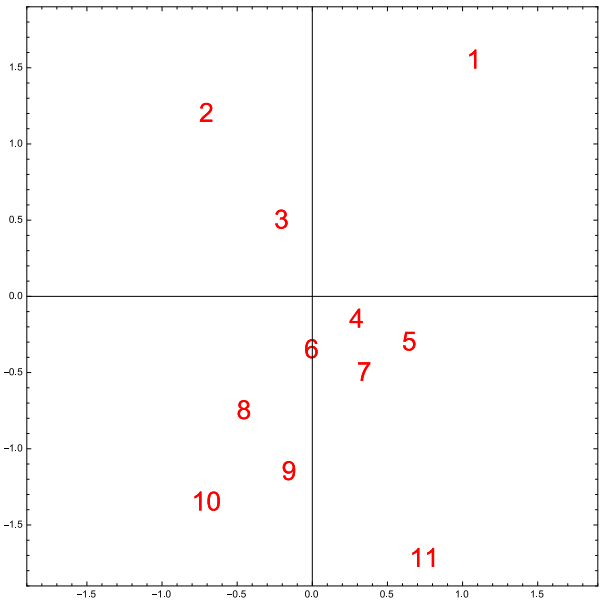

Figure 5.5: Positions of the sources.

Position	t_1	t_2
1	1.05×10^{15}s	1.02×10^{16}s
2	9.00×10^{15}s	1.10×10^{16}s
3	1.50×10^{15}s	2.00×10^{16}s
4	1.00×10^{15}s	3.00×10^{15}s
5	1.50×10^{15}s	2.00×10^{16}s
6	1.05×10^{15}s	1.02×10^{16}s
7	1.00×10^{15}s	3.00×10^{15}s
8	1.05×10^{15}s	1.02×10^{16}s
9	9.00×10^{15}s	1.10×10^{16}s
10	9.00×10^{15}s	1.10×10^{16}s
11	9.00×10^{15}s	1.10×10^{16}s

Table 5.3: Assigned time windows to the positions

We present the results of our calculations in Fig.5.6. To compare our results with the observed radio emission we overlaid the observed radio contours on the calculated radio emission. Looking at this figure it is clear that the morphology of the calculated radio emission is very similar to the observed one.

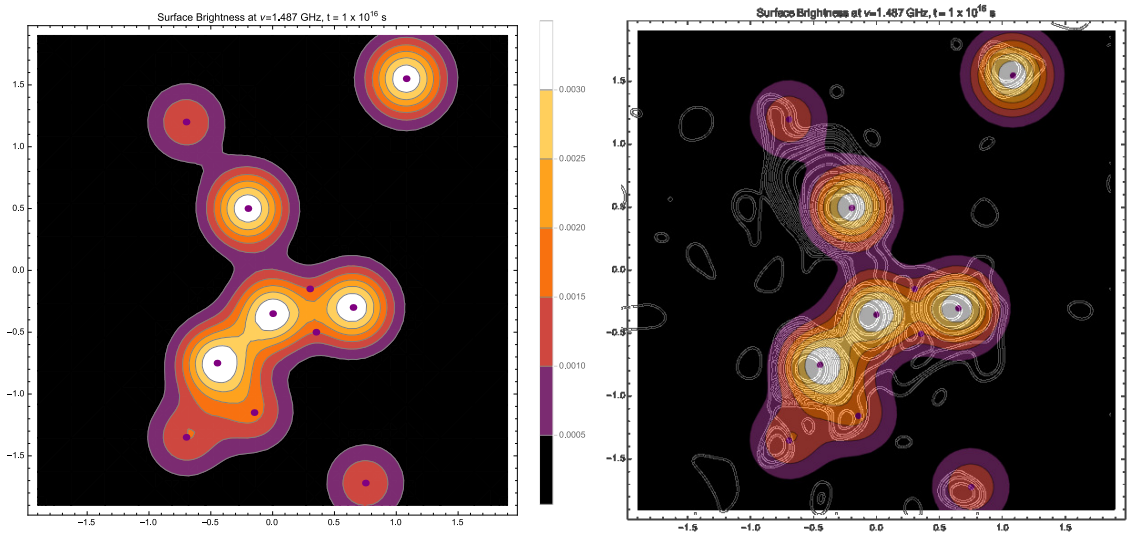

Figure 5.6: Left: surface brightness contours of CL1446+26 obtained using the model above with the parameters in Tables 5.1 and 5.3. Right: the observed radio emission contours overlaid on the distribution of surface brightness calculated by our model. All the maps in this chapter have scale presented by the colour legend is in the units of Jy/arcmin^2.

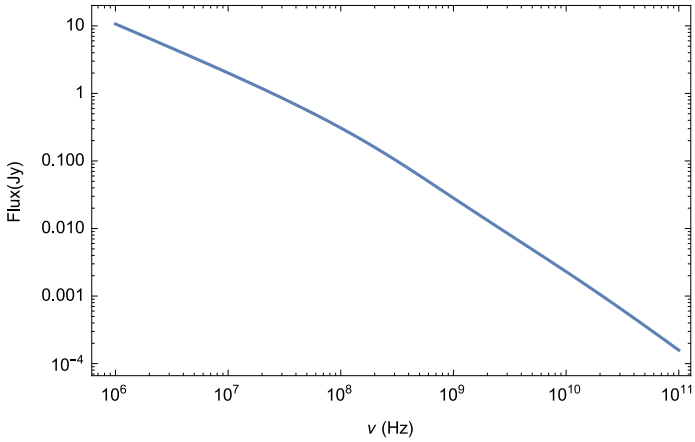

Figure 5.7: Total flux from 11 sources in CL1446+26.

We also calculated the total radio flux predicted by our model over a wide range of frequencies. To derive this flux we followed the same procedure described above: we calculated the flux for each source and then summed all the flux values at each point to obtain the total flux of the cluster. We present the results of this procedure in Fig. 5.7. The shape of the predicted flux spectrum changes at approximately 100 MHz. A similar change in slope is observed in some galaxy clusters (e.g. Thierbach et al. (2003), for the case of Coma). The frequency where the change in slope of the flux spectrum takes place is dependent on the choice of time window for each source within the cluster. In our model we predict the value of flux at 1.4 GHz to be of the order 18 mJy, which is similar to the value measured by Govoni et al. (2012), where by summing the values for the radio halo (7.7 ± 2.6 mJy) and the radio relic (5.3 ± 1.2 mJy) the value of 13.0 ± 2.9 mJy is obtained. We sum these values because we predict the full radio emission coming from all the regions observed by Govoni et al. (2012) including the regions classified as halo and relic. We are able to obtain this value of flux by simply scaling the value of Q_0 by a factor of 0.7. This result of our model is very promising as we are able to reproduce the observed flux for the galaxy cluster with the value of Q_0 that is very similar to the value obtained for M51 (see section 4.3).

Since our model is able to predict the shape of the radio map in CL1446+26, in the next section we test if our model can reproduce the shape of radio maps for other clusters by changing the number of sources. We also predict the flux spectrum for these cases.

5.5 Application of the model for a large number of sources

As we have seen in the previous section our model provides an explanation for the hypothesis that the overall radio emission of a cluster closely follows the distribution of galaxies within the cluster. This model can be applied to any cluster by changing the number of sources. To investigate the morphology of the total emission of other clusters, this model was further used for 20, 50, 80 and 100 sources within a cluster. In the case of 20 sources, five different time windows were used to describe different sources. The time windows were randomly chosen from Table 5.3. Sources in a cluster were randomly distributed on a disk of radius 2 Mpc with random distribution of time frames. All the parameters used are listed in Table 5.1 and the results are presented in Fig. 5.8.

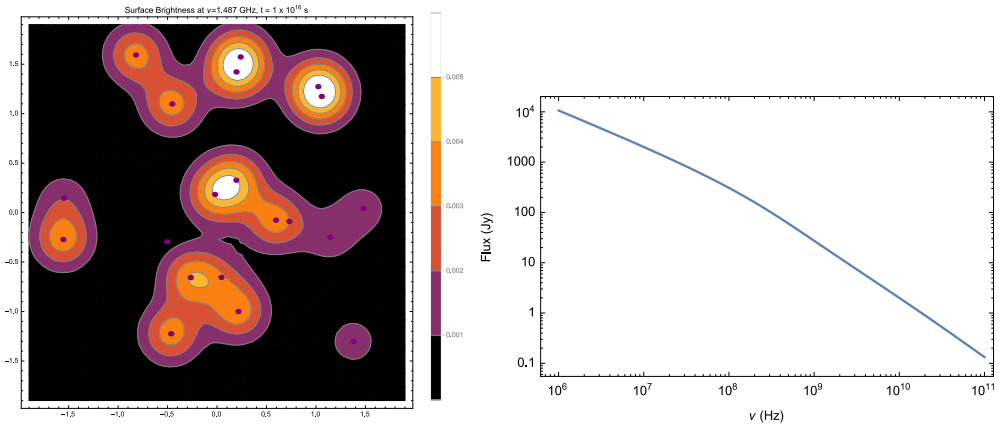

Figure 5.8: Left: 20 randomly distributed sources on a disk with randomly assigned time windows chosen from Table 5.3. This morphology of the cluster is at $t = 1 \times 10^{16}$s. The size of the box is $\approx$ 4Mpc. Right: the total flux from 20 sources within the cluster.

We also consider the cases with 50, 80 and 100 sources with the same assumptions as in the case of 20 sources. Again in these cases time windows for the sources are chosen randomly from Table5.3. The results for these cases are presented in the Fig. 5.9 for 50 sources and Fig. 5.10 for 80 sources. In the same figures we also present the total flux for each case.

As we increase the number of sources in a cluster the overall shape appears to become more extended and eventually quite regular. This effect is due to the mixing of diffusing electrons generated by these sources in the ICM. With a high number of sources the average distance between each of them is small and this makes it possible for electrons to mix more easily. As a consequence we expect that by increasing the number of sources we obtain more extended and regular radio maps.

Similar to the case of the cluster CL1446+26 we see that there is also a change in slope

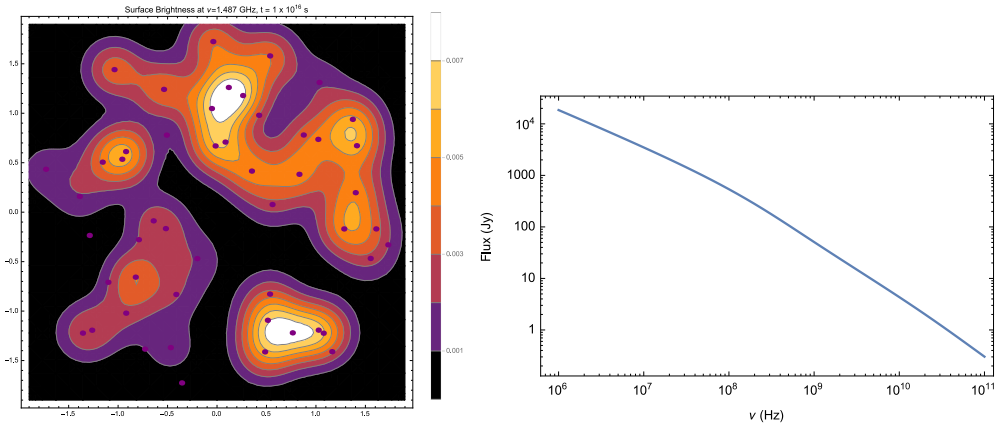

Figure 5.9: Left: 50 randomly distributed sources on a disk with randomly assigned time windows chosen from Table 5.3. This morphology of the cluster is at $t = 1 \times 10^{16}$s. The size of the box is $\approx$ 4Mpc. Right: the total flux from 50 sources within the cluster.

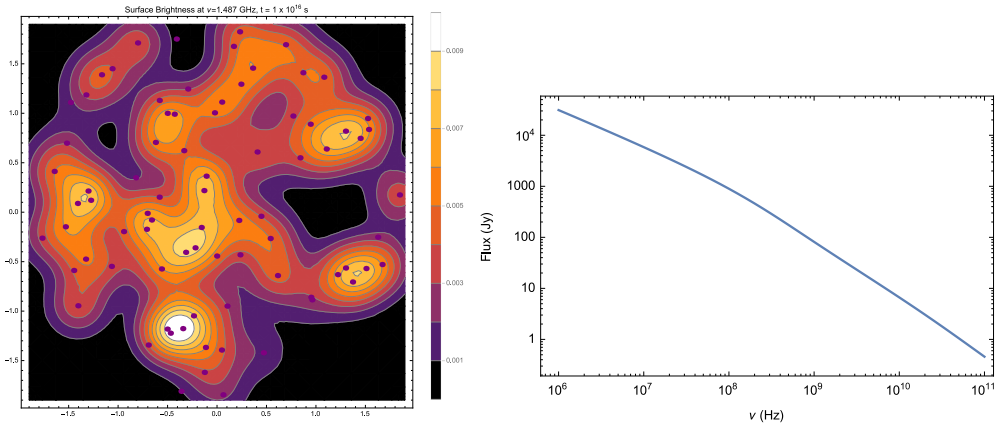

Figure 5.10: Left: 80 randomly distributed sources on a disk with randomly assigned time windows chosen from Table 5.3. This morphology of the cluster is at $t = 1 \times 10^{16}$s. The size of the box is $\approx$ 4Mpc. Right: the total flux from 80 sources within the cluster.

of flux spectrum for a large number of sources at approximately the same frequency. This may be due to the fact that we are using the same time windows as in the case of the cluster CL1446+26. Now comparing the intensity of the total flux for an increasing number of sources we see that the change is almost linear (see Fig. 5.12). Note that this correlation is not perfectly linear because the ratio between the active and inactive sources is not the same for different cases due to the random choices of time windows. This correlation is an important result of our model as it predicts that an increase in the number of sources increases the radio luminosity linearly. Since the number of galaxies is correlated with the mass of the cluster, we expect that the correlation between the radio luminosity and the mass is quite strong, while with other quantities like the X-ray luminosity we can expect a correlation with

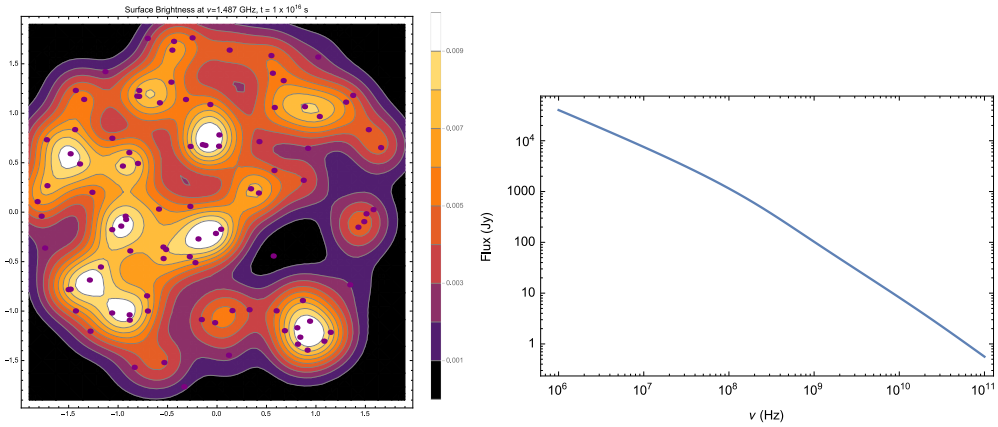

Figure 5.11: Left: 100 randomly distributed sources on a disk with randomly assigned time windows chosen from Table 5.3. This morphology of the cluster is at $t = 1 \times 10^{16}$s. The size of the box is $\approx$ 4Mpc. Right: the total flux from 100 sources within the cluster.

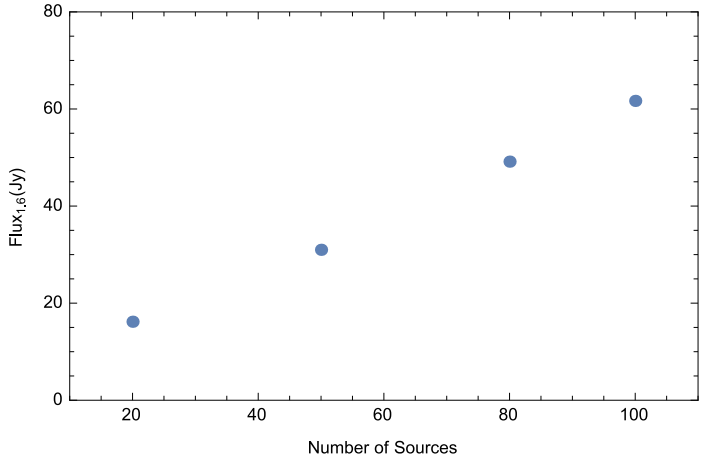

Figure 5.12: Total flux at 1.6 GHz predicted by our model as a function of number of sources within a cluster.

a bigger scatter because in our model the radio luminosity is not strictly correlated with the ICM temperature. This is in accordance with the observed scaling relations in galaxy clusters that show strong correlation of radio luminosity with mass (Govoni et al., 2001b), and a more scattered correlation with the X-ray luminosity (Govoni et al., 2012) and temperature (Liang et al., 2000). Also note that the predicted intensity of flux is high compared to the usual observed values in galaxy clusters (usually of the order 1 Jy or less) but we can adjust these values by scaling Q_0 and considering that most of the clusters are located at a further distance than 100 Mpc.

5.6 Discussion

The previous sections have shown clearly that our model is able to reproduce radio maps and flux spectra for a large variety of galaxy clusters. In the following we discuss in detail different properties of our results.

5.6.1 Morphology

We found that while keeping all the time windows the same for all the sources in a cluster, we do not observe any change in the overall shape of the radio map. However when measuring surface brightness over time we notice that the surface brightness increases while the sources are active and until they reach an equilibrium state. When the sources are no longer injecting electrons we observe a quick decrease in surface brightness. It is more realistic to consider the case where different time windows are assigned to different sources. In this case we found that the overall shape of the radio map changes when measured at different times. By comparing the results with observations we can understand which sources are active and in which state of the evolution they are in.

We applied this model to a specific cluster, namely the cluster CL1446+26 studied by Govoni et al. (2012) and we found that we were able to reproduce the observed radio emission map and flux with a limited number of sources. In this version of the model we considered sources of a large size, with each one of these sources representing a concentration of galaxies within the cluster. Future improvements of this model will include sources that coincide with each single galaxy in the cluster and possibly with different properties assigned to each one of them.

We also considered increasing the number of sources in a cluster and produced radio maps and flux spectra for some randomly generated clusters with different numbers of sources. We found that with an increase in the number of sources, the radio maps were more extended and had a more regular shape. As a consequence, our model predicts that richer clusters have radio halos with more extended and regular shapes. For this reason we searched for clusters with morphology that is similar to our predicted maps. Presented in figures 5.13 – 5.16 is the comparison between the observed radio halo and the predicted morphologies. We found for example that the clusters A1213 (Giovannini et al., 2009) has morphology that is similar to the predicted morphology in the case of 20 sources. Moreover, clusters A910 (Govoni et al., 2012) has morphology that is similar to the morphology predicted in the case of 50 sources. Furthermore, the clusters A2163 (Feretti et al., 2004) and Coma (Deiss et al., 1997)

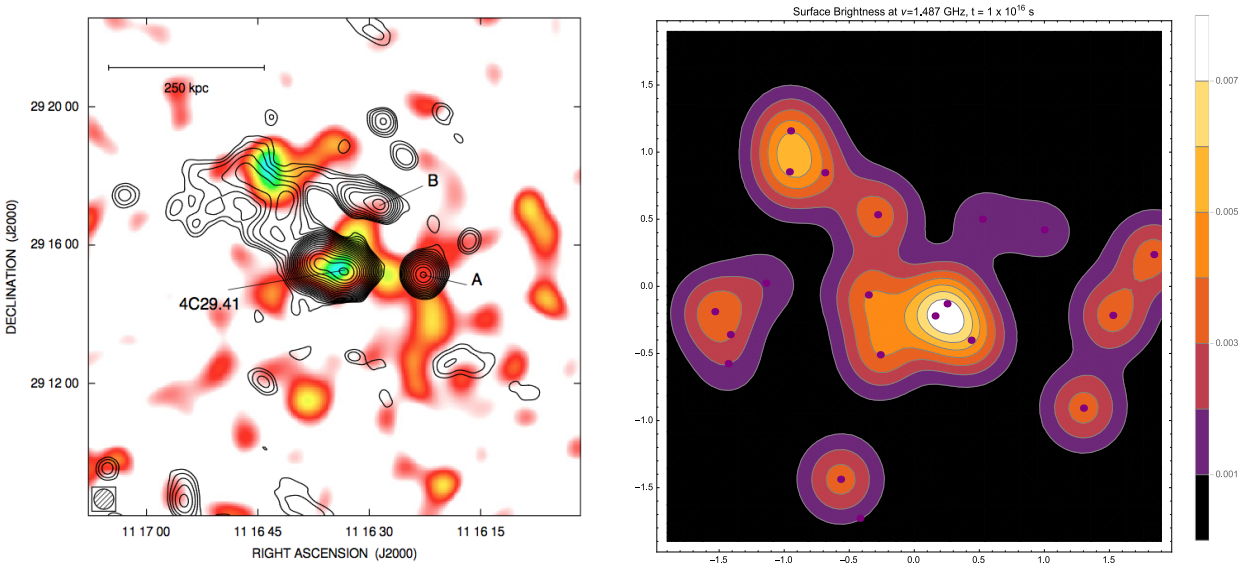

Figure 5.13: Comparison between A1213 Giovannini et al. (2009) and the prediction of the model with 20 sources

have morphologies that are similar to the morphologies predicted in the cases of 80 and 100 sources respectively.

A possible test for this model would be to check if all the observed radio halos can be explained by it. We can do this by searching for clusters where the radio emission is not correlated with the distribution of cluster galaxies. This requires fitting the model to high number of cluster and this work will be carried out in future. However it was recently observed, in cluster A3367, that where the central extended radio emission is missing no radio galaxies were observed in the central region of the cluster (George et al., 2015). This is a point that is in favour of our model.

5.6.2 Spectral Changes

As we saw in section 1.5 some clusters show spectral steepening at high frequencies (see for example Thierbach et al. (2003) for the case of Coma). Our model is able to account for the change in the slope of the flux spectrum as presented in figures 5.8 – 5.11. From these figures we can see that the spectral steepening takes place at $\nu \gtrsim 100$ MHz in this version of the model whereas in galaxy clusters it is usually observed at $2 - 5$ GHz. However, the frequency where the change in slope takes place is dependent on the choices of time windows for the different sources as well as the time of observation as we observed in the case of the evolution of the spectrum of M51 (see Fig. 4.8). In that case the steepening takes place at

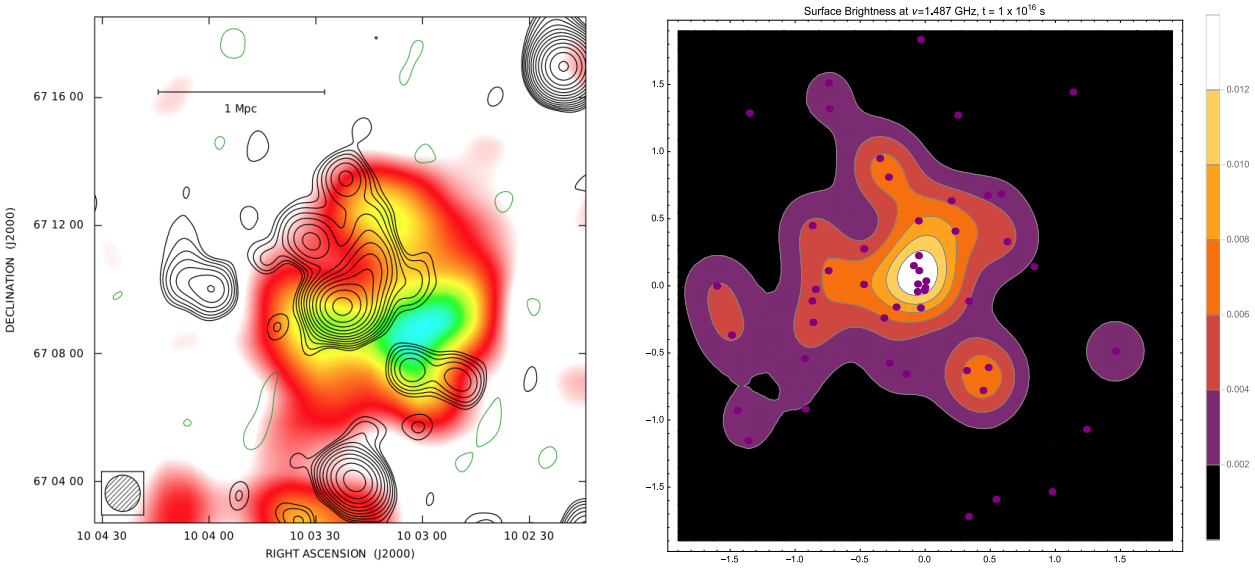

Figure 5.14: Comparison between A910 Govoni et al. (2012) and the prediction of the model with 50 sources

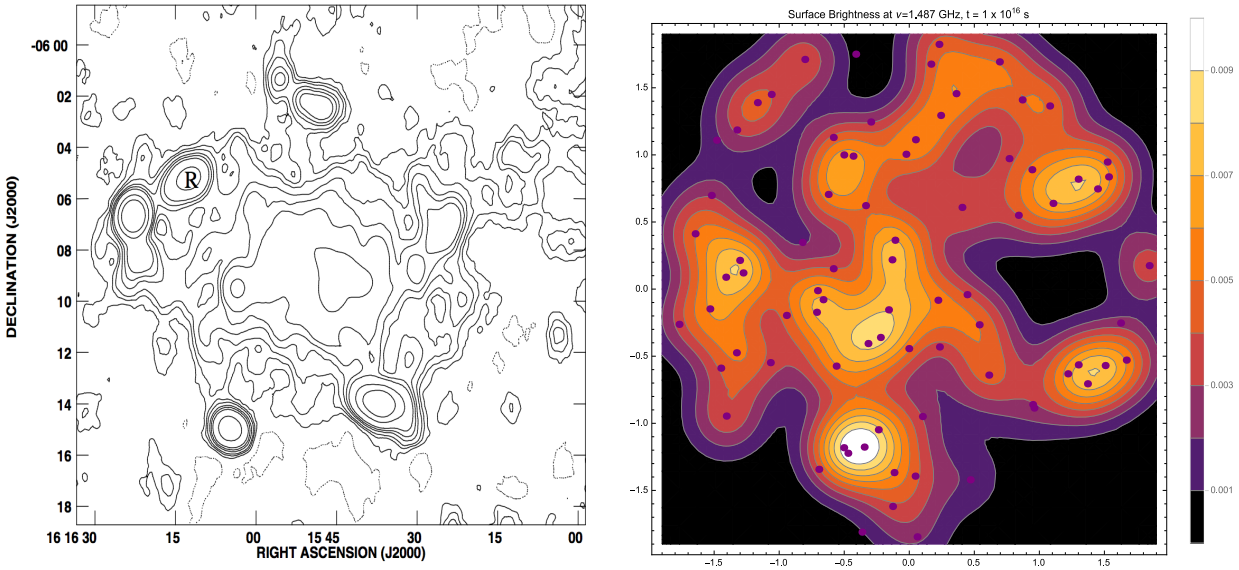

Figure 5.15: Comparison between A2163 (Feretti et al., 2004) and the prediction of the model with 80 sources

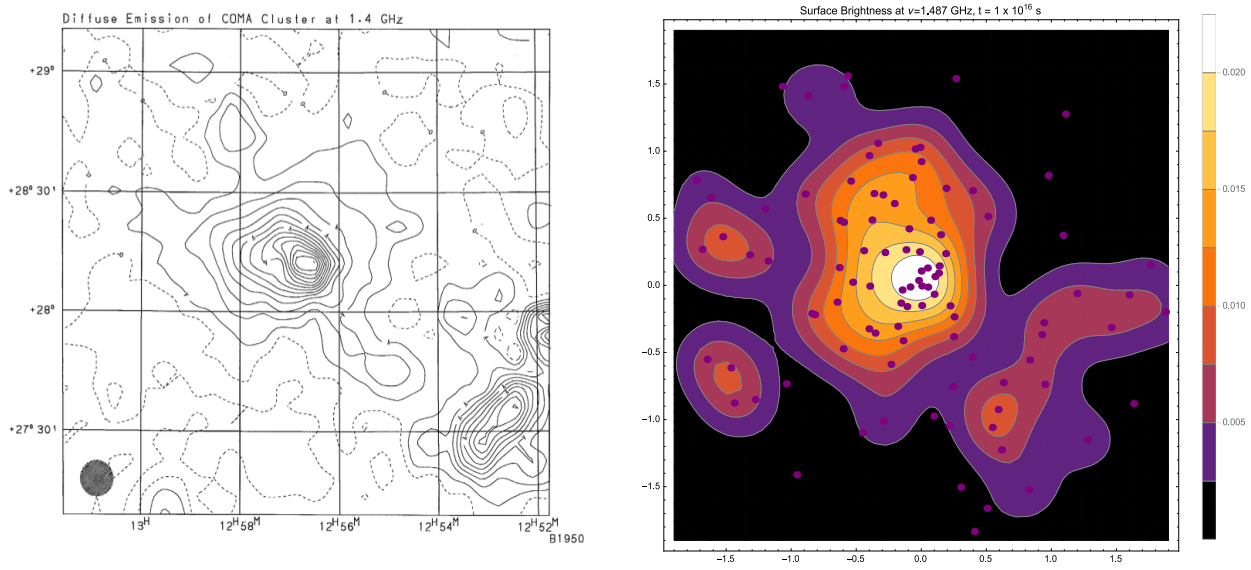

Figure 5.16: Comparison between Coma (Deiss et al., 1997) and the prediction of the model with 100 sources

frequencies between 10 – 20 GHz for a time value of 1×10^{14} s after the injection has ended. We note that this result was calculated for a magnetic field value of 15 μG while for the calculation of a cluster of galaxies we used the value of 1 μG. The timescale for the losses of electrons that are emitting at a frequency ν with magnetic field β_μ according to the relation $\nu \sim 16$ MHz $(E_e/\mathrm{GeV})^2 \beta_\mu$ is given by:

$$t_{loss} = \frac{\gamma}{b(\gamma)} \tag{5.3}$$

with $E_e = \gamma m_e c^2$. Using $\nu = 1.4$ GHz and $\beta_\mu = 1$ we obtain the value of t_{loss} to be 3.6×10^{15} s. In order to obtain steepening at this frequency we considered 12 sources with $t = 1 \times 10^{16}$ s and time windows with $t_1 = 10^{15}$s and four different values of t_2: 6.5×10^{15} s, 7.5×10^{15} s, 8×10^{15} s and 8.5×10^{15} s. These values of t_2 were chosen in order to keep the difference between t and t_2 of the order of the value we obtained for t_{loss}. In this case of 12 sources we assigned the above t_2 values to 2, 3, 5 and 2 sources respectively. In this calculation all the parameters are the same as presented in the Table 5.1 excluding the value of Q_0 which we scale to fit the radio data for Coma. As we can see in the Fig.5.17, the calculated spectrum fits very well to the observed flux spectrum of Coma.

Even though our model is very simple and in its early stages, we are able to reproduce the steepening of the spectrum by tuning the time evolution and time frames of the sources. In improved versions of the model it is possible to consider a larger number of time windows to

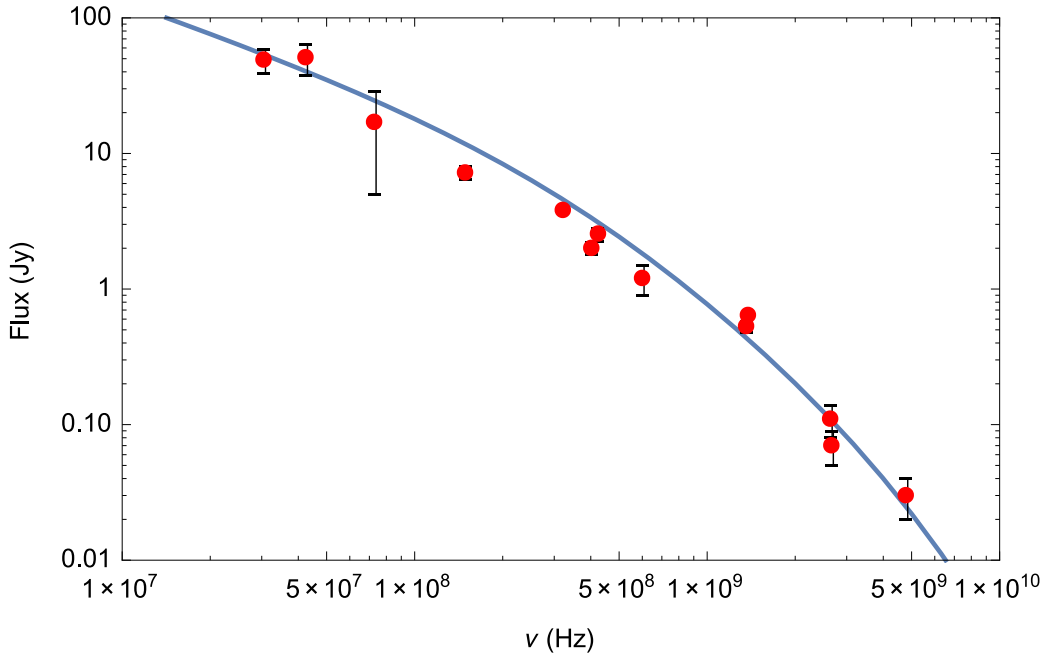

Figure 5.17: The spectrum of a cluster with 12 sources with four different time windows (see text for details) and $Q_0 = 1.0 \times 10^{-24}\mathrm{cm}^{-3}\mathrm{s}^{-1}$ compared with the radio data for Coma from Tierbach et al. (2003).

be assigned to different sources in a cluster in order to obtain more realistic results for both the spectral and spatial properties.

5.6.3 $P_{1.4} - L_x$ Correlation

We found that the change in flux density is almost linear with an increasing number of sources. For this reason this model predicts a strong correlation between the radio luminosity and number of galaxies in clusters. The number of galaxies is mainly correlated with the mass of the cluster and hence we expect the correlation between the radio luminosity and mass of the cluster to be strong as observed in Govoni et al. (2001b).

As we have seen in Fig. 2.10 many clusters exhibit a correlation between the radio and X-ray luminosity with some scatter. However there are some clusters that do not display this correlation very well. In particular, these clusters are over luminous in radio when compared to X-ray. Our model offers a possible explanation of these outliers. We consider the relations $P_{1.4} \propto n_{rel}\ B^{1+\alpha}$, where n_{rel} is the relativistic electron density, B is magnetic field, and α is the spectral index of the radio halo; and $L_x \propto n_e^2\ T^{1/2}$, where n_e is the density and T is the temperature of the thermal gas (Colafrancesco 1999). If the relation $n_{rel} \propto n_e$ holds then

from the above mentioned relations we derive the further relation $P_{1.4} \propto L_x^{1/2}\ T^{-1/4}\ B^{1+\alpha}$. The observed correlation is $P_{1.4} \propto L_x^d$, where $d = 1.78 \pm 0.07$ (Colafrancesco et al. 2014). In our model we have $n_{rel} \propto n_{gal}$ where n_{gal} is number of galaxies. If $n_{gal} \propto n_e$ we are in the previous case. In a general case when $n_{gal} \propto n_e^{\delta}$, accounting for a weaker relation between galaxies and gas distribution, we get that $\tilde{P}_{1.4} \propto L_x^{\delta/2}\ T^{-\delta/4}\ B^{1+\alpha}$. Putting all these relations together we obtain the relation $\tilde{P}_{1.4} \propto L_x^{d\delta}\ B^{(1+\alpha)(1-\delta)}$. When $\delta = 1$, the conditions are in favour of the main correlation where most of the clusters follow the correlation between $P_{1.4}$ and L_x with the slope d. However when $\delta < 1$, we expect a flatter correlation because in this case $d\delta < d$. In Fig. 2.10 we note that the correlation has a constant slope for high values of luminosity but the shape of the correlation may be flatter for clusters with low X-ray luminosity. We can explain this by assuming that the very high luminosity clusters have reached the virial equilibrium state which implies $n_{gal} \propto n_e$. In low luminosity clusters it is possible to have $\delta < 1$ because these clusters may still be undergoing the formation process where they accumulate galaxies but have not reached the complete virial equilibrium state.

5.6.4 $P_{1.4} - P_1/P_0$ Correlation

Some observations show that the radio bi-modality described in previous section is also related to the dynamical state of the hosting cluster (Buote, 2001; Cassano et al., 2010). These studies provided a quantitative comparison between the power of the radio halo and the magnitude of the dipole power ratio (P_1/P_0), connected to the X-Ray morphology, which provides the measure of the degree of asymmetry of clusters that is considered to be connected to the presence of recent merging events. It appears that the clusters with strong radio power have high values of P_1/P_0. However this correlation is not very accurate for small radio powers as there are clusters with very high values of P_1/P_0 but with small values of radio power.

In our model the radio power is expected to be proportional to the number of active radio sources. Apparently there is no direct way to correlate the number of sources with merging events. However studies by Owen et al. (1999) and Miller and Owen (2003) showed that clusters with merging events have higher number of active radio sources produced by starburst and AGNs. These authors considered clusters A2125 and A2255 respectively and suggested the possibility that the merging events are able to trigger star formation and radio emission from galaxies. If this suggestion can be confirmed for many other cluster, it would be in favour of the model presented in this thesis as this would imply that cluster with merging activities will have large number of radio sources and as a consequence our model will predict a larger value of the radio power.

However, the relation between merging events and presence of radio halo in a cluster is not clear, as there are clusters with not clear evidence of strong merging but with a powerful radio halo and there are clusters with strong merging events that don't have radio halos (see Section 2.5). Furthermore, the relation between the relics and merging events was questioned by Vazza and Brüggen (2014). Starting from the absence of gamma rays in clusters, including clusters with powerful halos and relics, these authors found that the efficiency of acceleration of particles produced by merging is not strong enough to account for the formation of radio emission.

We note also that the correlation $P_{1.4} - P_1/P_0$ is only a measure of the degree of asymmetry of X-ray emission in clusters and that it is not necessarily connected to merging events. For example we note that the heating of the gas in a cluster may be due to the particles emitted by galaxies (Colafrancesco and Marchegiani, 2008) and if the galaxies are not distributed uniformly within the cluster it will result in asymmetric distribution of X-ray emission. With this reasoning it is possible to explain the correlation between the power of the radio halo and the magnitude of the dipole power ratio (P_1/P_0) with our model.

5.6.5 Consequences in Other Spectral Bands

To predict the consequences of this model in other spectral bands it is necessary to consider the origin of relativistic electrons. If the electrons are all secondary then strong gamma-ray emission is expected from the same processes that describe the production of the electrons. To consider this case with our model it is necessary to calculate the diffusion of protons then the diffusion of electrons that are produced by proton interactions or dark matter annihilation (see section 2.2). To test the model is possible to compare the predicted emission with the emission observed by instruments like Fermi and the Cherenkov Telescope Array (CTA).

If the electrons are all primary we do not expect a strong emission in gamma-rays because the emission is only produced by Inverse Compton Scattering and non-thermal Bremsstrahlung emissions. Other bands where these emissions can be detected more easily are the hard X-ray and soft gamma-ray bands where future instruments like Astro-H(http://astro-h.isas.jaxa.jp) and AstroGam(http://astrogam.iaps.inaf.it) will be useful.

Chapter 6

Concluding Remarks

"He who loves practice without theory
is like the sailor who boards a ship
without a rudder and compass and
never knows where he may cast."
-Leonardo da Vinci

Overview

The main focus of this thesis is the origin of radio halos in galaxies and clusters of galaxies. We discussed the current problems with existing models that describe the origin of radio halos and found that all of these models present some difficulties either in observation or in theory. Most of these models predict a strong correlation between the X-ray and radio bands in both the observed morphology and luminosity. However, recent studies have found some clusters where this correlation is weak (Govoni et al., 2012). In particular, in some cases the observed morphology of the radio halo is correlated more with the galaxy distribution than with the observed X-ray maps. For this reason we proposed a new model to understand the origin and evolution of radio halos in galaxies and clusters of galaxies. Our hypothesis is that the overall radio halo emission from clusters of galaxies is the superposition of emissions from injected electrons by galaxies that are diffusing in the ICM.

In order to add more substance to this hypothesis we needed to develop a general model that could explain the origin and evolution of relativistic electrons in galaxies. We accomplished this by solving the diffusion equation describing these processes. We obtained a solution of this diffusion equation, which can be used for a very general type of source that varies in its spatial, spectral and temporal properties. The solution therefore is suitable for clusters where different sources with different dynamics are present.

In Chapter 1 we presented descriptions of galaxy clusters and their role in modern cosmology. Discussion on origins of radio halos is presented in Chapter 2. We presented descriptions

of current models and a discussion on observational and theoretical problems related to each of them and described our new proposed idea.

In Chapter 3 we presented the general analytical solution of the diffusion equation and developed a numerical scheme for efficiently solving the integrals in this analytical solution to obtain the spatial, spectral and temporal properties of electron density. Furthermore, in comparing our work to the existing literature we found that published solutions are special cases of our general solution.

To test our model we used it to calculate the synchrotron emission of the galaxy M51 in Chapter 4. Our model was able to reproduce both the spectral and spatial distributions of the radio emission for this galaxy. Furthermore, using our model we were able to predict the evolution of the radio properties for a M51-like galaxy in its rest frame as well as at different cosmological redshifts. This initial application of our model provided quantitative estimates of the values of model parameters that are likely to match the radio properties of a single galaxy. With this insight, we applied this model in Chapter 5 to radio halos in clusters of galaxies describing them as combinations of radio halos from different sources. Initially we calculated the temporal evolution of radio maps by assuming that all the sources in a cluster have the same properties. Later we considered a case in which different time windows were assigned to different sources. With these calculations we were able to predict different shapes of radio maps at different times. We then applied this model to the cluster CL1446+26 as it is one of the clusters where the morphology of the radio emission is not strongly correlated with the X-ray emission. We also considered more general applications of our model by randomly generating more luminous clusters with an increasing number of sources and calculating the spectra and morphologies of the radio halos in these clusters.

We now discuss the main results presented in this thesis and possible future improvements.

Results for a single galaxy

As we have seen in Chapter 4 our model can reproduce the spectral and spatial properties of the galaxy M51 satisfactorily. We found that the use of a single Gaussian could not explain the spatial properties observed at small radii. We therefore considered a double Gaussian source to account for the internal and the extended part of the radio halo. This is in accordance with observations that show the presence of a Seyfert-like nucleus at the centre of M51 and a moderate starburst activity in the more extended part of the galaxy.

Observations of the surface brightness at higher frequency (1.4 GHz) have a different

shape at large radius compared to those at lower frequency (151 MHz). Our model, on the other hand, produces the same shape at both frequencies. We tried varying parameters such as the intensity and the power spectrum of the magnetic field in order to address this problem. However, these changes did not produce satisfactory results. It is possible that the observed shape of the surface brightness can be obtained by allowing the magnetic field to be a function of radius. This would imply that the diffusion coefficient would also be a function of radius. In this case electrons with different energies would diffuse differently and the shape of the surface brightness would vary with frequency. Obtaining these results would require solving the diffusion equation with a radially dependent diffusion coefficient. This is one of the possible improvements to the model which we discuss later.

Instruments like the SKA will be able to observe M51-like galaxies at redshifts 0.2 and more. By observing the spectral deviations in these objects we will be able to derive the times at which the injection of electrons begins and ends. This will enable us to fully parameterise our model from observations.

Results for Clusters of Galaxies

In Chapter 5 we used our model to study radio halos in galaxy clusters. We calculated the superposition of halos produced from the diffusion of electrons from different sources within the cluster. We modelled each source in the cluster with a single gaussian radial distribution because we were only interested in the extended part of the emission. The positions of the sources in the cluster were chosen to match the shape of the radio halo in CL1446+26. The evolution of surface brightness maps were calculated with two different time assumptions. In the first case we assigned the same time window to each source and in the second case different time windows were used. We obtained the surface brightness maps at different times and found that in the first case the morphology of the halo remained the same with change in time whereas in the second case different shapes were obtained at different times.

We initially applied our model to the case of CL1446+26 by finding the positions of the main radio sources in the map and assigning a different time window to each source. In this version of our model we chose a limited number of large sources, which we believe describe concentrations of galaxies in the cluster. With these assumptions we were able to reproduce the morphology of the radio map. We were also able to obtain the observed flux by scaling the normalisation parameter of the source term and found that this value is realistic as it is similar to the value obtained in the case of M51.

We further applied this model to a wide range of randomly generated radio halos in clusters with many sources and obtained their spatial and spectral properties. We found that as the number of sources is increased the morphology of the resulting radio maps becomes more extended and more regular. We compared these maps with the observed maps of some existing clusters and found that there were remarkable similarities between our generated results and observations.

We studied the total spectrum of the radio halo for each of these generated clusters and found that there was some change in the slope of the spectrum. The frequency where the change takes place for a given cluster is dependent on the time windows of the sources in the cluster. By selecting specific time windows for a limited number of sources we were able to obtain a spectrum that accounts for the steepening at high frequencies observed in Coma.

We turned our attention to the observed correlation between the radio and X-ray luminosities of clusters, and in particular to the clusters that do not follow this correlation very well. In our model we expect that the number of relativistic electrons is proportional to the number of galaxies. Assuming the relation between the number of galaxies and the density of the thermal gas to be $n_{gal} \propto n_e^{\delta}$, we obtain the relation $P_{1.4} \propto L_x^{d\delta}$, where d is the exponent that describes this correlation for high luminosity clusters. For most clusters the correlation holds with the value of $\delta = 1$ and for outliers the correlation is flatter and described by $\delta < 1$. In the case $\delta = 1$, the clusters are in complete virial equilibrium and have therefore the number of galaxies and the density of the hot gas has reached linear proportionality. In the case $\delta < 1$ the clusters are still in their formation process and therefore have not reached this virial equilibrium state. This means that the galaxies are still falling towards the centre of the cluster and the density of the thermal gas has not yet increased. Therefore the number of galaxies is not linearly proportional to the density of the thermal gas in this case.

In this thesis we have proposed a new simple model to explain the origin and evolution of radio halos in clusters of galaxies. We have successfully applied the model to a single galaxy (M51) as well as to a cluster of galaxies (CL1446+26). Preliminary results are very promising, and indicate that the model may be useful for studying radio halos in galaxy clusters. This is still an early version of the model, however, and it will need to be tested against more observations and in greater detail before it is fully mature.

Possible Improvements

There are several ways in which the model can still be improved. Some of these are described below:

- In the current model the number of sources is small compared to the usual number of galaxies in a cluster and the size of each source is much larger than the typical size of a galaxy. The sources in this model can be considered to correspond to concentrations of galaxies and not single galaxies. Future versions of the model will incorporate independently derived list of sources, that is individual galaxies with their corresponding positions within the cluster.

- With the exception of time windows, different sources are currently given the same properties in the model. The model can be improved by giving each source different properties, such as spatial and spectral properties as well as the normalisation of the rate of injection.

- Another possible improvement is to consider more realistic source terms where the properties are chosen to take into account the physical origins of the electrons (see section 2.2). It would also be desirable to develop a priori criteria for choosing time windows, perhaps based on the physical injection mechanisms.

- We considered a constant diffusion coefficient in the diffusion equation in order to obtain a simple analytical solution. As discussed above, to match observational data better we may need to consider a radially dependent magnetic field, and therefore a radially dependent diffusion coefficient. In order to implement this change a new solution of the diffusion equation is required. This is quite clear when comparing Eq.(2.1) and Eq.(3.1).

- In this version of the model we have only considered diffusion of relativistic electrons. In order to provide a full description of the properties of galaxy clusters it is also important to consider the diffusion of relativistic protons. This would enable us to model the production of secondary electrons and gamma rays. The analytical solution for the case of diffusing protons is the same as that of electrons but it is necessary to replace the energy loss terms with the appropriate losses for protons (see e.g. Mannheim and Schlickeiser (1994)).

- Our current tests of the model are derived from comparisons of calculated synchrotron emissions with radio observations. Future observations with instruments like MeerKat, ASKAP and SKA will provide detailed information about the morphology and spectrum

of galaxy clusters including low luminosity clusters. These observations will also be able to determine better model parameters such as the time windows of the sources, their radial and spectral distribution as well as the rate of injection.

- The model can be further tested by calculating emission at other spectral bands by different emission processes, for example inverse Compton scattering and non-thermal bremsstrahlung emission. The model can also be used to predict the emission from hadronic interactions and dark matter annihilation. These improvements will allow us to extend the range of spectral bands where this model can predict the spatial and spectral properties of galaxy clusters. These results could be used to test the model by comparing it with the observations of future instruments like Astro-H in X-rays, AstroGam in soft gamma rays and CTA in high energy gamma rays.

Appendix A

Calculation of Synchrotron Emission

The synchrotron emissivity produced by the population of relativistic electrons with a spectrum $f(r,\gamma,t)$ interacting with the magnetic field β in a galaxy is given by

$$j_{syn}(\nu,r) = \int_1^{\gamma_{max}} d\gamma f(r,\gamma,t) P_{syn}(\nu,\gamma,r) \tag{A.1}$$

where ν is the frequency of the photon emitted in the galaxy's reference system [e.g. Schlickeiser et al.(2001)], and

$$\begin{aligned}
P_{syn}(\nu,\gamma,r) &= \int_0^{\pi} d\eta\, p(\eta)\, 2\pi\sqrt{3}\, r_0\, m_e\, c\, \nu_0\, \sin\eta\, F_S(x/\sin\eta) && \text{(A.2)}\\
\nu_0 &= \frac{eB}{2\pi m_e} = 2.8\left(\frac{\beta}{\mu\mathrm{G}}\right)\ \mathrm{Hz} && \text{(A.3)}\\
x &= \frac{2\nu}{3\nu_0\gamma^2}\left[1+\left(\frac{\gamma\nu_p}{\nu}\right)^2\right]^{3/2} && \text{(A.4)}\\
F_S(t) &= t\int_t^{\infty} K_{5/3}(\zeta)d\zeta && \text{(A.5)}\\
p(\eta) &= \frac{1}{2}\sin\eta\ , && \text{(A.6)}
\end{aligned}$$

where $\nu_p = 8980(n_e/1\ \mathrm{cm}^{-3})^{1/2}$ Hz is the plasma frequency, n_e is the electron density of the galaxy plasma, $r_0 = 2.82\times10^{-13}$ cm is the classical radius of the electron, and $K_{5/3}(\zeta)$ is the Bessel modified function of the second kind [see, e.g. Abramowitz and Stegun(1965)]. The approximation of the Eq.(A.5) is given by $F(t) = 1.78\, t^{0.3}\, e^{-t}$.

The flux emitted in the galaxy reference system is given by:

$$F_{syn}(\nu) = \frac{4\pi \int_0^R r^2 j_{syn}(\nu, r) dr}{4\pi D_L^2} \ , \tag{A.7}$$

where D_L is the luminosity distance of the source (galaxy) and R the maximum radius. The surface brightness distribution of the source is given by:

$$S(\nu, r_p) = 2 \int_{r_p}^{R} dr \frac{r}{\sqrt{r^2 - r_p^2}} \, j_{syn}(\nu, r). \tag{A.8}$$

In order to obtain a stable and efficient numerical solution of Eq.(A.7), we needs to transform the integral in Eq.(A.1). The density is a function of r, γ and t in Eq.(A.1). We observed that the density changes rapidly with linearly spaced values of γ, with most of the density at smaller values of γ (See Fig.A.1).

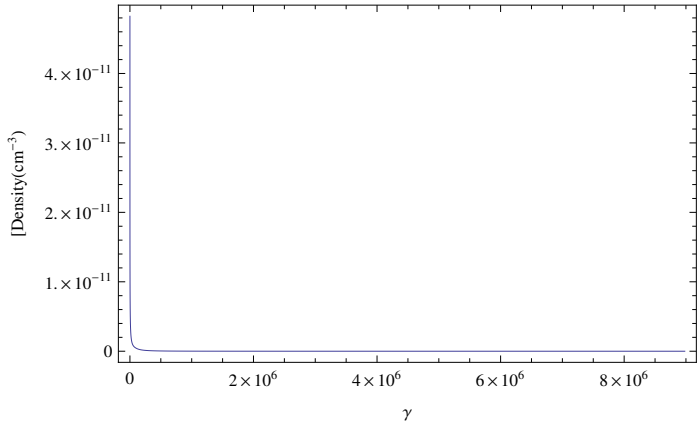

Figure A.1: Density as a function of γ, where γ is spaced linearly.

Since the γ values under consideration span 7 orders of magnitude, it is sensible to consider the logarithm $u = \log \gamma$. The density is well-behaved with respect to u (See Fig.A.2). Thus, integrating over u will be numerically more stable and efficient than integrating over γ. The density tables were generated for values of u linearly spaced from 0 to 7.

When we compute the emissivity we change variables to u:

$$j_{syn}(\nu, r) = \int_1^{\gamma_{max}} d\gamma f(r, \gamma, t) P_{syn}(\nu, \gamma, r) \tag{A.9}$$

$$= \int_0^{\log(\gamma_{max})} du f(r, e^u, t) P_{syn}(\nu, e^u, r) e^u. \tag{A.10}$$

This integral was evaluated numerically using the Trapezoid rule at evenly spaced values

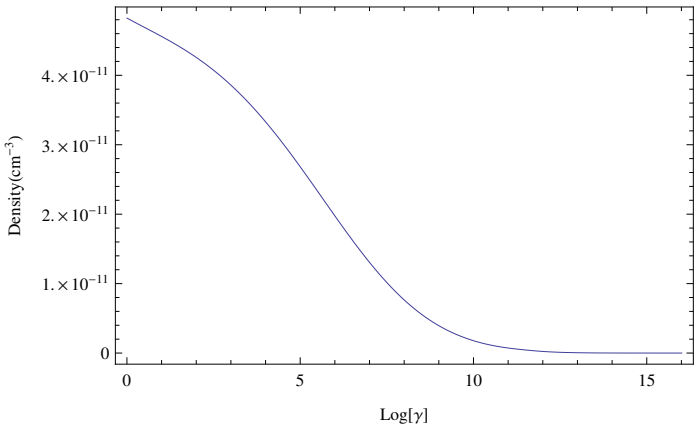

Figure A.2: Density as a function of $u = \log \gamma$. It is clear from the plot that it is easier to integrate over $\log \gamma$ than γ.

of u (precomputed in the density table). Once the emissivity is obtained, the integral over r was computed using the Gauss-Kronrod integrator to calculate flux and surface brightness.

Bibliography

Abazajian, K. N., Markevitch, M., Koushiappas, S. M., and Hickox, R. C.: 2007, *Phys. Rev.,* **75(6)**, 063511

Abell, G. O.: 1958, *ApJS,* **3**, 211

Abell, G. O., Corwin, Jr., H. G., and Olowin, R. P.: 1989, *ApJS,* **70**, 1

Abramowitz, M. and Stegun, I. A.: 1965, *Handbook of Mathematical Functions with Formulas, Graphs and Mathematical Tables*, Dover Book, N.Y

Ackermann, M., Ajello, M., Albert, A., Allafort, A., et al.: 2014, *ApJ,* **787**, 18

Ackermann, M., Ajello, M., Allafort, A., et al.: 2010, *ApJL,* **717**, L71

Ade, P. A. R., Aikin, R. W., Barkats, D., Benton, S. J., et. al, and Bicep2 Collaboration: 2014, *Physical Review Letters,* **112(24)**, 241101

Ajello, M., Rebusco, P., Cappelluti, N., Reimer, O., Böhringer, H., Greiner, J., Gehrels, N., Tueller, J., and Moretti, A.: 2009, *ApJ,* **690**, 367

Allen, S. W., Schmidt, R. W., and Fabian, A. C.: 2001, *MNRAS,* **328**, L37

Arlen, T., Aune, T., Beilicke, M., Benbow, W., et al.: 2012, *ApJ,* **757**, 123

Arnaud, M.: 2005, *CEA/DSM/DAPNIA Service d'Astrophysique L'Orme des Merisiers,* **709**, 91191, Gif sur Yvette Cedex, France, astro-ph/0508159v1

Bacchi, M., Feretti, L., Giovannini, G., and Govoni, F.: 2003, *A&A,* **400**, 465

Baltz, E. A. and Edsjö, J.: 1999, *Phys. Rev. D,* **59**, 023522

Baltz, E. A. and Wai, L.: 2004, *Phys. Rev. D,* **70**, 023512

Bartelmann, M.: 2010, *Classical and Quantum Gravity,* **27(23)**, 233001

Basu, K.: 2012, *MNRAS,* **421**, L112

Battaner, E. and Lesch, H.: 2000, *ArXiv Astrophysics e-prints : astro-ph/0003370*

Battistelli, E. S., De Petris, M., Lamagna, L., Melchiorri, F., Palladino, E., Savini, G., Cooray, A., Melchiorri, A., Rephaeli, Y., and Shimon, M.: 2002, *ApJ,* **580**, L101

Baum, S. A. and O'Dea, C. P.: 1991, *MNRAS,* **250**, 737

Bautz, L. P. and Morgan, W. W.: 1970, *ApJ Lett.,* **162**, L149

Baym, G., Bödeker, D., and McLerran, L.: 1996, *Phys. Rev. D,* **53**, 662

Berezinsky, V. S., Blasi, P., and Ptuskin, V. S.: 1997, *AJ,* **487**, 529

Berghöfer, T. W., Bowyer, S., and Korpela, E.: 2000, *ApJ,* **535**, 615

Berthelsdorf, R. F. and Culhane, J. L.: 1979, *Mon. Not. R. Astron. Soc.,* **187**, 17p

Bertone, G., Hooper, D., and Silk, J.: 2005, *Phys. Rep.,* **405**, 279

BICEP2/Keck, Planck Collaborations, :, Ade, P. A. R., Aghanim, N., Ahmed, Z., Aikin, R. W., Alexander, K. D., Arnaud, M., Aumont, J., et al.: 2015, *ArXiv e-prints:*

1502.00612

Biermann, P. L.: 1950, *Zeit. natueforshung,* **5a**, 65

Biermann, P. L., Enßlin, T. A., Kang, H., Lee, H., and Ryu, D.: 2003, in S. Bowyer and C.-Y. Hwang (eds.), *Matter and Energy in Clusters of Galaxies*, Vol. 301 of *Astronomical Society of the Pacific Conference Series*, p. 293

Birkinshaw, M.: 1999, *PhR,* **310**, 97

Blandford, R. and Eichler, D.: 1987, *Phys. Rep.,* **154**, 1

Blanton, E. L.: 2004, in T. Reiprich, J. Kempner, and N. Soker (eds.), *The Riddle of Cooling Flows in Galaxies and Clusters of galaxies*, p. 181

Blanton, E. L., Sarazin, C. L., and McNamara, B. R.: 2003, *ApJ,* **585**, 227

Blasi, P.: 2000, *ApJ,* **532**, L9

Blasi, P. and Colafrancesco, S.: 1999, *APh,* **12**, 169

Blasi, P. and Colafrancesco, S.: 1999, *Astroparticle Physics,* **12**, 169

Böhringer, H., Matsushita, K., Ikebe, Y., and Churazov, E.: 2002, in S. Borgani, M. Mezzetti, and R. Valdarnini (eds.), *Tracing Cosmic Evolution with Galaxy Clusters*, Vol. 268 of *Astronomical Society of the Pacific Conference Series*, p. 187

Bonafede, A., Feretti, L., Giovannini, G., Govoni, F., Murgia, M., Taylor, G. B., Ebeling, H., Allen, S., Gentile, G., and Pihlström, Y.: 2009, *A&A,* **503**, 707

Bonafede, A., Feretti, L., Murgia, M., Govoni, F., Giovannini, G., Dallacasa, D., Dolag, K., and Taylor, G. B.: 2010, *A&A,* **513**, A30

Bothun, G. (ed.): 1998, *Modern cosmological observations and problems*

Bousso, R.: 2012, *ArXiv e-prints: 1203.0307*

Bowyer, S., Berghöfer, T. W., and Korpela, E. J.: 1999, *ApJ,* **526**, 592

Bowyer, S., Korpela, E. J., Lampton, M., and Jones, T. W.: 2004, *ApJ,* **605**, 168

Bowyer, S., Lieu, R., and Mittaz, J. P.: 1998, in K. Koyama, S. Kitamoto, and M. Itoh (eds.), *The Hot Universe*, Vol. 188 of *IAU Symposium*, p. 185

Bradač, M., Clowe, D., Gonzalez, A. H., Marshall, P., Forman, W., Jones, C., Markevitch, M., Randall, S., Schrabback, T., and Zaritsky, D.: 2006, *ApJ,* **652**, 937

Bradt, H., Mayer, W., Naranan, S., Rappaport, S., and Spuda, G.: 1967, *ApJ,* **161**, L1

Bridle, A. H. and Fomalont, E. B.: 1976, *A&A,* **52**, 107

Briel, U., J, H., Schwarz, R., et al.: 1991, *A&A,* **246**, L10

Briel, U. G., Henry, J. P., and Boehringer, H.: 1992, *A&A,* **259**, L31

Brown, S., Duesterhoeft, J., and Rudnick, L.: 2011, *ApJ,* **727**, L25

Brüggen, M. and Kaiser, C. R.: 2002, *Nature,* **418**, 301

Brunetti, G.: 2003, in S. Bowyer and C.-Y. Hwang (eds.), *Matter and Energy in Clusters of Galaxies*, Vol. 301 of *Astronomical Society of the Pacific Conference Series*, p. 349

Brunetti, G., Blasi, P., Cassano, R., and Gabici, S.: 2004, *MNRAS,* **350**, 1174

Brunetti, G., Blasi, P., Reimer, O., Rudnick, L., Bonafede, A., and Brown, S.: 2012, *MNRAS,* **426**, 956

Brunetti, G., Setti, G., Feretti, L., and Giovannini, G.: 2001, *MNRAS,* **320**, 365

Buote, D. A.: 2001, *ApJ,* **553**, 15

Burles, S. and Tytler, D.: 1998a, *ApJ,* **499**, 699

Burles, S. and Tytler, D.: 1998b, *ApJ,* **507**, 732

Burns, J. O., Roettiger, K., Pinkney, J., Perley, R. A., Owen, F. N., and Voges, W.: 1995, *ApJ,* **446**, 583

Burns, J. O., Sulkanen, M. E., Gisler, G. R., and Perley, R. A.: 1992, *ApJ,* **388**, L49

Byram, E., Chubb, T., and Friedman, H.: 1966, *Science,* **152**, 66

Calzetti, D., Kennicutt, Jr., R. C., Bianchi, L., Thilker, D. A., et al.: 2005, *ApJ,* **633**, 871

Carilli, C. L. and Taylor, G. B.: 2002, *ARA&A,* **40**, 319

Carlstrom, J. E., Joy, M., Grego, L., Holder, G., Holzapfel, W. L., LaRoque, S., Mohr, J. J., and Reese, E. D.: 2001, *ArXiv Astrophysics e-prints: astro-ph/0103480*

Cassano, R. et al.: 2010, *ApJL,* **721**, L82

Cassano, R., Ettori, S., Brunetti, G., Giacintucci, S., Pratt, G. W., Venturi, T., Kale, R., Dolag, K., and Markevitch, M.: 2013, *ApJ,* **777**, 141

Cavaliere, A. and Fusco-Femiano, R.: 1976, *Astron. Astrophys,* **49**, 137

Cavaliere, A., Gursky, H., and Tucker, W. H.: 1971, *Nature,* **231**, 437

Churazov, E., Sunyaev, R., Forman, W., and Böhringer, H.: 2002, *MNRAS,* **332**, 729

Ciardullo, R., Feldmeier, J. J., Jacoby, G. H., de Naray, R. K., Laychak, M. B., and Durrell, P. R.: 2002, *ApJ,* **577**, 31

Clarke, T. E., Kronberg, P. P., and Böhringer, H.: 2001, *ApJ,* **547**, L111

Clowe, D., Bradač, M., Gonzalez, A. H., Markevitch, M., Randall, S. W., Jones, C., and Zaritsky, D.: 2006, *ApJL,* **648**, L109

Colafrancesco, S. and Blasi, P.: 1998, *APh,* **9**, 227

Colafrancesco, S., Dar, A., and De Rújula, A.: 2004, *A&A,* **413**, 441

Colafrancesco, S., Lieu, R., Marchegiani, P., Pato, M., Pieri, L., and Buonanno, R.: 2011a, *A&A,* **527**, A80

Colafrancesco, S. and Marchegiani, P.: 2008, *A&A,* **484**, 51

Colafrancesco, S., Marchegiani, P., and Beck, G.: 2015a, *JCAP,* **2**, 32

Colafrancesco, S., Marchegiani, P., and Buonanno, R.: 2011b, *A&A,* **527**, L1

Colafrancesco, S., Marchegiani, P., and Palladino, E.: 2003, *A&A,* **397**, 27

Colafrancesco, S., Mazzotta, P., Rephaeli, Y., and Vittorio, N.: 1994, *ApJ,* **433**, 454

Colafrancesco, S., Mekuria, R. R., Faltenbacher, A., and Marchegiani, P.: 2015b, *in Prepa-*

ration

Colafrancesco, S. and Mele, B.: 2001, *ApJ,* **562**, 24

Colafrancesco, S., Profumo, S., and Ullio, P.: 2006, *A&A,* **455**, 21

Colafrancesco, S. and Vittorio, N.: 1994, *ApJ,* **422**, 443

Colafrancesco, S., Vittorio, N., and Mazzotta, P.: 1997, in F. R. Bouchet, R. Gispert, B. Guiderdoni, and J. Trân Thanh Vân (eds.), *Microwave Background Anisotropies*, pp 395–400

Colless, M., Dalton, G., Maddox, S., Sutherland, W., Norberg, P., Cole, S., Bland-Hawthorn, J., Bridges, T., Cannon, R., Collins, C., Couch, W., Cross, N., Deeley, K., De Propris, R., Driver, S. P., Efstathiou, G., Ellis, R. S., Frenk, C. S., Glazebrook, K., Jackson, C., Lahav, O., Lewis, I., Lumsden, S., Madgwick, D., Peacock, J. A., Peterson, B. A., Price, I., Seaborne, M., and Taylor, K.: 2001, *MNRAS,* **328**, 1039

Dahlem, M., Lisenfeld, U., and Golla, G.: 1995, *ApJ,* **444**, 119

Dahlem, M., Petr, M. G., Lehnert, M. D., Heckman, T. M., and Ehle, M.: 1997, *A&A,* **320**, 731

Daly, R. A. and Loeb, A.: 1990, *ApJ,* **364**, 451

David, L. P., Nulsen, P. E. J., McNamara, B. R., Forman, W., Jones, C., Ponman, T., Robertson, B., and Wise, M.: 2001, *ApJ,* **557**, 546

de Lapparent, V., Geller, M. J., and Huchra, J. P.: 1986, *ApJL,* **302**, L1

de Lapparent, V., Geller, M. J., and Huchra, J. P.: 1988, *ApJ,* **332**, 44

De Petris, M., D'Alba, L., Lamagna, L., Melchiorri, F., Orlando, A., Palladino, E., Rephaeli, Y., Colafrancesco, S., Kreysa, E., and Signore, M.: 2002, *ApJ,* **574**, L119

Deiss, B. M., Reich, W., Lesch, H., and Wielebinski, R.: 1997, *A&A,* **321**, 55

Dennison, B.: 1980, *ApJ,* **239**, L93

Dewdney, P., Turner, W., Millenaar, R., McCool, R., Lazio, J., and Cornwell, T.: 2012, *SKA baseline design document*, http://www.skatelescope.org/wp-content/uploads/2012/07/SKA-TEL-SKO-DD-001-1˙BaselineDesign1.pdf

Dolag, K., Bartelmann, M., and Lesch, H.: 2002, *A&A,* **387**, 383

Dolag, K. and Schindler, S.: 2000, *A&A,* **364**, 491

Dolag, K., Schindler, S., Govoni, F., and Feretti, L.: 2001, *A&A,* **378**, 777

Dressler, A., Oemler, Jr., A., Couch, W. J., Smail, I., Ellis, R. S., Barger, A., Butcher, H., Poggianti, B. M., and Sharples, R. M.: 1997, *ApJ,* **490**, 577

Drury, L. O.: 1983, *Reports on Progress in Physics,* **46**, 973

Dumas, G., Schinnerer, E., Tabatabaei, F. S., Beck, R., Velusamy, T., and Murphy, E.: 2011, *AJ,* **141**, 41

Eckert, D., Neronov, A., Courvoisier, T. J.-L., and Produit, N.: 2007, *A&A,* **470**, 835

Eckert, D., Produit, N., Paltani, S., Neronov, A., and Courvoisier, T. J.-L.: 2008, *A&A,* **479**, 27

Eilek, J. A. and Owen, F. N.: 2002, *ApJ,* **567**, 202

Einstein, A.: 1936, *Science,* **84**, 506

Eisenstein, D. J., Weinberg, D. H., Agol, E., Aihara, H., Allende Prieto, C., Anderson, S. F., Arns, J. A., Aubourg, É., Bailey, S., Balbinot, E., et al.: 2011, *AJ,* **142**, 72

Elmegreen, D. M. and Elmegreen, B. G.: 1982, *MNRAS,* **201**, 1021

Elmegreen, D. M. and Elmegreen, B. G.: 1987, *ApJ,* **314**, 3

Elmouttie, M., Haynes, R. F., Jones, K. L., Ehle, M., Beck, R., Harnett, J. I., and Wielebinski, R.: 1997, *MNRAS,* **284**, 830

Elvis, M.: 1976, *Mon. Not. R. Astron. Soc.,* **177**, 7p

Enßlin, T., Pfrommer, C., Miniati, F., and Subramanian, K.: 2011, *A&A,* **527**, A99

Enßlin, T. A. and Biermann, P. L.: 1998, *A&A,* **330**, 90

Enßlin, T. A., Biermann, P. L., Kronberg, P. P., and Wu, X.-P.: 1997, *ApJ,* **477**, 560

Enßlin, T. A., Lieu, R., and Biermann, P. L.: 1999, *A&A,* **344**, 409

Fabian, A. C.: 2004, in G. Bertin, D. Farina, and R. Pozzoli (eds.), *Plasmas in the Laboratory and in the Universe: New Insights and New Challenges*, Vol. 703 of *American Institute of Physics Conference Series*, pp 337–344

Fabian, A. C., Sanders, J. S., Taylor, G. B., Allen, S. W., Crawford, C. S., Johnstone, R. M., and Iwasawa, K.: 2006, *MNRAS,* **366**, 417

Feretti, L.: 1999, in H. Boehringer, L. Feretti, and P. Schuecker (eds.), *Diffuse Thermal and Relativistic Plasma in Galaxy Clusters*, p. 3

Feretti, L., Boehringer, H., Giovannini, G., and Neumann, D.: 1997a, *A&A,* **317**, 432

Feretti, L., Dallacasa, D., Giovannini, G., and Tagliani, A.: 1995, *A&A,* **302**, 680

Feretti, L., Dallacasa, D., Govoni, F., Giovannini, G., Taylor, G. B., and Klein, U.: 1999, *A&A,* **344**, 472

Feretti, L., Fusco-Femiano, R., Giovannini, G., and Govoni, F.: 2001, *A&A,* **373**, 106

Feretti, L., Giovannini, G., and Böhringer, H.: 1997b, *New Astr.,* **2**, 501

Feretti, L., Orrù, E., Brunetti, G., Giovannini, G., Kassim, N., and Setti, G.: 2004, *A&A,* **423**, 111

Ferrari, C., Govoni, F., Schindler, S., Bykov, A. M., and Rephaeli, Y.: 2008, *Space Science Reviews,* **134**, 93

Fixsen, D. J., Cheng, E. S., Gales, J. M., Mather, J. C., Shafer, R. A., and Wright, E. L.: 1996, *ApJ,* **473**, 576

Fletcher, A., Beck, R., Shukurov, A., Berkhuijsen, E. M., and Horellou, C.: 2011, *MNRAS,* **412**, 2396

Ford, H. C., Crane, P. C., Jacoby, G. H., Lawrie, D. G., and van der Hulst, J. M.: 1985, *ApJ,* **293**, 132

Forman, W., Jones, C., Cominsky, L., Julien, P., Murray, S., Peters, G., Tananbaum, H., and Giacconi, R.: 1978, *ApJS,* **38**, 357

Fritz, G., Davidsen, A., Meekins, J. F., and H.Friedman: 1971, *ApJ,* **164**, L81

Fujita, Y., Hayashida, K., Nagai, M., Inoue, S., Matsumoto, H., Okabe, N., Reiprich, T. H., Sarazin, C. L., and Takizawa, M.: 2008, *PASJ,* **60**, 1133

Fusco-Femiano, R., Dal Fiume, D., De Grandi, S., Feretti, L., Giovannini, G., Grandi, P., Malizia, A., Matt, G., and Molendi, S.: 2000, *ApJ,* **534**, L7

Fusco-Femiano, R., Dal Fiume, D., Feretti, L., Giovannini, G., Grandi, P., Matt, G., Molendi, S., and Santangelo, A.: 1999, *ApJ,* **513**, L21

Fusco-Femiano, R., dal Fiume, D., Orlandini, M., de Grandi, S., Molendi, S., Feretti, L., Grandi, P., and Giovannini, G.: 2003a, in S. Bowyer and C.-Y. Hwang (eds.), *Matter and Energy in Clusters of Galaxies*, Vol. 301 of *Astronomical Society of the Pacific Conference Series*, p. 109

Fusco-Femiano, R., Orlandini, M., De Grandi, S., Molendi, S., Feretti, L., Giovannini, G., Bacchi, M., and Govoni, F.: 2003b, *A&A,* **398**, 441

Gamow, G.: 1946, *Physical Review,* **70**, 572

Gastaldello, F., Wik, D. R., Molendi, S., Westergaard, N. J., Hornstrup, A., Madejski, G., Ferreira, D. D. M., Boggs, S. E., Christensen, F. E., Craig, W. W., Grefenstette, B. W., Hailey, C. J., Harrison, F. A., Madsen, K. K., Stern, D., and Zhang, W. W.: 2014, *ArXiv e-prints:1411.1573*

George, L. T., Dwarakanath, K. S., Johnston-Hollitt, M., Hurley-Walker, N., Hindson, L., Kapińska, A. D., Tingay, S. J., Bell, M., Callingham, J. R., For, B.-Q., Hancock, P. J., Lenc, E., McKinley, B., Morgan, J., Offringa, A., Procopio, P., Staveley-Smith, L., Wayth, R. B., Wu, C., Zheng, Q., Bernardi, G., Bowman, J. D., Briggs, F., Cappallo, R. J., Corey, B. E., Deshpande, A. A., Emrich, D., Goeke, R., Greenhill, L. J., Hazelton, B. J., Kaplan, D. L., Kasper, J. C., Kratzenberg, E., Lonsdale, C. J., Lynch, M. J., McWhirter, S. R., Mitchell, D. A., Morales, M. F., Morgan, E., Oberoi, D., Ord, S. M., Prabu, T., Rogers, A. E. E., Roshi, A., Udaya Shankar, N., Srivani, K. S., Subrahmanyan, R., Waterson, M., Whitney, R. L. W. A. R., Williams, A., and Williams, C. L.: 2015, *ArXiv e-prints: 1506.00451*

Giacconi, R., Murray, S., Gursky, H., Kellogg, E., Schreier, E., Matilsky, T., Koch, D., and Tananbaum, H.: 1974, *ApJS,* **27**, 37

Giacconi, R., Murray, S., Gursky, H., Kellogg, E., Schreier, E., and Tananbaum, H.: 1972, *ApJ,* **178**, 281

Giacintucci, S., Venturi, T., Brunetti, G., Bardelli, S., Dallacasa, D., Ettori, S., Finoguenov, A., Rao, A. P., and Zucca, E.: 2005, *A&A,* **440**, 867

Gioia, I. M. and Gregorini, L.: 1980, *A&AS,* **41**, 329

Giovannini, G., Bonafede, A., Feretti, L., Govoni, F., Murgia, M., Ferrari, F., and Monti, G.: 2009, *A&A,* **507**, 1257

Giovannini, G. and Feretti, L.: 2000, *New Astr.,* **5**, 335

Giovannini, G. and Feretti, L.: 2002, in L. Feretti, I. M. Gioia, and G. Giovannini (eds.), *Merging Processes in Galaxy Clusters*, Vol. 272 of *Astrophysics and Space Science Library*, pp 197–227

Giovannini, G., Feretti, L., Girardi, M., Govoni, F., Murgia, M., Vacca, V., and Bagchi, J.: 2011, *A&A,* **530**, L5

Giovannini, G., Feretti, L., Venturi, T., Kim, K.-T., and Kronberg, P. P.: 1993, *ApJ,* **406**, 399

Giovannini, G., Tordi, M., and Feretti, L.: 1999, *New Astr.,* **4**, 141

Govoni, F., Enßlin, T. A., Feretti, L., and Giovannini, G.: 2001a, *A&A,* **369**, 441

Govoni, F. and Feretti, L.: 2004, *International Journal of Modern Physics D* **13**, 1549

Govoni, F., Ferrari, C., Ferretti, L., Vacca, V., Murgia, M., Giovannini, G., Perley, R., and Benoist, C.: 2012, *A&J,* **545**, A74

Govoni, F., Murgia, M., Feretti, L., Giovannini, G., Dolag, K., and Taylor, G. B.: 2006, *A&A,* **460**, 425

Govoni, F., Taylor, G. B., Dallacasa, D., Feretti, L., and Giovannini, G.: 2001b, *A&A,* **379**, 807

Gruber, D. and Rephaeli, Y.: 2002, *ApJ,* **565**, 877

Gursky, H., Kellogg, E., Leong, C., Tananbaum, H., and Giacconi, R.: 1971a, *ApJ,* **165**, L43

Gursky, H., Kellogg, E., Murray, S., Leong, C., Tananbaum, H., and Giacconi, R.: 1971b, *ApJ,* **165**, L81

Gursky, H., Solinger, A., Kellogg, E., Murray, S., Tananbaum, H., Giacconi, R., and Cavaliere, A.: 1972, *ApJL,* **173**, L99

Guth, A. H.: 1981, *Phy. Rev. D* **23**, 347

Hales, S. E. G., Baldwin, J. E., and Warner, P. J.: 1988, *MNRAS,* **234**, 919

Harris, D. E. and Grindlay, J. E.: 1979, *MNRAS,* **188**, 25

Harrison, E. R.: 1970, *MNRAS,* **147**, 279

Heesen, V., Beck, R., Krause, M., and Dettmar, R.-J.: 2009, *A&A,* **494**, 563

Hinshaw, G., Larson, D., Komatsu, E., Spergel, D. N., Bennett, C. L., Dunkley, J., Nolta, M. R., Halpern, M., Hill, R. S., Odegard, N., Page, L., Smith, K. M., Weiland, J. L., Gold, B., Jarosik, N., Kogut, A., Limon, M., Meyer, S. S., Tucker, G. S., Wollack, E., and

Wright, E. L.: 2013, *ApJS,* **208**, 19

Holzapfel, W. L., Ade, P. A. R., Church, S. E., Mauskopf, P. D., Rephaeli, Y., Wilbanks, T. M., and Lange, A. E.: 1997, *ApJ,* **481**, 35

Israel, F. P. and Mahoney, M. J.: 1990, *ApJ,* **352**, 30

Jaffe, W. J.: 1977, *ApJ,* **212**, 1

Jones, C. and Forman, B.: 1992, *in NATO ASI Vol,* **366**, p. 49

Jones, C. and Forman, W.: 1984, *Astrophys. J.,* **276**, 38

Kaastra, J. S., Lieu, R., Mittaz, J. P. D., Bleeker, J. A. M., Mewe, R., Colafrancesco, S., and Lockman, F. J.: 1999, *ApJ,* **519**, L119

Kaastra, J. S., Tamura, T., Peterson, J. R., et al.: 2004, *A&A,* **413**, 415

Kaiser, C. R. and Binney, J.: 2003, *MNRAS,* **338**, 837

Kassim, N. E., Clarke, T. E., Enßlin, T. A., Cohen, A. S., and Neumann, D. M.: 2001, *ApJ,* **559**, 785

Kellogg, E. M., Gursky, H., Leong, C., Schreier, E., Tananbaum, H., and Giacconi, R.: 1971, *ApJL,* **165**, L49

Kellogg, E. M., Murray, S., Giacconi, R., Tananbaum, H., and Gursky, H.: 1973, *ApJL,* **185**, L13

Kim, K.-T., Kronberg, P. P., Dewdney, P. E., and Landecker, T. L.: 1990, *ApJ,* **355**, 29

King, I. R.: 1962, *Astron. J.,* **67**, 471

Klein, U. and Emerson, D. T.: 1981, *A&A,* **94**, 29

Klein, U., Wielebinski, R., and Beck, R.: 1984, *A&A,* **135**, 213

Kolb, E. W. and Turner, M. S.: 1990, *The Early Universe*, Addison-Wesley, Redwood City

Kronberg, P. P.: 1996, *SSRv,* **75**, 387

Large, M. I., Mathewson, D. S., and Haslam, C. G. T.: 1959, *Nature,* **183**, 1663

Lesch, H. and Birk, G. T.: 1998, *Physics of Plasmas,* **5**, 2773

Lewis, A. D., Stocke, J. T., and Buote, D. A.: 2002, *ApJL,* **573**, L13

Liang, H., Hunstead, R. W., Birkinshaw, M., and Andreani, P.: 2000, *ApJ,* **544**, 686

Liddle, A. R.: 1997, in *From Quantum Fluctuations to Cosmological Structures*, Vol. 126 of *Astronomical Society of the Pacific Conference Series*, p. 31

Lieu, R., Mittaz, J. P. D., Bowyer, S., Breen, J. O., Lockman, F. J., Murphy, E. M., and Hwang, C.-Y.: 1996a, *Science,* **274**, 1335

Lieu, R., Mittaz, J. P. D., Bowyer, S., Lockman, F. J., Hwang, C.-Y., and Schmitt, J. H. M. M.: 1996b, *ApJ,* **458**, L5

Longair, M. S.: 1994, *High energy astrophysics.*, Cambridge: Cambridge University Press

Mannheim, K. and Schlickeiser, R.: 1994, *A&A,* **286**, 983

Marchegiani, P., Perola, G. C., and Colafrancesco, S.: 2007, *A&A,* **465**, 41

Markevitch, M.: 2005, *ArXive:astro-ph/0511345,*

Markevitch, M., Gonzales, A. H., David, L., et al.: 2002, *ApJ,* **567**, L27

Markevitch, M., Ponman, T., Nulsen, P. E. J., et al.: 2000, *ApJ,* **541**, 542

Markevitch, M., Sarazin, C., and Vikhlinin, A.: 1999, *ApJ,* **521**, 526

Mather, J. C., Cheng, E. S., Eplee, Jr., R. E., Isaacman, R. B., Meyer, S. S., Shafer, R. A., Weiss, R., Wright, E. L., Bennett, C. L., Boggess, N. W., Dwek, E., Gulkis, S., Hauser, M. G., Janssen, M., Kelsall, T., Lubin, P. M., Moseley, Jr., S. H., Murdock, T. L., Silverberg, R. F., Smoot, G. F., and Wilkinson, D. T.: 1990, *ApJL,* **354**, L37

Mathewson, D. S., van der Kruit, P. C., and Brouw, W. N.: 1972, *A&A,* **17**, 468

Meekins, J. F., Gilbert, F., Chubb, T. A., Friedman, H., and Henry, R. C.: 1971, *Nature,* **231**, 107

Miller, N. A. and Owen, F. N.: 2003, *AJ,* **125**, 2427

Miniati, F., Jones, T. W., Kang, H., and Ryu, D.: 2001a, *ApJ,* **562**, 233

Miniati, F., Ryu, D., Kang, H., and Jones, T. W.: 2001b, *ApJ,* **559**, 59

Mitchell, R. and Culhane, J. L.: 1977, *Mon. Not. R. Astron. Soc.,* **178**, 75p

Mitchell, R., Culhane, J. L., Davison, P. J., and Ives, J. C.: 1976, *Mon. Not. R. Astron. Soc.,* **175**, 29p

Mittaz, J. P. D., Lieu, R., and Lockman, F. J.: 1998, *ApJ,* **498**, L17

Moskalenko, I. V. and Strong, A. W.: 1998, *ApJ,* **493**, 694

Mroczkowski, T., Dicker, S., Sayers, J., Reese, E. D., Mason, B., Czakon, N., Romero, C., Young, A., Devlin, M., Golwala, S., Korngut, P., Sarazin, C., Bock, J., Koch, P. M., Lin, K.-Y., Molnar, S. M., Pierpaoli, E., Umetsu, K., and Zemcov, M.: 2012, *ApJ,* **761**, 47

Mulcahy, D. D., Horneffer, A., Beck, R., Heald, G., Fletcher, A., Scaife, A., Adebahr, B., Anderson, J. M., Bonafede, A., Brüggen, M., Brunetti, G., Chyży, K. T., Conway, J., Dettmar, R. J., Enßlin, T., Haverkom, M., Horellou, C., Iacobelli, M., Israel, F. P., Junklewitz, H., Jurusik, W., Köhler, J., Kuniyoshi, M., Orrú, E., Paladino, R., Pizzo, R., Reich, W., and Röttgering, H. J. A.: 2014, *A&A,* **568**, A74

Murgia, M., Eckert, D., Govoni, F., Ferrari, C., Pandey-Pommier, M., Nevalainen, J., and Paltani, S.: 2010, *A&A,* **514**, A76

Murgia, M., Govoni, F., Feretti, L., Giovannini, G., Dallacasa, D., Fanti, R., Taylor, G. B., and Dolag, K.: 2004, *A&A,* **424**, 429

Mushotzky, R. F., Serlemitsos, P. J., Smith, B. W., Boldt, E. A., and Hol, S. S.: 1978, *AJ,* **225**, 21

Mushotzky, R. F. and Smith, B. W.: 1980, *Highlights of Astronomy,* **5**, 735

Ogrean, G. A. and Brüggen, M.: 2013, *MNRAS,* **433**, 1701

Ogrean, G. A., Brüggen, M., van Weeren, R. J., Burgmeier, A., and Simionescu, A.: 2014,

MNRAS, **443**, 2463

Ogrean, G. A., Brüggen, M., van Weeren, R. J., Röttgering, H., Croston, J. H., and Hoeft, M.: 2013, *MNRAS,* **433**, 812

Owen, F., Morrison, G., and Voges, W.: 1999, *Diffuse Thermal and Relativistic Plasma in Galaxy Clusters*

Owen, F. N., Eilek, J. A., and Kassim, N. E.: 2000, *ApJ,* **543**, 611

Owen, F. N., Ledlow, M. J., Keel, W. C., and Morrison, G. E.: 1999, *AJ,* **118**, 633

Padmanabhan, T.: 1995, *Structure formation in the universe*, Cambridge U Press

Pandey-Pommier, M., Richard, J., Combes, F., Dwarakanath, K. S., Guiderdoni, B., Ferrari, C., Sirothia, S., and Narasimha, D.: 2013, *A&A,* **557**, A117

Peebles, P. J. and Ratra, B.: 2003, *Reviews of Modern Physics,* **75**, 559

Peebles, P. J. E.: 1980, *The large-scale structure of the universe*, Princeton University Press, Princeton, N.J.

Peebles, P. J. E.: 1993, *Principle of Physical Cosmology*, Princeton University Press

Penzias, A. A. and Wilson, R. W.: 1965, *AJ,* **142**, 419

Pérez-Torres, M. A., Zandanel, F., Guerrero, M. A., Pal, S., Profumo, S., Prada, F., and Panessa, F.: 2009, *MNRAS,* **396**, 2237

Perley, R. A. and Taylor, G. B.: 1991, *AJ,* **101**, 1623

Perola, G. C. and Reinhardt, M.: 1972, *A&A,* **17**, 432

Peterson, J. R., Kahn, S. M., Paerels, F. B. S., Kaastra, J. S., Tamura, T., Bleeker, J. A. M., Ferrigno, C., and Jernigan, J. G.: 2003, *ApJ,* **590**, 207

Petrosian, V.: 2001, *ApJ,* **557**, 560

Pfrommer, C. and Enßlin, T. A.: 2004, *A&A,* **413**, 17

Pinzke, A. and Pfrommer, C.: 2010, *MNRAS,* **409**, 449

Planck Collaboration, Ade, P. A. R., Aghanim, N., Arnaud, M., Arroja, F., Ashdown, M., Aumont, J., Baccigalupi, C., Ballardini, M., Banday, A. J., et al.: 2015a, *ArXiv e-prints : 1502.02114*

Planck Collaboration, Ade, P. A. R., Aghanim, N., Arnaud, M., Ashdown, M., Aumont, J., Baccigalupi, C., Banday, A. J., Barreiro, R. B., Barrena, R., et al.: 2015b, *ArXiv e-prints,1502.01598,*

Planck Collaboration, Ade, P. A. R., Aghanim, N., Arnaud, M., Ashdown, M., Aumont, J., Baccigalupi, C., Banday, A. J., Barreiro, R. B., Bartlett, J. G., et al.: 2015c, *ArXiv e-prints: 1502.01589*

Press, W. H. and Schechter, P.: 1974, *ApJ,* **187**, 425

Quashnock, J. M., Loeb, A., and Spergel, D. N.: 1989, *ApJ,* **344**, L49

Rave, G., Kushnir, D., and Waxman, E.: 2013, *ArXiv e-prints - 1304.4234*

Rees, M. J.: 1989, in L. V. Keldysh and V. I. Fainberg (eds.), *Problems in Theoretical Physics and Astrophysics*, pp 415–421

Rees, M. J. and Setti, G.: 1968, *Nature,* **219**, 127

Reid, A. D., Hunstead, R. W., Lemonon, L., and Pierre, M. M.: 1999, *MNRAS,* **302**, 571

Rephaeli, Y.: 1979, *ApJ,* **227**, 364

Rephaeli, Y., Gruber, D., and Blanco, P.: 1999, *ApJ,* **511**, L21

Reynolds, C. S., McKernan, B., Fabian, A. C., Stone, J. M., and Vernaleo, J. C.: 2005, *MNRAS,* **357**, 242

Roettiger, K., Stone, J. M., and Burns, J. O.: 1999, *ApJ,* **518**, 594

Roettiger, K., Stone, J. M., and Mushotzky, R. F.: 1998, *ApJ,* **493**, 62

Rood, H. J. and Sastry, G. N.: 1971, *Publ. Astron. Soc. Poc.,* **83**, 313

Rossetti, M. and Molendi, S.: 2004, *A&A,* **414**, L41

Rothenflug, R. and M.Arnaud: 1985, *A&A,* **144**, 431

Rots, A. H., Bosma, A., van der Hulst, J. M., Athanassoula, E., and Crane, P. C.: 1990, *AJ,* **100**, 387

Rottgering, H., Snellen, I., Miley, G., de Jong, J. P., Hanisch, R. J., and Perley, R.: 1994, *ApJ,* **436**, 654

Rottgering, H. J. A., Wieringa, M. H., Hunstead, R. W., and Ekers, R. D.: 1997, *MNRAS,* **290**, 577

Russell, H. R., van Weeren, R. J., Edge, A. C., McNamara, B. R., Sanders, J. S., Fabian, A. C., Baum, S. A., Canning, R. E. A., Donahue, M., and O'Dea, C. P.: 2011, *MNRAS,* **417**, L1

Ruszkowski, M. and Begelman, M. C.: 2002, *ApJ,* **581**, 223

Ruszkowski, M., Brüggen, M., and Begelman, M. C.: 2004, *ApJ,* **611**, 158

Ryu, D., Kang, H., Hallman, E., and Jones, T. W.: 2003, *ApJ,* **593**, 599

S. Zimmer for the Fermi-LAT Collaboration: 2015, *ArXiv e-prints: 1502.02653*

Sarazin, C. L.: 1988, *X-ray emission from clusters of galaxies*, Cambridge Astrophysics Series, Cambridge: Cambridge University Press

Sarazin, C. L.: 1999, *ApJ,* **520**, 529

Sarazin, C. L. and Kempner, J. C.: 2000, *ApJ,* **533**, 73

Sarazin, C. L. and Lieu, R.: 1998, *ApJ,* **494**, L177

Sarkar, S.: 1996, *Reports on Progress in Physics,* **59**, 1493

Schlickeiser, R.: 2001, *Cosmic Ray Astrophysics,*, Springer-Verlag, Berlin

Segalovitz, A.: 1977, *A&A,* **54**, 703

Serlemitsos, P. J., Smith, B. W., Boldt, E. A., Holt, S. S., and Swank, J. H.: 1977, *Astrophys. J. Lett.,* **211**, L63

Shimwell, T. W., Brown, S., Feain, I. J., Feretti, L., Gaensler, B. M., and Lage, C.: 2014, *MNRAS,* **440**, 2901

Shimwell, T. W., Markevitch, M., Brown, S., Feretti, L., Gaensler, B. M., Johnston-Hollitt, M., Lage, C., and Srinivasan, R.: 2015, *ArXiv e-prints: 1502.01064*, Provided by the SAO/NASA Astrophysics Data System

Skivie, P.: 2009, *ArXiv e-prints: 0909.0949*

Springel, V., White, S. D. M., Jenkins, A., Frenk, C. S., Yoshida, N., Gao, L., Navarro, J., Thacker, R., Croton, D., Helly, J., Peacock, J. A., Cole, S., Thomas, P., Couchman, H., Evrard, A., Colberg, J., and Pearce, F.: 2005, *Nature,* **435**, 629

Steinhardt, P. and Turok, N.: 2006, *Science,* **312**, 1180

Syrovat-skii, S.: 1959, *SvA,* **3**, 22

Tamura, T., Kaastra, J. S., Peterson, J. R., Paerels, F. B. S., Mittaz, J. P. D., Trudolyubov, S. P., Stewart, G., Fabian, A. C., Mushotzky, R. F., Lumb, D. H., and Ikebe, Y.: 2001, *A&A,* **365**, L87

Taylor, G. B., Fabian, A. C., and Allen, S. W.: 2002, *MNRAS,* **334**, 769

Taylor, G. B., Fabian, A. C., Gentile, G., Allen, S. W., Crawford, C., and Sanders, J. S.: 2007, *MNRAS,* **382**, 67

Taylor, G. B., Govoni, F., Allen, S. W., and Fabian, A. C.: 2001, *MNRAS,* **326**, 2

Taylor, G. B. and Perley, R. A.: 1993, *ApJ,* **416**, 554

Thierbach, M., Klein, U., and Wielebinski, R.: 2003, *A&A,* **397**, 53

Thornley, M. D., Braine, J., and Gardan, E.: 2006, *ApJ,* **651**, L101

Timokhin, A. N., Aharonian, F. A., and Neronov, A. Y.: 2004, *A&A,* **417**, 391

Tribble, P. C.: 1993, *MNRAS,* **263**, 31

Trimble, V.: 1987, *ARA&A,* **25**, 425

Turner, M. S. and Tyson, J. A.: 1999, *Reviews of Modern Physics Supplement,* **71**, 145

Turner, M. S. and Widrow, L. M.: 1988, *Phys. Rev. D,* **37**, 2743

Valinia, A., Henriksen, M. J., Loewenstein, M., Roettiger, K., Mushotzky, R. F., and Madejski, G.: 1999, *ApJ,* **515**, 42

van Weeren, R. J., Röttgering, H. J. A., Brüggen, M., and Cohen, A.: 2009, *A&A,* **505**, 991

Vazza, F. and Brüggen, M.: 2014, *MNRAS,* **437**, 2291

Vazza, F., Gheller, C., and Brüggen, M.: 2014, *MNRAS,* **439**, 2662

Venturi, T., Bardelli, S., Dallacasa, D., Brunetti, G., Giacintucci, S., Hunstead, R. W., and Morganti, R.: 2003, *A&A,* **402**, 913

Vernaleo, J. C. and Reynolds, C. S.: 2006, *ApJ,* **645**, 83

Vikhlinin, A., Markevitch, M., and Murray, S.: 2001, *ApJ,* **549**, L47

Viner, M. R. and Erickson, W. C.: 1975, *AJ,* **80**, 931

Voit, G. M. and Donahue, M.: 2005, *ApJ,* **634**, 955

Völk, H. J., Aharonian, F. A., and Breitschwerdt, D.: 1996, *SSRv,* **75**, 279

Völk, H. J. and Atoyan, A. M.: 2000, *ApJ,* **541**, 88

Vorontsov-Velyaminov, B. A.: 1959, *Atlas and catalog of interacting galaxies. 1959, Sternberg Institute, Moscow State University.*

Waldram, E. M., Yates, J. A., Riley, J. M., and Warner, P. J.: 1996, *MNRAS,* **282**, 779

Watanabe, M., Yamashita, K., Furuzawa, A., Kunieda, H., and Tawara, Y.: 2001, *PASJ,* **53**, 605

Weinberg, S.: 1972, *Gravitation and Cosmology: Principals and Applications of the General Theory of Relativity*, Wiley, New York

Wilson, M.: 1970, *MNRAS,* **151**, 1

Wolfe, B. and Melia, F.: 2006, *ApJ,* **638**, 125

Wu, X. P., Xue, Y. J., and Fang, L. Z.: 1999, *ApJ* **524**, 22

Zeldovich, Y. B. and Sunyaev, R. A.: 1969, *Ap&SS,* **4**, 301

Zemcov, M., Rex, M., Rawle, T. D., Bock, J. J., et al.: 2010, *A&A,* **518**, L16

Zwicky, F.: 1933, *Helvetica Physica Acta,* **6**, 110

Zwicky, F., Herzog, E., Wild, P., Karpowicz, M., and Kowal, C. T.: 1961, *Catalogue of galaxies and of clusters of galaxies, Vol. I*, Pasadena: California Institute of Technology (CIT)